EFFECTS OF TUMOR MICROENVIRONMENTAL CUES ON ENDOTHELIAL CELL BEHAVIOR AND CHEMOTHERAPEUTIC EFFICIENCY

A Dissertation

Presented to the Faculty of the Graduate School

of Cornell University

In Partial Fulfillment of the Requirements for the Degree of

Doctor of Philosophy

by

Danielle Judith LaValley

December 2018

EFFECTS OF TUMOR MICROENVIRONMENTAL CUES ON ENDOTHELIAL CELL BEHAVIOR AND CHEMOTHERAPEUTIC EFFICENCY

Danielle Judith LaValley, Ph. D.

Cornell University 2018

Cancer is a leading cause of death worldwide and within the US. While cancer initially arises from genetic mutations that transform otherwise healthy cells into cancerous cells, the growth, expansion, and metastasis of malignant tumors is dictated by local mechanical and biological cues, collectively known as the tumor microenvironment. Accordingly, to successfully treat cancer, one must target microenvironmental cues that emerge from tumor-associated stromal cells and extracellular matrix, in addition to the cancer cells. However, most cancer therapeutics do not effectively eradicate the disease, highlighting the need to improve our knowledge of cancer biology and develop novel treatments to target cancerous phenotypes with minimal side effects. Thus, the objectives of this dissertation are two-fold: to expand our current understanding of molecular mechanisms involved in tumor angiogenesis that contribute to cancer progression, and to create a human-based platform to screen anti-cancer therapeutics.

During tumor progression, the cancer microenvironment evolves both chemically and mechanically. In line with the first goal above, endothelial cell behavior was investigated as a function of increased extracellular matrix stiffness and elevated

vascular endothelial growth factor (VEGF) production, two known characteristics of the tumor microenvironment. My data indicate additive effects from both stimuli on VEGF receptor internalization, endothelial signaling, and proliferation, emphasizing the need to design cancer therapeutics to target multiple signaling pathways. While basic research such as that from goal number one can shed light on therapeutic targets, this basic science must subsequently be utilized in translational studies. Therefore, in line with the second goal, I designed a body-on-a-chip microfluidic device to investigate tumor-specific factors in cancer drug development. Such systems are critical in translating cancer biology research within drug screening models. My design creates a physiologically-relevant model to test both efficacy and toxicity of anti-cancer drugs, promoting unidirectional flow on a pumpless platform and using multicellular tumor spheroids as realistic tumor models. My data reveal both chemotherapeutic-induced cytotoxicity to the intended cancer cells and undesired toxic side effects in distant organs. Collectively, the data in this dissertation present a multifaceted approach to improve cancer treatment where basic science advances are translated to human-based drug screening systems.

BIOGRAPHICAL SKETCH

Danielle Judith LaValley was born in Ware, MA on May 7, 1991 to Darrell and Judy LaValley and grew up with her two siblings, Lisa and Drew. She graduated as Valedictorian of Ware High School in 2009. Danielle attended the University of Massachusetts Amherst to pursue a degree in chemical engineering with a concentration in biochemical engineering. While at UMass, Danielle began her first of many cancer-related research projects in the laboratory of Professor Shelly Peyton. In the summer of 2011, she participated in the Bioengineered Interfaces and Devices REU Program at the University of Kentucky. She graduated magna cum laude from UMass in May 2013. Later that year, Danielle entered the biomedical engineering Ph.D. program at Cornell University and was awarded a Douglas Fellowship. She joined the lab of Professor Cynthia Reinhart-King and began research on the influence of cancer-related extracellular cues on endothelial cell behavior. Danielle was awarded a National Science Foundation Graduate Research Fellowship in 2015. In 2016, she began working within the lab of Professor Michael Shuler designing a body-on-a-chip microfluidic device to aid in the development of cancer therapeutics. Danielle completed her Ph.D. in December 2018. In addition to spending time in lab, she enjoys visiting with family and friends, playing sports, and spending time outdoors.

To my family and friends.

ACKNOWLEDGMENTS

I would like to sincerely thank both of my research advisors, Drs. Cynthia Reinhart-King and Michael Shuler. My experiences with both of you have helped me grow as a researcher and as a person in general.

Cindy, I am extremely thankful for my time in your lab. From the very beginning you welcomed me in graciously and served as a friend and mentor to me every day thereafter. Your endless guidance and encouragement always kept me going. Thank you for always supporting every decision I made.

Mike, I cannot express how grateful I am to you for allowing me to continue my Ph.D. work in your lab. It was truly a pleasure to work for you. You've helped me grow immensely as an independent researcher. Your countless wise words of wisdom will resonate with me forever.

I would also like to thank my committee members, Drs. Brian Kirby and Robert Weiss, for their guidance and support of all my work in both research labs.

Thank you to all of the collaborations I have had during my time at Cornell. I especially want to thank Matt Zanotelli, Dr. Francois Bordeleau, Wenjun Wang, Samantha Schwager, Paula Miller, Dr. Ying Wang, Yashira Negron Abril, and Dr. Robert Weiss for collaborating on exciting and challenging research projects.

Special thanks for all those who helped me along my journey in both the Reinhart-King and Shuler labs. I would especially like to thank Dr. Brooke Mason who showed me the ropes in my beginning time in the Reinhart-King lab. Many thanks to Dr. Shawn Carey, Dr. Julie Kohn, and Dr. Marsha Lampi for serving an excellent role models and always answering my countless questions over the years. A very special thank you to Dr. Francois Bordeleau for teaching me everything I know about Western blotting and collaborating on several projects. Many thanks for Matt Zanotelli for all his hard work in troubleshooting experiments and collecting images for publications and this dissertation. Other CRK lab members, past and present, thank you for being fantastic colleagues and friends. Dr. Aniqua Rahman, Dr. Joe Miller, Jacob VanderBurgh, Lauren Hapach, Zach Goldblatt, Emmanuel Lollis, Adam Munoz, Johana Uribe, Marianne Lintz, and Wenjun Wang, I thoroughly enjoyed working with you all.

I am immensely grateful to all of the Shuler lab members who welcomed me into the lab with open arms. In particular, thank you to Paula Miller for teaching me all of the ins and outs of the lab and always willingly helping me through any and every problem I encountered. Many thanks to Dr. Ying Wang for her technical expertise which helped strengthen my work greatly. Dr. Ramin Payoumshariati, Dr. Cristiana Trinconi Tronco, and Chen-Yu Chen, it was a pleasure getting to know you and working with you all.

I must also thank those to encouraged me to pursue a Ph.D. degree in biomedical engineering at Cornell. Thank you to Dr. Shelly Peyton and Thuy Nguyen for guiding

and supporting me during my undergraduate research at UMass. Many thanks to Drs. Kimberly Anderson and Thomas Dziubla and their lab members, Jenn Fischer and David Cochran, for an excellent summer during the Bioengineered Interfaces and Devices REU Program at the University of Kentucky.

I would also like to thank Belinda Floyd, Drs. Chris Schaffer, Jan Lammerding, and Peter Doerschuk for not only ensuring I meet the degree requirements, but talking with me and helping me with hard decisions I've had to make along the way.

Thank you to the National Science Foundation Graduate Research Fellowship Program for financial support of my work. Additionally, thank you to the Cornell NanoScale Science and Technology Facility, and the Biotechnology Resource Center at Cornell for providing essential tools to complete the work within this dissertation.

Many thanks to all of the friends I have made during my time in Ithaca. You certainly made my time at Cornell more enjoyable.

Most importantly, thank you to my parents, Darrell and Judy, my siblings, Lisa and Drew, and my incredible fiancé, Eddie, for your continuous love, support, and encouragement. This journey would not have been possible without each and every one of you.

TABLE OF CONTENTS

Biographical Sketch……. v

Dedication……..... vi

Acknowledgements…… vii

Table of Contents……. x

List of Figures…… xiv

List of Tables…… xvii

List of Abbreviations…….. xviii

List of Symbols……. xxii

Chapter 1: Introduction…….. 1

1.1 Introduction to Cancer……... 1

1.2 Role of the Tumor Microenvironment……... 2

1.3 Organization of the Dissertation…… 4

References…….. 7

Chapter 2: Matrix Stiffness Enhances VEGFR-2 Internalization, Signaling, and Proliferation in Endothelial Cells……. 10

2.1 Abstract…… 10

2.2 Introduction…….. 11

Tumor Angiogenesis…… 11

VEGF in Cancer……... 13

Influence of Matrix Stiffness on Tumor Angiogenesis…… 15

2.3 Materials and Methods……. 20

2.4 Results…….. 26

2.5 Discussion…… 45

2.6 Conclusion……... 50

2.7 Acknowledgments…… 51

References…… 52

Chapter 3: Pumpless, Unidirectional Microphysiological System for Testing Metabolism-Dependent Chemotherapeutic Toxicity…….. 69

3.1 Abstract…… 69

3.2 Introduction…….. 70

Cancer Drug Development……... 70

Tumor Microfluidic Models……. 72

Body-on-a-Chip Technology……... 74

Body-on-a-Chip as Alternative Drug Development Models... 76

3.3 Materials and Methods……. 79

3.4 Results…….. 87

3.5 Discussion…….. 104

3.6 Conclusion……. 108

3.7 Acknowledgments……. 109

References……. 110

Chapter 4: Conclusions and Future Directions……. 129

4.1 Conclusions…… 129

4.2 Future Directions……... 133

Chemical and Mechanical Regulation of Tumor Angiogenesis…….. 133

Current Limitations of Body-on-a-Chip Platforms…… 136

Anti-Angiogenic Drug Testing Within a Body-on-a-Chip Device…… 138

References…….. 141

Appendix A: Additional Results……. 149

A.1 Endothelial Network Formation on Compliant 2D Substrates…….. 149

A.2 Endothelial Permeability with Matrix Stiffness and Fibronectin Cues…… 151

A.3 Isolation of Endothelial Cells from MMTV-PyMT Tumor Tissue… 155

References…….. 161

Appendix B: Protocol for MMTV-PyMT Mouse Tumor Extraction and Isolation of Tumor-Derived Endothelial Cells…….. 164

B.1 Extracting Tumors from MMTV-PyMT Mice……... 164

B.2 Isolation of Tumor Endothelial Cells……. 165

Appendix C: Protocol for Genotyping MMTV-PyMT Mice…….. 171

C.1 Day 1: Tail Snips and Tissue Digestion……. 171

C.2 Day 2: DNA Extraction, PCR, and Gel Electrophoresis……..... 174

LIST OF FIGURES

Chapter 2: Matrix Stiffness Enhances VEGFR-2 Internalization, Signaling, and Proliferation in Endothelial Cells

Figure 2.1. Matrix stiffness enhances VEGF-induced VEGFR-2 response in endothelial cells independently of ECM protein type……. 27

Figure 2.2. VEGFR-2 expression level and clustering decreases with the addition of VEGF and as a function of ECM stiffness……... 30

Figure 2.3. Matrix stiffness elevates VEGFR-2 clustering following VEGF stimulation……... 32

Figure 2.4. Matrix stiffness and VEGF stimulation foster VEGFR-2 colocalization with EEA-1 and decrease cell surface VEGFR-2 levels in endothelial cells…… 34

Figure 2.5. Matrix stiffness does not influence VEGF-stimulated fold change in VEGFR-2 internalization…… 36

Figure 2.6. Matrix stiffness does not influence VEGF-induced VEGFR-2 phosphorylation in confluent endothelial monolayers…… 38

Figure 2.7. Matrix mechanics regulate VEGF-mediated ERK 1/2 phosphorylation and proliferation in sub-confluent cells……... 40

Figure 2.8. VEGF-induced ERK 1/2 phosphorylation is not influenced by ECM compliance in confluent endothelial cells……. 42

Figure 2.9. Matrix stiffness and VEGF stimulate actin stress fiber formation in endothelial cells…….. 44

Chapter 3: Pumpless, Unidirectional Microphysiological System for Testing Metabolism-Dependent Chemotherapeutic Toxicity

Figure 3.1. Three-chamber microphysiological system design……. 88

Figure 3.2. Unidirectional flow within the µCCA……. 92

Figure 3.3. High viability of each cell line cultured within the three-organ microphysiological system…….. 95

Figure 3.4. Cells within the µCCA maintain vital metabolic functions over four days of device operation…….. 96

Figure 3.5. Tegafur and uracil (UFT) combination therapy reduces cancer cell viability……... 98

Figure 3.6. Liver enzymes are required to convert Tegafur to its active metabolites……..... 99

Figure 3.7. Chemotherapeutic efficiency is influenced by cell culture geometry and the presence of flow within the µCCA……... 101

Figure 3.8. Off-target effects of UFT treatment in the multiorgan device induce HL-60 cytotoxicity…… 103

Appendix A: Additional Results

Figure A.1. Endothelial network formation on a compliant substrate……. 150

Figure A.2. Endothelial monolayer permeability increases as a function of matrix stiffness and ECM protein type and concentration…… 153

Figure A.3. Tumors isolated from MMTV-PyMT mice contain a wide variety of cell types……... 156

Figure A.4. CD31 magnetic bead separation of a MMTV-PyMT mouse tumor reveals subpopulations of cells with distinct morphologies….. 158

Figure A.5. DiI-labeled AcLDL can be used as a live-cell fluorescent marker to identify tumor-derived endothelial cells…….... 160

LIST OF TABLES

Chapter 2: Matrix Stiffness Enhances VEGFR-2 Internalization, Signaling, and Proliferation in Endothelial Cells

Table 2.1. A summary of the effects of matrix stiffening on angiogenesis in two-dimensional (2D) and three-dimensional (3D) models…… 18

Chapter 3: Pumpless, Unidirectional Microphysiological System for Testing Metabolism-Dependent Chemotherapeutic Toxicity

Table 3.1. Physiologically-relevant microfluidic chip values were selected using a residence time-based scaling approach from human data…….. 90

Table 3.2. Calculated and measured volumetric flow rates of individual channels within the multiorgan system……... 91

LIST OF ABBREVIATIONS

2D	Two dimensional
3D	Three dimensional
5-FU	5-fluorouracil
AcLDL	Acetylated low-density lipoprotein
ADME	Adsorption, distribution, metabolism, excretion
ANOVA	Analysis of variance
BAEC	Bovine aortic endothelial cell
BAPN	β-aminopropionitrile
bFGF	Basic fibroblast growth factor
BSA	Bovine serum albumin
$CaCl_2$	Calcium chloride
CAF	Cancer-associated fibroblast
CCA	Cell culture analog
CO_2	Carbon dioxide gas
CRC	Colorectal cancer
CYP450	Cytochrome P450
DAPI	4’6-diamidino-2-phenylindole
DMEM	Dulbecco’s Modified Eagle Medium
DMSO	Dimethyl sulfoxide
DNA	Deoxyribonucleic acid
dNTP	Deoxynucleotide triphosphate
DPD	Dihydropyrimidine dehydrogenase
EBM	Endothelial basal medium
EC	Endothelial cell

ECM	Extracellular matrix
EDTA	Ethylenediaminetetraacetic acid
EdU	5-ethynyl-2’-deoxyuridine
EEA-1	Early endosomal antigen-1
EGM	Endothelial growth medium
ELISA	Enzyme-linked immunosorbent assay
eNOS	Endothelial nitric oxide synthase
EpCAM	Epithelial cell adhesion molecule
ERK	Extracellular signal-regulated kinase
FAK	Focal adhesion kinase
FBS	Fetal bovine serum
FDA	Food and Drug Administration
Fn	Fibronectin
FSP1	Fibroblast specific protein 1
HEPES	4-(2-hydroxyethyl)-1-piperazineethanesulfonic acid
HRP	Horse radish peroxidase
HUVEC	Human umbilical vein endothelial cell
IMDM	Iscove’s Modified Dulbecco’s Medium
iPSC	Induced pluripotent stem cell
LSM	Laser scanning confocal microscope
MACS	Magnetic-activated cell sorting
MAPK	Mitogen-activated protein kinase
μCCA	Micro cell culture analog
MEM	Minimal Essential Medium
MMP	Matrix metalloproteinase

MMTV-PyMT	Mouse mammary tumor virus-polyoma virus middle T antigen
MPS	Microphysiological system
NaCl	Sodium chloride
PA	Polyacrylamide
PBPK	Physiologically-based pharmacokinetic
PBS	Phosphate buffered saline
PCR	Polymerase chain reaction
PDMS	Polydimethylsiloxane
PKB	Protein kinase B
PK-PD	Pharmacokinetic-pharmacodynamic
PLGF	Placenta growth factor
PMMA	Poly(methyl methacrylate)
PVDF	Polyvinylidene difluoride
RGD	Arginine-glycine-aspartate
ROCK	Rho-associated coiled-coil kinase
SD	Standard deviation
SDS	Sodium dodecyl sulfate
SE	Standard error
TAE	Tris-acetate-EDTA
TBS	Tris buffered saline
Triton	Octyl phenol ethoxylate
Tween	Polyoxyethylene 20 sorbitan monolaurate
UFT	Tegafur-uracil
UV	Ultraviolet
v/v	volume/volume

VE-cadherin	Vascular endothelial cadherin
VEGF	Vascular endothelial growth factor
VEGFR	Vascular endothelial growth factor receptor
w/v	weight/volume

LIST OF SYMBOLS

Symbol	Description	Units
^{o}C	Degree Celsius	Degree
g	Gravitational constant	$m\ s^{-2}$
h	Channel height	m
Δh	Height difference	m
l	Channel length	m
μ	Dynamic fluid viscosity	$Pa \cdot s$
ΔP	Pressure difference	Pa
Q	Volumetric flow rate	$L\ min^{-1}$
R	Hydrodynamic resistance	$Pa \cdot s \cdot m^{-3}$
ρ	Fluid density	$g\ m^{-3}$
τ	Residence time	min
V	Organ volume	L
w	Channel width	m

CHAPTER 1

INTRODUCTION

1.1 Introduction to Cancer

Cancer is currently the second leading cause of death both worldwide and within the United States. In 2018, an estimated 9.6 million and 600,000 cancer-related deaths are projected worldwide and within the US, respectively [1,2]. In particular, colorectal cancer (CRC) is considered the third most deadly type of cancer worldwide and within the US in both men and women [1,2]. CRC accounted for over 50,000 deaths in the US in 2015 [3], and the gravity of this disease is highlighted by the fact that over 140,000 new cases of CRC are estimated to be diagnosed in the US in 2018 [2]. With the large burden associated with this disease, there is a need to both understand the aberrant biology within the affected cells and develop treatments that can target such aberrant phenotypes with minimal side effects.

To improve cancer treatment, one must understand how cells are altered both in terms of their own biology and the microenvironment they encounter. Cancer cells exhibit many characteristic hallmarks, such as undergoing chronic proliferation, escaping cell death, and inducing angiogenesis [4]. For example, due to its high metabolic activity, a tumor must stimulate angiogenesis to supply the additional oxygen

and nutrients necessary to grow beyond a small size [5,6]. However, these newly formed blood vessels do not just provide vital resources, but they also create a route for cancer cells to travel throughout the body, adhere, and develop into metastatic tumors. Such events are highlighted in importance by the fact that approximately 90% of cancer-related deaths are due to distant metastases, and not the primary tumor [7].

1.2 Role of the Tumor Microenvironment

It is becoming widely known that cancerous tissue is not composed solely by the cancer cells that constitute a portion of the mass. Indeed, the extracellular matrix, other cell types, and soluble signals, in addition to the cancer cells, dictate the tumor microenvironment. Understanding the interplay between different cell types and their immediate surroundings has been a focal point of research in recent years [8,9]. Consequently, it is becoming well understood that most solid tumors arise from normal cells that are transformed to become cancerous, but are also comprised of endothelial cells, pericytes, cancer stem cells, cancer-associated fibroblasts, and immune cells [4]. Thus, the microenvironment is dictated by a largely heterogeneous cell population, and tumor-mediated interactions among distinct cell types, including soluble growth factor secretion and direct cell-cell communication, are pivotal for tumorigenesis [4,10].

It is known that a tumor requires angiogenesis for additional oxygen and nutrients, thereby recruiting nearby endothelial cells and pericytes. Normally quiescent endothelial cells undergo an “angiogenic switch” and become triggered to begin the

process of creating new blood vessels [11,12]. Often, this angiogenic switch can be 'flipped' by cancer cells or other stromal cells as they secrete pro-angiogenic factors to activate endothelial cells [13,14]. Further, this endothelial cell conversion can be fostered by pericytes as they tune endothelial cell phenotype via paracrine signaling [4].

One type of essential cellular interaction for cancer homeostasis is interactions with cancer-associated fibroblasts (CAFs). These cells, including fibroblasts and myofibroblasts, are important in the initiation of cancer and during its progression [15]. CAFs secrete growth factors and cytokines that promote tumor growth [15], as well as synthesize and remodel ECM to create a path for cancer cell invasion and metastasis [16]. Moreover, CAFs facilitate the recruitment of endothelial cells and pericytes to promote tumor angiogenesis [15].

Not only is the local microenvironment important to tumor dynamics, but body-wide factors, such as the immune system, play a critical role in cancer progression or suppression. Certain types of tumor-associated immune cells include T lymphocytes, B cells, dendritic cells, macrophages, leukocytes, and natural killer cells [17]. Often, immune cells fail to recognize and destroy neoplastic cells. In many cases, the initial inflammatory response detects a foreign particle; however, tumor cells often present with host antigens and therefore can evade T cells [17,18]. As such, cancer cells remain elusive and novel treatment strategies aim to reprogram T cells to identify and attack cancer cells throughout the body [19]. Furthermore, the generation of chronic

inflammation by cancer-associated immune cells provides both soluble and matrix cues to further propagate tumor growth [20].

The ECM surrounding a tumor serves as a reservoir of growth factors and matrix proteins that supports numerous activities for cancer and stromal cells. ECM molecules bind to cell surface receptors like integrins, activating intracellular signaling pathways and resulting in changes in proliferation, angiogenesis, invasion, metastasis, and more [21,22]. The dynamic tumor ECM is constantly being remodeled by enzymes such as matrix metalloproteinases [23]. Altogether, while many of the direct and indirect interactions among the diverse cell types within the tumor microenvironment are still unknown, effective cancer treatment strategies must consider attacking the problem from multiple directions.

1.3 Organization of the Dissertation

This dissertation was crafted to expand our current understanding of cellular behaviors within the tumor microenvironment and improve current drug development models to design therapeutics that combat tumor progression. The importance of such research is highlighted by the approval rate of cancer drugs. Currently, only 7 out of every 100 cancer drugs that enter clinical trials eventually gains FDA approval [24], and this exceptionally low rate underlies our need to both understand the molecular mechanisms associated with cancer as well as our ability to translate this understanding into clinically-relevant drug screening models. Thus, the overall goal of this thesis is to

elucidate the effects of cues found within the tumor microenvironment on multiple levels.

In Chapter 2, I present data focused on understanding the signaling and mechanobiology associated with tumor angiogenesis. In this study, I investigated endothelial cell response to multiple tumor-specific factors. Specifically, endothelial cell signaling and behavior was investigated when simultaneous chemical and mechanical stimuli were present, exposing crosstalk between signaling pathways that would not have been identified by studying either factor individually. Importantly, identifying crucial parameters within the tumor microenvironment that promote aberrant cell behavior and cancer progression may reveal new, potential drug targets.

In Chapter 3, I present data to expand current models of cancer drug screening to translate findings like those in Chapter 2 (i.e. therapeutic targets) to physical systems. In doing so, I developed a human body-on-a-chip device, based on human parameters, as a platform to examine the influence of tumor-specific cues on chemotherapeutic-induced cytoxicity. Such physiologically-relevant devices can better identify non-efficacious or toxic compounds that generate side effects during initial drug screening compared to current preclinical models [25]. Further, this approach is translatable to other tumor models to test novel therapeutics or combination regimens that target multiple cell types within the tumor stroma.

In Chapter 4, conclusions and future directions are presented. Broadly, the work contained in this dissertation represents a main thrust of biomedical engineering. That is, the main chapters focus both on basic science and clinical translation of research in a cancer research context. While, this dissertation represents one endeavor in each of the basic science and translational realm, this process is certainly iterative. Looking forward, the data presented here will inform future studies to extend our comprehensive understanding of cancer biology and treatment.

While Chapters 2 and 3 present the bulk of the original research I conducted in developing this dissertation, I have also included Appendix A containing additional results generated during my time at Cornell, which may inform future experiments. Specifically, I include preliminary data (Appendix A) and a protocol to isolate endothelial cells from tumors (Appendix B). In connecting Chapters 2 and 3, that is the basic science to clinically-relevant screening modalities, one must be able to properly isolate distinct cell populations to both study cellular processes and create more authentic body-on-a-chip systems. With this motivation, I devoted substantial time to develop a protocol to isolate tumor-derived endothelial cells from the MMTV-PyMT mouse model to investigate inherent differences of disease-mediated cells and their response to changes in matrix stiffness.

REFERENCES

1. http://www.who.int/news-room/fact-sheets/detail/cancer.
2. Siegel RL, Miller KD, Jemal A. Cancer Statistics, 2018. CA Cancer J Clin. 2018;68(1):7–30.
3. Siegel RL, Miller KD, Jemal A. Cancer Statistics, 2017. CA Cancer J Clin. 2017;67(1):7–30.
4. Hanahan D, Weinberg RA. Hallmarks of Cancer: The Next Generation. Cell. 2011;144:646–74.
5. Chauhan VP, Stylianopoulos T, Boucher Y, Jain RK. Delivery of molecular and nanoscale medicine to tumors: transport barriers and strategies. Annu Rev Chem Biomol Eng. 2011;2:281–98.
6. Gimbrone Jr MA, Leapman SB, Cotran RS, Folkman J. Tumor dormancy in vivo by prevention of neovascularization. J Exp Med. 1972;136:261–76.
7. Chaffer CL, Weinberg RA. A Perspective on Cancer Cell Metastasis. Science. 2011;331:1559–64.
8. Discher DE, Janmey P, Wang Y-L. Tissue cells feel and respond to the stiffness of their substrate. Science. 2005;310:1139–43.
9. Chin LK, Xia Y, Discher DE, Janmey PA. Mechanotransduction in cancer. Curr Opin Chem Eng. 2016;11:77–84.
10. Fukumura D, Jain RK. Tumor microvasculature and microenvironment: targets for anti-angiogenesis and normalization. Microvasc Res. 2007;74:72–84.
11. Hanahan D, Folkman J. Patterns and emerging mechanisms of the angiogenic switch during tumorigenesis. Cell. 1996;86(3):353–64.

12. Bergers G, Benjamin LE. Tumorigenesis and the angiogenic switch. Nat Rev Cancer. 2003;3:401–10.

13. Senger DR, Perruzzi CA, Feder J, Dvorak HF. A Highly Conserved Vascular Permeability Factor Secreted by a Variety of Human and Rodent Tumor Cell Lines. Cancer Res. 1986;46:5629–32.

14. Fukumura D, Xavier R, Sugiura T, Chen Y, Park EC, Lu N, Selig M, Nielsen G, Taksir T, Jain RK, Seed B. Tumor induction of VEGF promoter activity in stromal cells. Cell. 1998;94:715–25.

15. Kalluri R, Zeisberg M. Fibroblasts in cancer. Nat Rev Cancer. 2006;6(May):392–401.

16. Xing F, Saidou J, Watabe K. Cancer associated fibroblasts (CAFs) in tumor microenvironment. Front Biosci. 2010;15(2):166–79.

17. Whiteside TL. The tumor microenvironment and its role in promoting tumor growth. Oncogene. 2008;27(45):5904–12.

18. Allard B, Aspeslagh S, Garaud S, Dupont FA, Solinas C, Kok M, Routy B, Sotiriou C, Stagg J, Buisseret L. Immuno-oncology-101: overview of major concepts and translational perspectives. Semin Cancer Biol. 2018;52:1–11.

19. Almåsbak H, Aarvak T, Vemuri MC. CAR T Cell Therapy: A Game Changer in Cancer Treatment. J Immunol Res. 2016;2016:5474602.

20. de Visser KE, Eichten A, Coussens LM. Paradoxical roles of the immune system during cancer development. Nat Rev Cancer. 2006;6(1):24–37.

21. Lu P, Weaver VM, Werb Z. The extracellular matrix: A dynamic niche in cancer progression. J Cell Biol. 2012;196(4):395–406.

22. Pickup MW, Mouw JK, Weaver VM. The extracellular matrix modulates the hallmarks of cancer. EMBO Rep. 2014;15(12):1243–53.

23. Kessenbrock K, Plaks V, Werb Z. Matrix Metalloproteinases: Regulators of the Tumor Microenvironment. Cell. 2010;141:52–67.

24. Hay M, Thomas DW, Craighead JL, Economides C, Rosenthal J. Clinical development success rates for investigational drugs. Nat Biotechnol. 2014;32(1):40–51.

25. Esch MB, King TL, Shuler ML. The Role of Body-on-a-Chip Devices in Drug and Toxicity Studies. Annu Rev Biomed Eng. 2011;13:55–72.

CHAPTER 2

MATRIX STIFFNESS ENHANCES VEGFR-2 INTERNALIZATION, SIGNALING, AND PROLIFERATION IN ENDOTHELIAL CELLS

Portions of this chapter were published in *Advances in Regenerative Biology* [1] and *Convergent Science Physical Oncology* [2]

2.1 Abstract

Vascular endothelial growth factor (VEGF) can mediate endothelial cell migration, proliferation, and angiogenesis. During cancer progression, VEGF production is often increased to stimulate the growth of new blood vessels to supply growing tumors with the additional oxygen and nutrients they require. Extracellular matrix stiffening also occurs during tumor progression, however, the crosstalk between tumor mechanics and VEGF signaling remains poorly understood. Here, we show that matrix stiffness heightens downstream endothelial cell response to VEGF by altering VEGF receptor-2

[1] LaValley DJ, Reinhart-King CA. Matrix stiffening in the formation of blood vessels. Adv Regen Biol 2014; 1(1): 25247.

[2] LaValley DJ, Zanotelli MR, Bordeleau F, Wang W, Schwager SC, Reinhart-King CA. Matrix stiffness enhances VEGFR-2 internalization, signaling, and proliferation in endothelial cells. Converg Sci Phys Oncol 2017; 3(4): 044001.

Author Contributions: D.J.L., M.R.Z., F.B., C.A.R.-K. designed research. D.J.L., M.R.Z., W.W., S.C.S. performed research. D.J.L., M.R.Z. analyzed data. D.J.L., C.A.R.-K. wrote the paper. M.R.Z. edited the paper.

(VEGFR-2) internalization, and this effect is influenced by cell confluency. In sub-confluent endothelial monolayers, VEGFR-2 levels, but not VEGFR-2 phosphorylation, are influenced by matrix rigidity. Interestingly, more compliant matrices correlated with increased expression and clustering of VEGFR-2; however, stiffer matrices induced increased VEGFR-2 internalization. These effects are most likely due to actin-mediated contractility, as inhibiting ROCK on stiff substrates increased VEGFR-2 clustering and decreased internalization. Additionally, increasing matrix stiffness elevates ERK 1/2 phosphorylation, resulting in increased cell proliferation. Moreover, cells on stiff matrices generate more actin stress fibers than on compliant substrates, and the addition of VEGF stimulates an increase in fiber formation regardless of stiffness. In contrast, once endothelial cells reached confluency, stiffness-enhanced VEGF signaling was no longer observed. Together, these data show a complex effect of VEGF and matrix mechanics on VEGF-induced signaling, receptor dynamics, and cell proliferation that is mediated by cell confluency.

2.2 Introduction

Tumor Angiogenesis

Angiogenesis is the process by which new blood vessels develop from existing vasculature. It is typically a healthy process that occurs only during fetal development and wound healing in adults, but can become dysregulated during diseases, such as cancer [1]. During angiogenesis, the existing vessel is destabilized and the local extracellular matrix (ECM) is degraded and remodeled by matrix metalloproteinases.

Pro-angiogenic factors, such as vascular endothelial growth factor (VEGF), stimulate endothelial cell (EC) proliferation and migration, after which ECs re-establish cell-cell contacts with neighboring cells. Once sufficient proliferation has occurred, ECs form tube-like structures. Mesenchymal cells are recruited to the new vessel where they proliferate, migrate, and differentiate into pericytes. Finally, the vessel matures and stabilizes, and ECs return to a normal, quiescent state [2,3].

While normal angiogenesis is regulated by a balance between pro-and anti-angiogenic cues, this balance becomes dysregulated during cancer [1]. Despite utilizing many of the same mechanisms involved in normal angiogenesis, cancerous cells stimulate angiogenic responses that result in the formation of structurally abnormal blood vessels [2]. Tumor-associated vessels are known to be hyperpermeable, immature, and organized in tortuous patterns [1,4]. Moreover, vessels can be often become compressed due to the large tumor burden, and insufficient blood flow leads to a hypoxic, acidic tumor core [5]. Further, the abnormal vascular geometries promote chaotic blood flow and high interstitial fluid pressure gradients [5]. Collectively, the abnormalities in tumor vasculature can inhibit effective chemotherapeutic delivery [5,6].

As a result of the aberrant vasculature formed within malignant tissue, traditional anti-angiogenic treatment strategies aim to eradicate existing blood vessels surrounding tumors and prevent the formation of new ones. However, cancer cells are thus forced to leave the primary tumor site in search of oxygen and vital nutrients,

thereby promoting metastasis [7,8]. Additionally, without a proper oxygen supply, hypoxia develops or worsens within the cancerous tissue, consequently upregulating the production of pro-angiogenic factors, such as VEGF, which in turn, generates a feed-forward loop to further drive tumor angiogenesis [9]. Furthermore, VEGF-targeted therapies often develop resistance due to activation or upregulation of alternative pro-angiogenic pathways [10,11]. As such, an emerging cancer treatment strategy, pioneered by Rakesh Jain, seeks to "normalize" the tumor-associated vasculature by restoring the imbalance between pro- and anti-angiogenic cues to increase the delivery and efficacy of therapeutics [12,13]. This approach requires an optimal dosing and timing schedule of carefully selected anti-angiogenic drugs [14].

VEGF in Cancer

VEGF is one of the many molecules extensively involved in both healthy and tumor-associated angiogenesis [2]. In mammals, there exist five VEGF ligands, VEGF-A, VEGF-B, VEGF-C, VEGF-D, and placenta growth factor (PLGF) which bind to three VEGF receptors (VEGFRs), VEGFR-1, VEGFR-2, and VEGFR-3 [15]. Angiogenesis is predominantly mediated through the interaction of VEGF-A with VEGFR-2 [3]. Activation of VEGFR-2, through ligand binding or mechanical stimuli such as shear stress, requires receptor dimerization and trans-autophosphorylation on intracellular tyrosine residues [15]. Downstream signals, such as focal adhesion kinase (FAK), extracellular signal-regulated kinase (ERK) 1/2, protein kinase B (PKB/Akt), and endothelial nitric oxide synthase (eNOS), are then activated and mediate crucial endothelial cell behaviors [15].

VEGF stimulation can result in numerous phenotypic changes within endothelial cells. High levels of VEGF are needed for tubulogenesis initiation and the maintenance of these tubule-like structures *in vitro* [16–18]. Interestingly, established endothelial networks on compliant matrices are disrupted with the addition of growth factors like VEGF [18,19]. The addition of VEGF leads to coordinated EC migration [20–22] and proliferation [23–30] under several conditions. While VEGFR-2-mediated EC migration can exploit several intracellular pathways, VEGF-stimulated endothelial proliferation is classically mediated through the mitogen-activated protein kinase (MAPK) cascade [15]. Furthermore, VEGF-enhanced vascular permeability has been extensively studied [31–37], which emphasizes that continuous VEGF signaling further propagates the formation of hyperpermeable blood vessels within the tumor microenvironment.

Notably, VEGF is considered to be a major contributing factor in promoting aberrant tumor vasculature [1,38]. Historically, VEGF was discovered in tumors and initially called vascular permeability factor [38]. To initiate angiogenesis, tumor cells can either secrete VEGF directly [39] or stimulate stromal cell secretion [40]. Consequently, elevated levels of VEGF are frequently reported in cancer patients, and correlate with the degree of vascularity, proliferation, and malignancy [41,42]. As such, anti-VEGF therapeutics have been developed [43–45] for use as single therapy or in combination regimens with chemotherapeutics for cancer treatment [46].

Influence of Matrix Stiffness on Tumor Angiogenesis

The ECM serves as both a reservoir of matrix proteins and a structural scaffold to support EC organization and stabilization during blood vessel formation [47]. However, it also serves a mechanical function, as the stiffness of the matrix can dictate the nature and extent of angiogenesis. Normally it is tightly regulated during tissue homeostasis, but becomes highly deregulated and continuously remodeled during diseases, such as cancer [48].

2D and 3D Regulation of Vascular Growth and Integrity by Matrix Stiffness

Cells are capable of sensing and responding to changes in matrix stiffness [49], which in turn, regulates angiogenesis. Significant work has been done using deformable 2D substrates to show that ECs form capillary-like networks on compliant substrates, but not on stiffer matrices [18,19,47,50,51]. Using planar substrates of tunable stiffness, several groups, including our own, have observed that ECs form capillary networks on compliant matrices independently of exogenously applied growth factors [19,47,50,51]. Cells are thought to sense one another and communicate mechanically through the ECM, facilitating the formation of cell-cell junctions during tissue formation [52]. Compliant substrates induce enhanced EC elongation and alignment [47,50], whereas increasing 2D matrix stiffness decreases network formation [19,50] and sprouting [18]. Conversely, decreasing stiffness results in decreased matrix metalloproteinase (MMP) expression and increased network formation [16]. Furthermore, more EC proliferation was observed on stiffer matrices than on more compliant substrates [53]. Overall, data

in 2D suggest that compliant matrices foster the self-assembly and growth of vascular networks.

Although most studies report that elevated matrix stiffness on 2D substrates inhibits network formation [18,19,47,50,51], results differ in 3D matrices. Increased matrix density, which results in increased stiffness, is reported to reduce neovascularization and capillary network formation [54,55], resulting in shorter, thicker, slower growing sprouts, fewer branch points, and reduced network connectivity [17,55], but more stable lumen formation [17]. Importantly, there exists a collagen density above which vessels no longer form [17]. It is crucial to note, however, that in these studies stiffness is regulated by density.

Stiff, 3D, collagen matrices can also be fabricated by cross-linking collagen gels, in which case the collagen density and gel pore size remain constant. For example, Yamamura et al. [56] reported thicker, deeper capillary networks on rigid 3D collagen gels and the formation of large, multicellular lumens. In a 3D spheroid model, cell spreading, the number and length of EC sprouts, and overall angiogenic outgrowth increased as a function of stiffness in 3D when stiffness was modulated by collagen glycation [57]. In a similar study, increasing matrix stiffness increased angiogenic outgrowth and branching in a 3D spheroid model, β-aminopropionitrile (BAPN)-treated mouse model, and *ex ovo* chick embryo model [58]. However, separate experiments have shown that stiffening collagen delays EC sprouting and increases resistance to matrix degradation during remodeling [59].

It is hypothesized that, in 3D, matrix stiffness alters EC force generation that is critical for early sprouting morphogenesis [60,61] and is required for later maintenance stages as well [61]. Additionally, stiffness is thought to regulate MMP production, as it has been shown that increasing stiffness results in increased MMP expression and decreased microvascular density [62]. Together, these data underscore the need to parse apart the effects of density from stiffness in both 2D and 3D (Table 1).

To better mimic the *in vivo* microenvironment, microfabrication approaches are capable of introducing complex topographies into gels of tunable stiffness to investigate the combined effects of stiffness and topography on angiogenesis. Sun et al. [51] showed that ECs formed denser, shorter cord networks near a physical boundary compared to regions without boundaries. In our own work, we have demonstrated that topography in compliant or stiff gels can induce EC alignment [63]. Collectively, these microfabricated systems create more complex, realistic geometries than those found in typical 2D assays without the density and stiffness issues that are at play in 3D matrices.

To complement these experimental approaches, computational modeling has been used to predict the effects of ECM stiffness on angiogenesis [55,64,65]. Computationally, increasing matrix density and network connectivity were shown to decrease sprout extension speed and alter morphology [64,66]. The models can predict the optimal protein density to maximize sprout extension speed [64], and simulate individual ECs forming sprouts [66].

Table 2.1. A summary of the effects of matrix stiffening on angiogenesis in two-dimensional (2D) and three-dimensional (3D) models.

Parameter	2D	3D
Network formation	Decreases with increasing stiffness [16,19,50]; networks present on compliant matrices but not on stiff substrates [18,19,47,50,51]	Decreases with increasing ECM density [17,54,55,59]; thicker, deeper networks with increasing stiffness [56]
EC elongation and sprouting	EC elongation decreases with increasing stiffness [47,50]	Sprouting and outgrowth increases with increasing glycation of ECM proteins [57,58]
Lumen formation	Larger lumens formed on stiffer gels [60]	Form more stable lumens with increased stiffness [17]; large lumens on rigid gels [56]
MMP expression	Decreases with decreasing stiffness, resulting in increased EC elongation [16]	Increases with increasing stiffness [58,62], resulting in decreased vessel density [62]
EC proliferation	Increases with increasing stiffness [53]	No change in proliferation with increasing protein glycation [57]

Elevated Matrix Stiffness During Cancer Progression

In addition to the abnormal growth of blood vessels in the tumor microenvironment, many other microenvironmental changes are known to occur during tumor progression that can influence tumor growth. One such change is an increase in ECM stiffness within the tumor due to increased ECM protein production and increased crosslinking of existing matrix proteins, via the action of enzymes like lysyl oxidase, within the tumor stroma [67,68]. Together, these numerous microenvironmental changes can highly influence tumor and stromal cell behavior and further promote cancer progression.

Stiffness has been shown to influence numerous aspects of tumor angiogenesis including capillary sprouting [69,70] and malignancy [71]. In normoxic conditions, increased stiffness reduces EC sprouting and invasion [69], whereas under hypoxic conditions, there is increased sprouting compared to normoxia regardless of stiffness [69]. Studies within the vascular biology community have suggested that increased matrix stiffness can also disrupt vascular integrity by increasing EC contractility and disrupting EC-EC adhesion [72,73]. In general, matrix stiffness has been shown to affect endothelial gene expression [74,75], morphology [17,18,50,76], outgrowth [57], traction forces [73,77,78], and permeability [37,58,78,79], which may significantly influence tumor angiogenesis.

Cellular behavior is determined by the complex integration of numerous chemical and mechanical cues [65,80]. While some have begun to delineate the

pathways of these chemical and mechanical cues and identify crosstalk mechanisms [16,81–87], most are not yet fully understood. Altered matrix mechanics are known to influence cell behaviors [49,88] mainly through crosstalk between integrins and the Rho/ROCK pathway [89]. Here, the combined effects of matrix rigidity and VEGF stimulation on endothelial cell behavior were investigated. Our data indicate that ECM stiffness increases endothelial cell VEGFR-2 internalization and downstream VEGF-stimulated signaling, proliferation, and stress fiber formation.

2.3 Materials and Methods

Cell Culture

Human umbilical vein endothelial cells (HUVECs) were purchased from Lonza (Walkersville, MD). They were maintained and plated at 37^{o}C and 5% CO_2 in endothelial growth medium (EGM; Lonza) supplemented with the EGM BulletKit^{TM} (2% v/v FBS, Bovine Brain Extract, Ascorbic Acid, Hydrocortisone, Epidermal Growth Factor, Gentamicin/Amphotericin-B; Lonza). HUVECs were used at passage 4 for all experiments.

Polyacrylamide Gel Fabrication

Polyacrylamide (PA) gels were fabricated as described elsewhere [50,73,90]. Briefly, the ratio of acrylamide (40% w/v; Bio-Rad, Hercules, CA) and bis-acrylamide (2% w/v; Bio-Rad) was varied to tune gel stiffness from 1 to 10 kPa to mimic vascular and tumorous tissue as described previously [58,73,91]. Gels were coated with either 0.1 mg

mL^{-1} collagen type I (BD Biosciences, San Jose, CA) or fibronectin (Thermo Fisher Scientific, Waltham, MA).

Western Blot

The seeding density of HUVECs atop PA gels or collagen-coated glass coverslips was optimized to achieve either 50-70% confluency after one day or full confluence after 2-4 days. Cells were stimulated with 5 ng mL^{-1} human recombinant $VEGF_{165}$ (R&D Systems, Minneapolis, MN) for the desired time, rinsed with ice cold phosphate buffered saline (PBS), and lysed with 6x SDS sample buffer (4x Tris-Cl/SDS, pH 6.8, 30% v/v glycerol, 10% w/v SDS, 0.09% v/v 2-mecaptoethanol, and 0.012% w/v Bromophenol Blue) [92]. For Western blotting, lysates were run with 8% w/v acrylamide gels on a Mini-PROTEAN Tetra System (Bio-Rad) and electrotransferred onto a PVDF membrane (Bio-Rad). Membranes were blocked in 5% w/v BSA (Sigma-Aldrich, St. Louis, MO) or milk (Nestle) in 0.1% v/v Tris-buffered saline (TBS)-polyoxyethylene 20 sorbitan monolaurate (Tween; JT Baker, Phillipsburg, NJ) for 1 h. Membranes were then incubated overnight at $4^{o}C$ with antibodies against phosphorylated VEGFR-2 (p-VEGFR-2) at Y1175 (1:1000; #3770; Cell Signaling Technology, Beverly, MA) or phosphorylated ERK 1/2 (p-ERK 1/2) at T202/Y204 (1:2000; #9106; Cell Signaling Technology). Goat anti-mouse or goat anti-rabbit horse-radish-peroxidase (HRP)-conjugated antibodies (1:2000; Rockland Immunochemicals, Limerick, PA) were incubated for 1 h at room temperature. After the addition of SuperSignal™ chemiluminescent substrate (Thermo Fisher Scientific), blots were imaged using a FujiFilm ImageQuant LAS-4000 (FujiFilm Life Science). Following

imaging, membranes were stripped with Restore Stripping Buffer (Thermo Fisher Scientific), re-blocked, and probed with antibodies against total VEGFR-2 (1:1000; #sc-6251; Santa Cruz Biotechnology, Santa Cruz, CA) or total ERK 1/2 (1:1000; #9102; Cell Signaling Technology) followed by goat anti-mouse or goat anti-rabbit HRP-conjugated secondary antibodies (1:2000; Rockland Immunochemicals). Lastly, α-tubulin (1:20,000; #05-829; Millipore, Billerica, MA) was stained as a loading control. Densitometry analysis was performed in ImageJ.

VEGFR-2 Immunofluorescence and Analysis

HUVECs were pretreated with Y-27632 (5 μM; BioVision, Milpitas, CA) or DMSO vehicle (Sigma-Aldrich) for 12 h. Cells were stimulated with 5 ng mL^{-1} VEGF (R&D Systems) for 15 min, rinsed with PBS, and then immediately fixed with 3.2% v/v paraformaldehyde (Electron Microscopy Systems, Hatfield, PA) for 10 min. After being washed with 0.02% v/v Tween (JT Baker) in PBS, HUVECs were permeabilized with 0.1% v/v Triton X-100 (JT Baker) in PBS with 5% v/v donkey serum (Millipore) for 20 min. Cells were blocked in 5% v/v donkey serum (Millipore) in PBS for 1 h and then incubated with VEGFR-2 antibody (1:50; #ab9530; Abcam, Cambridge, MA) in 0.01% v/v Triton X-100 (JT Baker), 5% v/v donkey serum (Millipore) in PBS overnight at 4°C. Alexa Fluor 488 donkey anti-mouse antibody (1:200; Thermo Fisher Scientific) was incubated for 1 h. Nuclei were counterstained with 4',6-diamidino-2-phenylindole (DAPI; 1:500; Thermo Fisher Scientific). To image, gels were inverted onto a drop of Vectashield™ Mounting Media (Vector Laboratories, Burlingame, CA) placed on a thin coverslip (No. 1, 48x65 mm, Thermo Fisher Scientific). Fluorescent z-stack images of

each sample were acquired with a 40x water-immersion objective on a Zeiss LSM 700 confocal microscope on a Zeiss Axio Observer Z1 inverted stand (Carl Zeiss, Oberkochen, Germany). Images are presented as maximum intensity projections of z-stacks, unless otherwise stated. For analysis, cells were outlined in ImageJ and mean fluorescence intensity was measured. Additionally, the average number and size of VEGFR-2 clusters was calculated in ImageJ by thresholding images, analyzing particles, and normalizing per nucleus.

Colocalization of VEGFR-2 with EEA-1

Sub-confluent HUVECs were seeded on 1 and 10 kPa collagen-coated gels. One day post seeding, cells were pretreated with 5 μM Y-27632 (BioVision) or DMSO vehicle (Sigma-Aldrich) for 12 h. Following 15 min VEGF (R&D Systems) incubation, cells were fixed and co-stained with VEGFR-2 primary antibody (1:50; #ab9530; Abcam) and early endosomal antigen-1 (EEA-1) primary antibody (1:50; #ab2900; Abcam) as described above. Alexa Fluor 488 donkey anti-mouse and Alexa Fluor 568 donkey anti-rabbit secondary antibodies (1:200; Thermo Fisher Scientific) were utilized. Cells were counterstained with DAPI (1:500; Thermo Fisher Scientific) to visualize nuclei. Gels were inverted onto glass coverslips and a z-stack image of each sample was captured using a Zeiss LSM 700 confocal microscope equipped with a 40x water-immersion objective. Analysis was performed utilizing a custom-written Matlab code previously described [77] with slight modifications. Briefly, VEGFR-2 and EEA-1 z-stack images were converted into image sequences in ImageJ. In Matlab, image sequences were subjected to an adaptive Weiner filter (0.78 μm filtering window) to remove background

noise, and then image sections with structures presenting a signal-to-noise ratio greater than 2:1 were subjected to a top-hat filter (0.78 μm diameter disc). A median filter (0.63 μm filtering window) was applied to correct for variations in intensity. VEGFR-2 and EEA-1 colocalization was quantified by overlaying corresponding VEGFR-2 and EEA-1 filtered images to generate a 3D overlapping volume data. The number of colocalization events for each image was then normalized per cell.

Surface-Bound VEGFR-2 Immunofluorescence

Sub-confluent HUVECs were pretreated with 5 μM Y-27632 (BioVision) or DMSO vehicle (Sigma-Aldrich) for 12 h and then stimulated with 5 ng mL^{-1} VEGF (R&D Systems) for 15 min. Cells were fixed and stained with VEGFR-2 (1:50; #ab9530; Abcam) as described above, however, omitting cell permeabilization with Triton X-100 and wash steps involving Tween to visualize only membrane-bound VEGFR-2. Nuclei were counterstained with DAPI (1:500; Thermo Fisher Scientific). Fluorescent images were captured with a 40x water-immersion objective on a Zeiss LSM 700 confocal microscope. The number of VEGFR-2 clusters on the cell surface was calculated in ImageJ as described previously, and reported per cell.

Proliferation Assay

One day post seeding, sub-confluent HUVECs were serum starved in EBM (Lonza) for 24 h. PD98059 (10 or 20 μM; Cell Signaling Technology) or DMSO vehicle (Sigma-Aldrich) was added to the cells for the final hour of serum starving. Cells were stimulated with 5 ng mL^{-1} VEGF (R&D Systems) in 0.1% v/v FBS in EBM for 20 h.

10 μM 5-ethynyl-2'-deoxyuridine (EdU; Thermo Fisher Scientific) was added for 4 h and cells were fixed with 3.7% v/v formaldehyde (Alfa Aesar, Ward Hill, MA) for 15 min. HUVECs were stained with the Click-iT EdU Kit (Thermo Fisher Scientific) following the manufacturer's instructions and nuclei were counterstained with DAPI (1:500; Thermo Fisher Scientific). Cells were imaged with a 10x objective on a Zeiss Axio Observer Z1 inverted phase-contrast microscope (Carl Zeiss) with a Hamamatsu ORCA-ER camera. The percentage of EdU incorporation was calculated as the ratio of EdU positive cells to the total number of cells. Cell counts from 15 representative fields of view are also reported.

Actin Stress Fiber Immunofluorescence

Sub-confluent HUVECs seeded on collagen-coated 1 and 10 kPa PA gels were stimulated with 5 ng mL^{-1} VEGF (R&D Systems) for 15 min and then fixed with 3.7% v/v formaldehyde (Alfa Aesar) for 10 min. Cells were washed with 0.02% v/v Tween (JT Baker) in PBS and permeabilized for 5 min with 1% v/v Triton X-100 (JT Baker) in PBS before being incubated with Alexa Fluor 488 phalloidin (1:100; Thermo Fisher Scientific) and DAPI (1:500; Thermo Fisher Scientific) for 30 min at room temperature. Fluorescent z-stack images were obtained with a Zeiss LSM 700 confocal microscope on a Zeiss Axio Observer Z1 inverted stand (Carl Zeiss) equipped with a 40x water-immersion objective. The average number of stress fibers per cell was quantified using the ImageJ Tubeness plugin, as described previously [93].

Statistical Analysis

All analyses were performed using GraphPad Prism 7 (GraphPad Software, La Jolla, CA) or Excel 2016 (Microsoft, Redmond, WA). Where appropriate, student's *t*-tests or parametric one-way or two-way ANOVAs with post hoc Tukey's honest significant difference test were performed. $P < 0.05$ was considered statistically significant. All values are presented as mean $\pm$ standard error (SE).

2.4 Results

Matrix stiffness enhances VEGF-induced VEGFR-2 response in sub-confluent endothelial monolayers

To investigate the interplay of signaling pathways activated by both VEGF and ECM stiffness, we first probed VEGFR-2 activation. To represent healthy blood vessels, sub-confluent HUVECs were cultured on 1 kPa PA substrates [94]. Since matrix stiffening occurs during tumor progression [67,68], 10 kPa gels were utilized to mimic tumor tissue. After HUVECs were seeded onto 1 and 10 kPa gels and subjected to 5 min of 5 ng mL^{-1} VEGF stimulation, activated VEGFR-2 levels (ratio of Y1175 phosphorylated VEGFR-2 (p-VEGFR-2) to total VEGFR-2) was significantly increased on stiffer matrices (Figure 2.1A-B,D-E). This response was independent of whether the cells were cultured on collagen-coated (Figure 2.1A-C) or fibronectin-coated (Figure 2.1D-F) matrices, although the magnitude of the response was much more robust for cells cultured on collagen. Interestingly, no changes were observed in the level of p-

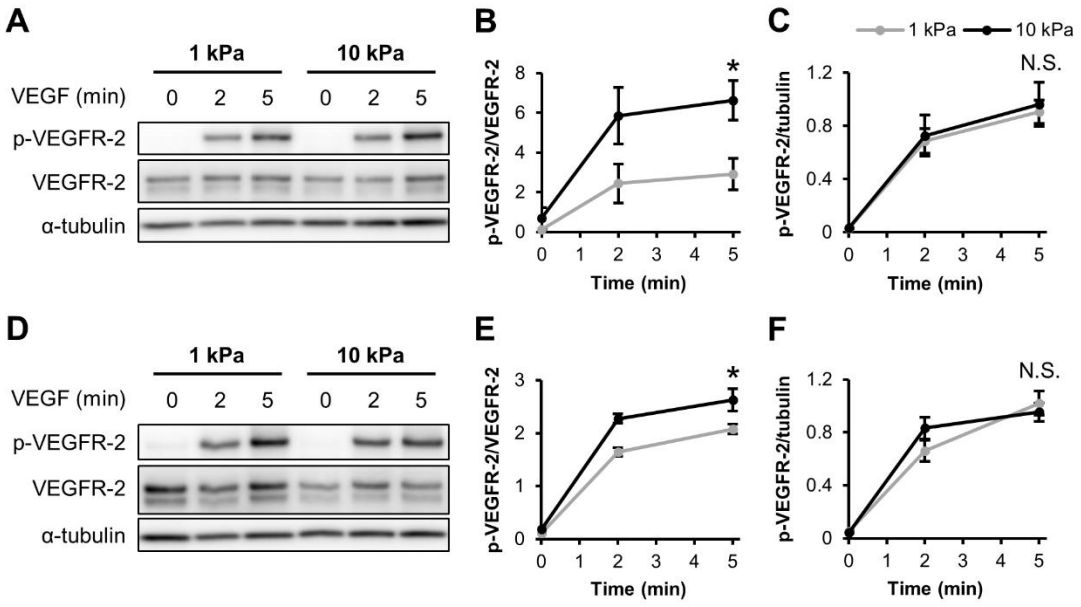

Figure 2.1. Matrix stiffness enhances VEGF-induced VEGFR-2 response in endothelial cells independently of ECM protein type. (A-C) Sub-confluent HUVECs cultured on collagen-coated gels were stimulated with 5 ng/ml VEGF for the indicated amounts of time and probed for Y1175 VEGFR-2 phosphorylation and VEGFR-2 expression using a Western blot (A) with corresponding densitometry quantification (B-C). (D-F) Same as in (A-C) but HUVECs were cultured on fibronectin-coated substrates and analyzed for p-VEGFR-2 and VEGFR-2 using Western blot (D) and densitometry (E-F). α-tubulin was used as a loading control. Plots are mean ± SE. N = 3 independent sets of lysates. * $p<0.05$ from student's *t*-test. N.S. not significant.

VEGFR-2 relative to the housekeeping gene, α-tubulin (Figure 2.1C,F), demonstrating no stiffness-mediated changes in the level of p-VEGFR-2 in HUVECs.

Next, we investigated VEGFR-2 expression with and without VEGF simulation as a function of ECM stiffness. Sub-confluent cells on stiffer substrates had significantly less VEGFR-2 compared to compliant matrices both without VEGF treatment (control) and after 15 min VEGF treatment (VEGF; Figure 2.2A-B). Additionally, we observed a decrease in VEGFR-2 expression after 15 min for both stiffness values tested (Figure 2.2A-B). However, the fold decrease in VEGFR-2 levels after stimulation with VEGF (VEGF/control) was independent of ECM stiffness (Figure 2.2B). These results confirm the findings of Mammoto et al. [74] which demonstrated that matrix stiffness modulates VEGF-independent VEGFR-2 expression in endothelial cells cultured on fibronectin-coated PA substrates, and further suggest a decrease in VEGFR-2 following VEGF stimulation.

The addition of VEGF to endothelial cells rapidly initiates VEGFR-2 endocytosis, an important step in downstream VEGF signaling [95,96]. Since endocytosis in stem cells can be influenced by matrix stiffness [97], we sought to determine the effect of stiffness on VEGF-stimulated VEGFR-2 endocytosis in endothelial cells. Cells cultured on 1 and 10 kPa collagen-coated PA gels were subjected to 15 min VEGF stimulation, fixed, and immunostained for VEGFR-2 (Figure 2.2C). Indeed, total fluorescence intensity of VEGFR-2 significantly decreased with increasing matrix stiffness (Figure 2.2D). Total fluorescence intensity of VEGFR-2 also decreased

following VEGF stimulation at each stiffness (Figure 2.2D). Moreover, VEGF treatment induced VEGFR-2 clustering (Figure 2.2C, arrows), where the average size of VEGFR-2 clusters increased with VEGF stimulation regardless of ECM stiffness (Figure 2.2E), suggesting receptor aggregation and packaging for endocytosis [95]. VEGFR-2 clusters were more numerous and larger in size following VEGF treatment in cells on more compliant substrates compared to cells on stiffer substrates (Figure 2.2E-F). The fold change in VEGFR-2 cluster size, but not intensity or cluster number, from the addition of VEGF (VEGF/control) increased on stiff matrices compared to compliant substrates (Figure 2.3), indicating stiffness increased cluster size in response to VEGF but not the number or intensity of clusters. Since matrix stiffness has been shown to regulate cell behavior and signaling via the Rho/ROCK pathway [73,81], we also investigated its role in VEGFR-2 localization and clustering. Pretreatment of HUVECs on 10 kPa gels with Y-27632, a ROCK inhibitor [98], abrogated the reduced VEGFR-2 signal, cluster size, and cluster number compared to untreated cells on stiff substrates (Figure 2.2C-F). Cells on stiff substrates that were treated with Y-27632 exhibited VEGFR-2 clustering that resembled the clustering seen on more compliant matrices.

Figure 2.2. VEGFR-2 expression level and clustering decreases with the addition of VEGF and as a function of ECM stiffness. (A-B) Sub-confluent HUVECs seeded atop collagen-coated gels were stimulated with 5 ng/ml VEGF for the indicated times and probed for VEGFR-2 expression by Western blot (A) and normalized VEGFR-2 densitometry (B). The fold change (VEGF/control) in densitometry quantification is also reported. α-tubulin was used as a loading control. Plots are mean ± SE. N = 3 independent sets of lysates. # $p<0.05$, ### $p<0.001$ compared to control sample at each stiffness. * $p<0.05$, *** $p<0.001$. N.S. not significant. (C) Sub-confluent endothelial cells cultured on collagen-coated 1 kPa, 10 kPa, or 10 kPa gels pretreated with 5 μM Y-27632 were cultured under control conditions (upper panel) or incubated with 5 ng/ml VEGF for 15 min (lower panel) and immunostained for VEGFR-2 (green) and DAPI (blue). Insert is a 3x zoom of the boxed region. Arrows indicate VEGFR-2 clusters formed after VEGF treatment. Images were acquired with identical exposure settings (Scale bar, 20 μm). Quantification of normalized fluorescence intensity (D), average VEGFR-2 cluster size (E), and the average number of VEGFR-2 clusters per cell (F) for each condition. Plots are mean ± SE. N = 5 independent experiments, at least 30 cells per condition. * $p<0.05$, ** $p<0.01$, *** $p<0.001$ from ANOVA with post hoc Tukey's test. Panel C acquired in collaboration with Matt Zanotelli.

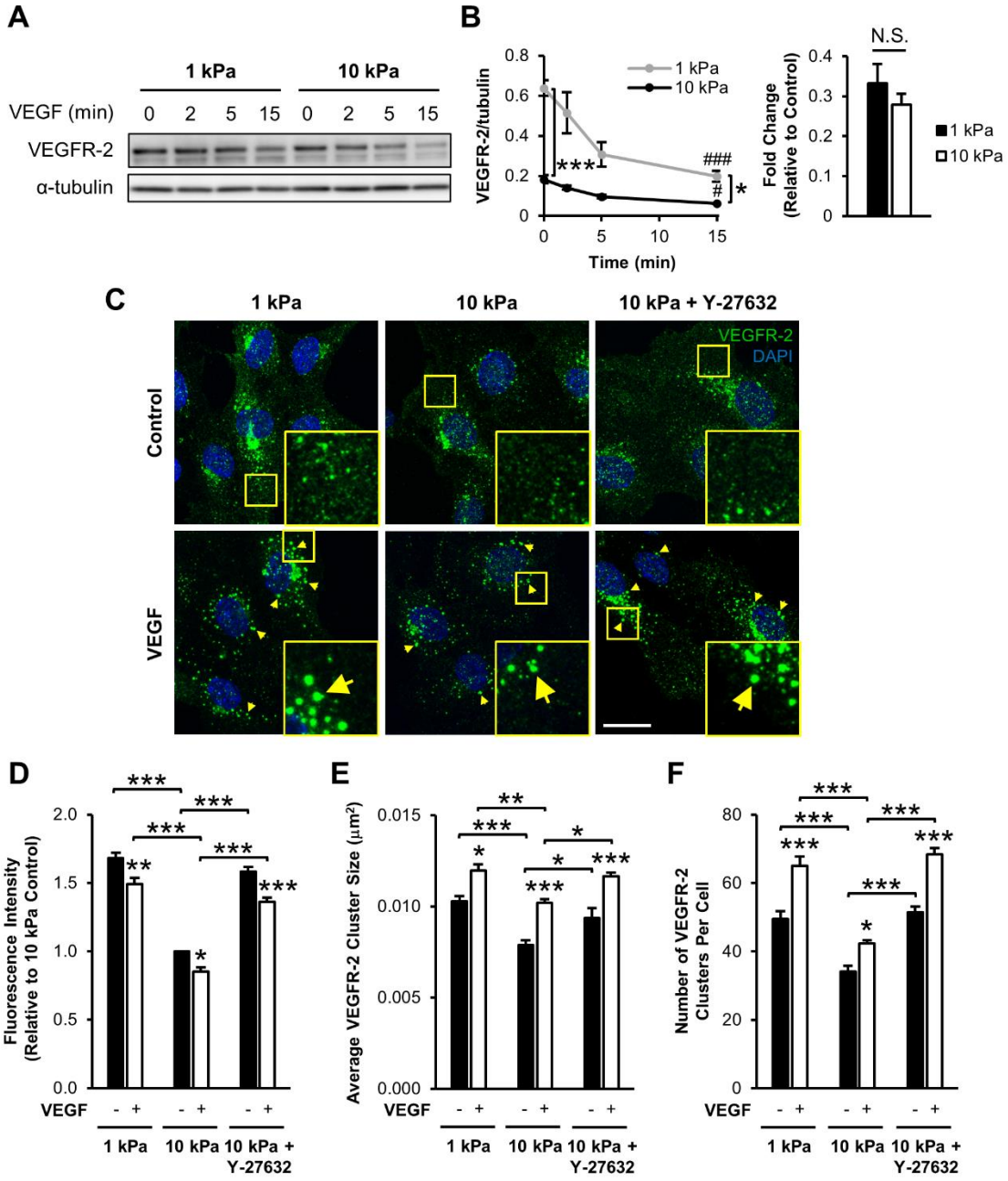
A
1 kPa
10 kPa
VEGF (min)
0 2 5 15 0 2 5 15
VEGFR-2
α-tubulin
B
VEGFR-2/tubulin
1 kPa
10 kPa
***
###
*
Time (min)
N.S.
Fold Change (Relative to Control)
1 kPa
10 kPa
C
1 kPa
10 kPa
10 kPa + Y-27632
VEGFR-2
DAPI
Control
VEGF
D
Fluorescence Intensity (Relative to 10 kPa Control)
VEGF
1 kPa
10 kPa
10 kPa + Y-27632
E
Average VEGFR-2 Cluster Size (μm²)
F
Number of VEGFR-2 Clusters Per Cell

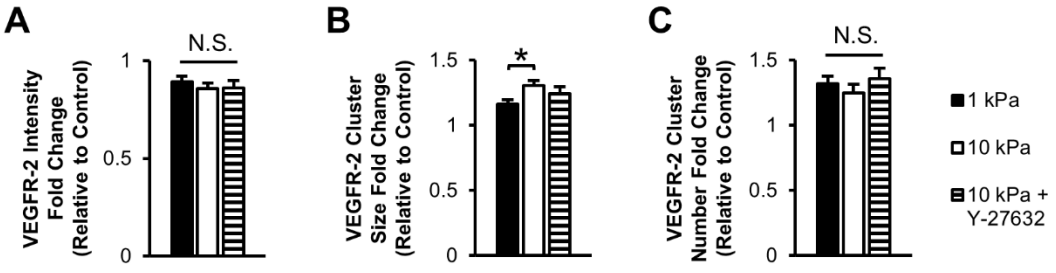

Figure 2.3. Matrix stiffness elevates VEGFR-2 clustering following VEGF stimulation. (A-C) The fold change (VEGF/control) of VEGFR-2 intensity (A), cluster size (B), and cluster number (C) following 15 min VEGF treatment for sub-confluent endothelial cells cultured on 1 kPa, 10 kPa, or 10 kPa gels with Y-27632 pretreatment. Plots are mean $\pm$ SE. N = 5 independent experiments, at least 30 cells per condition. * $p<0.05$ from ANOVA with post hoc Tukey's test. N.S. not significant.

To further investigate the role of matrix stiffness on VEGFR-2 trafficking within our system, we probed VEGFR-2 colocalization with an early endosomal marker, early endosomal antigen-1 (EEA-1) [96,99]. Sub-confluent endothelial cells cultured on compliant and stiff collagen-coated gels were stimulated with VEGF for 15 min, fixed, and immunostained for VEGFR-2 and EEA-1 (Figure 2.4A). In the absence of VEGF stimulation (control), a significant increase in VEGFR-2 colocalization with EEA-1 was observed in cells seeded on stiff matrices (Figure 2.4B), indicating increased VEGFR-2 internalization on stiff substrates. Furthermore, after stimulation with VEGF, VEGFR-2 and EEA-1 colocalization increased further (Figure 2.4B), indicating rapid VEGF-induced VEGFR-2 endocytosis. However, the fold change in VEGFR-2 and EEA-1 colocalization with VEGF treatment compared to without VEGF treatment was independent of matrix stiffness (Figure 2.5A). In addition, VEGFR-2 levels on the cell membrane were measured in non-permeabilized cells under all conditions (Figure 2.4C). As expected, decreased levels of cell surface-bound VEGFR-2 were observed as a function of ECM stiffness and VEGF treatment (Figure 2.4D), correlating with an increase in VEGFR-2 and EEA-1 colocalization (Figure 2.4B). The fold change due to VEGF stimulation was not significantly different between any conditions (Figure 2.5B), revealing no difference in VEGF responsiveness with stiffness, but that changes in receptor internalization are stiffness-mediated regardless of treatment. Since Rho/ROCK signaling affected receptor clustering (Figure 2.2), we investigated the role of Rho/ROCK signaling in VEGFR-2 internalization. Cells were cultured on 10 kPa gels and pretreated with Y-27632 before exposure to 15 min VEGF stimulation. Inhibiting ROCK reduced VEGFR-2 colocalization with EEA-1 (Figure 2.4B),

Figure 2.4. Matrix stiffness and VEGF stimulation foster VEGFR-2 colocalization with EEA-1 and decrease cell surface VEGFR-2 levels in endothelial cells. (A) Sub-confluent HUVECs on 1 kPa, 10 kPa, or 10 kPa collagen-coated gels with Y-27632 pretreatment were cultured under control conditions (left panels) or stimulated with 15 min VEGF (right panels) and then co-stained for VEGFR-2 (green), EEA-1 (red), and DAPI (blue). Insert is a 3x zoom of the boxed region. Images were acquired with identical exposure settings (Scale bar, 20 μm). (B) The average number of VEGFR-2 and EEA-1 colocalization events per cell. Plot is mean ± SE. N = 3 independent experiments, at least 30 cells per condition. (C) Non-permeabilized HUVECs were stained for VEGFR-2 (green) and DAPI (blue) following exposure to control conditions (left panel) or 15 min VEGF treatment (right panel) to visualize receptors located on the cell surface. Insert is a 3x zoom of the boxed region. Arrows indicate VEGFR-2 clusters formed after VEGF stimulation. Images were captured with identical exposure settings (Scale bar, 20 μm). (D) Quantification of the average number of membrane-bound VEGFR-2 clusters per condition. Plot is mean ± SE. N = 3 independent experiments, at least 30 cells per condition. * $p<0.05$, ** $p<0.01$, *** $p<0.001$ from ANOVA with post hoc Tukey's test. Panels A and C contributed by Matt Zanotelli.

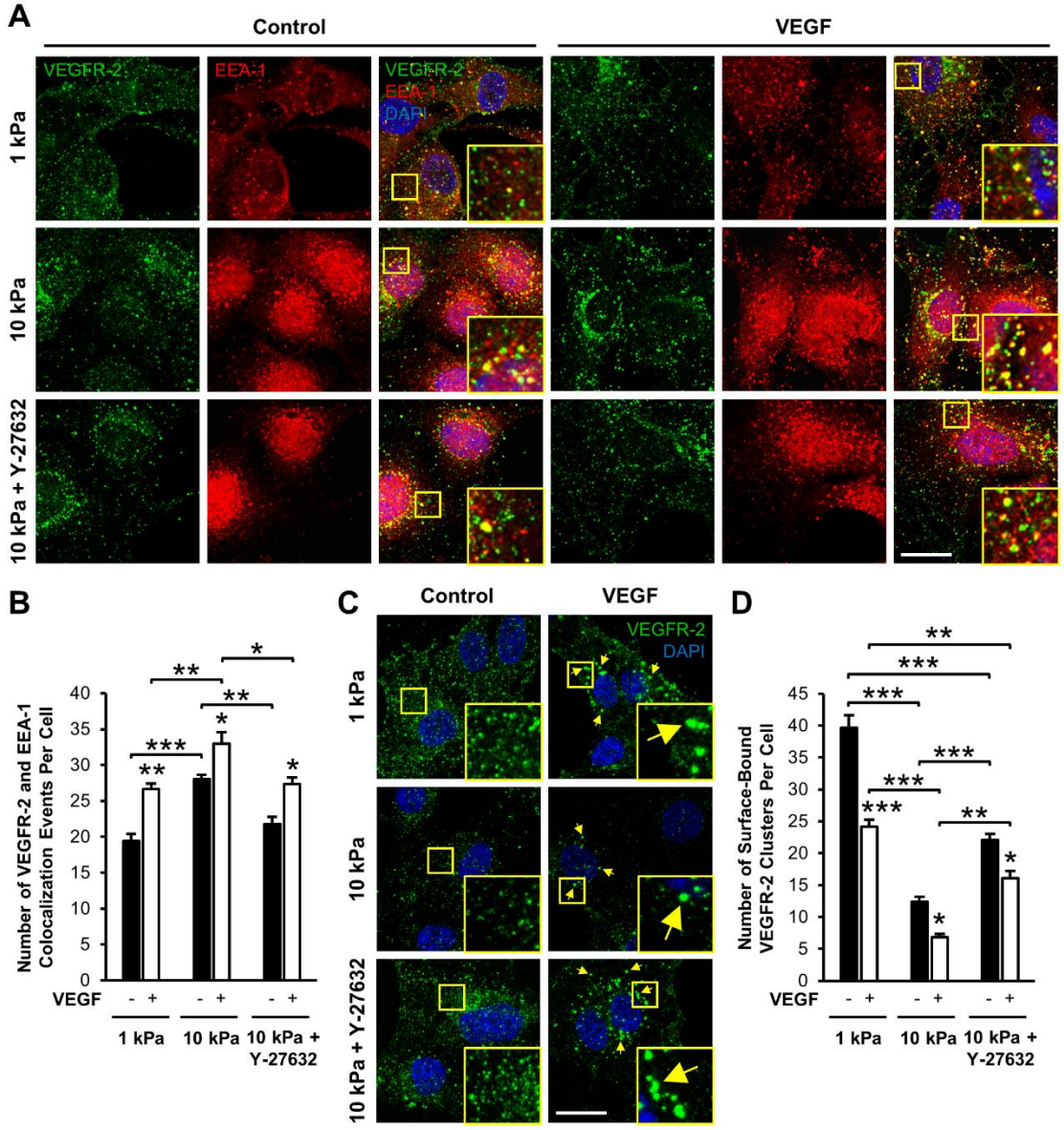
A
Control
VEGF
VEGFR-2
EEA-1
DAPI
1 kPa
10 kPa
10 kPa + Y-27632
B
Number of VEGFR-2 and EEA-1 Colocalization Events Per Cell
VEGF
1 kPa
10 kPa
10 kPa + Y-27632
C
Control
VEGF
VEGFR-2
DAPI
D
Number of Surface-Bound VEGFR-2 Clusters Per Cell

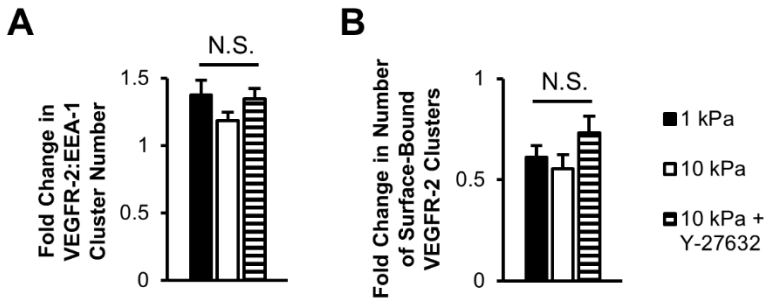

Figure 2.5. Matrix stiffness does not influence VEGF-stimulated fold change in VEGFR-2 internalization. (A) The fold change in the number of VEGFR-2 and EEA-1 colocalization events (VEGF/control) of cells cultured on 1 kPa, 10 kPa, or 10 kPa gels treated with Y-27632 following 15 min VEGF stimulation. (B) Fold change in the number of VEGFR-2 clusters on the cell surface under the same conditions. Plots are mean $\pm$ SE. N = 3 independent experiments, at least 30 cells per condition. N.S. not significant.

indicating reduced receptor internalization, and increased VEGFR-2 remaining on the cell surface. However, the levels were still significantly lower than those in cells cultured on 1 kPa gels (Figure 2.4D). Together, these data suggest a vital role of matrix mechanics in VEGFR-2 endocytosis and trafficking in endothelial cells.

It has previously been shown that VEGFR-2 is negatively regulated at cell-cell junctions to maintain contact inhibition and prevent VEGF-induced overproliferation [27,99]. Therefore, we investigated the influence of matrix stiffness on VEGFR-2 signaling in a confluent monolayer. HUVECs were seeded on 1, 5, or 10 kPa gels or glass coverslips and grown to full confluence before stimulating with 5 ng mL^{-1} VEGF. Interestingly, VEGFR-2 phosphorylation and total VEGFR-2 levels did not differ with increased matrix stiffness (Figure 2.6A-D) as seen in sub-confluent cells (Figure 2.1, 2.2), indicating that the effects of matrix stiffness on activated and total VEGFR-2 levels following VEGF stimulation are sensitive to monolayer confluence.

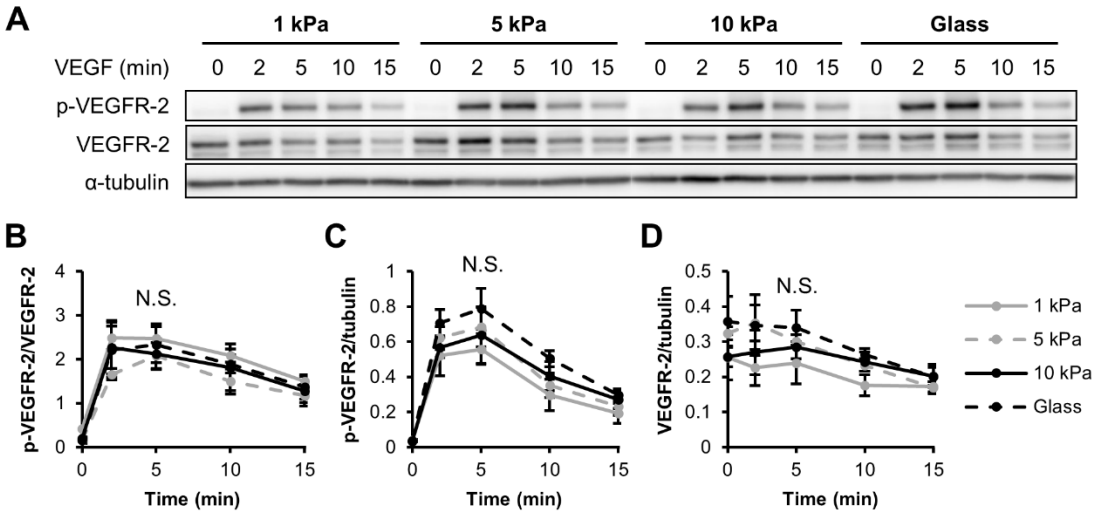

Figure 2.6. Matrix stiffness does not influence VEGF-induced VEGFR-2 phosphorylation in confluent endothelial monolayers. (A-D) Confluent HUVECs on collagen-coated PA gels or glass were stimulated with 5 ng/ml VEGF for the indicated amounts of time, lysed, and analyzed for Y1175 p-VEGFR-2 and VEGFR-2 expression using a Western blot (A) and densitometry quantifications (B-D). α-tubulin was used as a loading control. Plots are mean ± SE. N = 3 independent sets of lysates. N.S. not significant.

Matrix mechanics regulate VEGF-mediated ERK 1/2 signaling and proliferation in sub-confluent cells

Given our results indicating that matrix stiffness alters VEGFR-2 activation in sub-confluent endothelial cells, we investigated its effects on downstream signals and proliferation as a phenotypic output. ERK 1/2 is a common downstream effector molecule activated by both VEGF and matrix stiffness pathways [15,89], and VEGF promotes endothelial proliferation [23–30] in an ERK-dependent manner [15,23]. We cultured HUVECs on compliant and stiff PA gels to 50-70% confluence. When stimulated with 5 ng mL^{-1} VEGF, ERK 1/2 phosphorylation increased on stiff substrates after 5 min to a greater extent than the activation detected on compliant substrates (Figure 2.7A-C). Since ERK signaling mediates proliferation, S-phase cells were labelled and enumerated after 24 h VEGF treatment to determine whether proliferation is affected. Quantification of the percentage of proliferating (EdU positive) cells revealed that, without any exogenous VEGF added, HUVECs displayed a 2.4-fold increase in proliferation on stiffer gels compared to more compliant matrices (Figure 2.7D). In addition, proliferation increased more than two-fold on both compliant and stiff matrices following 5 ng mL^{-1} VEGF treatment (Figure 2.7D). Preincubation of cells with PD98059, an ERK 1/2 inhibitor, significantly decreased proliferation of endothelial cells cultured on both compliant and stiff substrates in a dose-dependent manner (Figure 2.7D). Similarly, a 3.5-fold increase in cell count was observed with increasing stiffness without VEGF treatment (Figure 2.7E). With VEGF stimulation cell numbers significantly increased, but PD98059 pretreatment diminished this effect (Figure 2.7E). To test if the increase observed in cell proliferation for HUVECs on 10

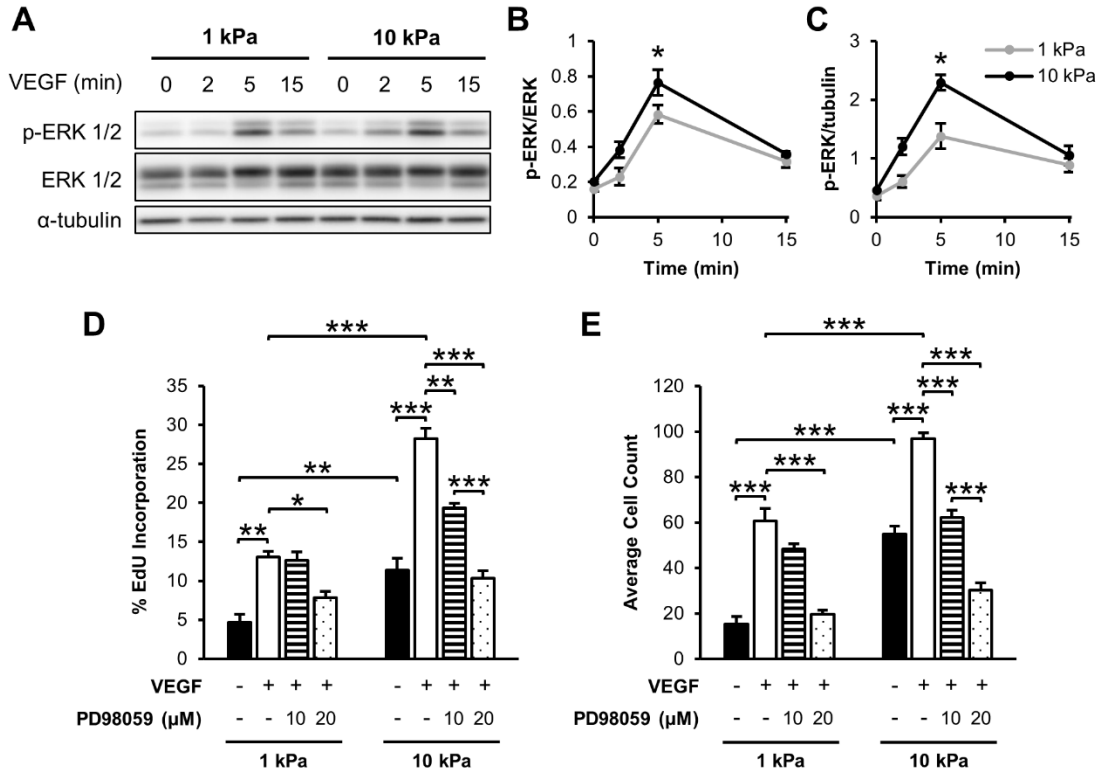

Figure 2.7. Matrix mechanics regulate VEGF-mediated ERK 1/2 phosphorylation and proliferation in sub-confluent cells. (A-C) HUVECs cultured on collagen-coated gels were analyzed following 5 ng/ml VEGF treatment for T202/Y204 ERK 1/2 phosphorylation and ERK 1/2 expression through Western blot (A) and densitometry (B-C). α-tubulin was used as a loading control. Plots are mean ± SE. N = 3 independent sets of lysates. (D) Sub-confluent HUVEC proliferation after being stimulated with 5 ng/ml VEGF for 24 h with or without PD98059 pretreatment as determined by Click-iT EdU staining. Percentages relative to total cell number. N = 3 independent experiments, at least 200 cells per condition. (E) Average cell count from 15 representative fields of view. Plots are mean ± SE. N = 3 independent experiments. * $p<0.05$, ** $p<0.01$, *** $p<0.001$ from ANOVA with post hoc Tukey's test.

kPa gels following VEGF stimulation was a result of synergism between the individual stimuli, the response was compared to the sum of the response magnitude for stiffness and VEGF separately. Our results indicate that the combined effect of increasing matrix stiffness and adding VEGF simultaneously was not greater than the sum of the responses from each individual cue (Figure 2.7D-E), suggesting a complex interaction of these pathways on endothelial proliferation rate and cell counts.

After observing differential VEGFR-2 signaling in sub-confluent compared to confluent cells (Figures 2.1, 2.6), we investigated the effect of confluency on ERK 1/2. HUVECs were seeded on 1, 5, or 10 kPa gels or glass coverslips and grown to confluence. When probed for ERK 1/2 phosphorylation and total ERK 1/2 levels in response to VEGF stimulation, we did not detect a change in ERK 1/2 signal as a function of matrix stiffness (Figure 2.8A-D), unlike the response we observed in sub-confluent cells (Figure 2.7A-C). These data suggest that the VEGF-induced response of both VEGFR-2 and ERK 1/2 is dependent upon monolayer confluency.

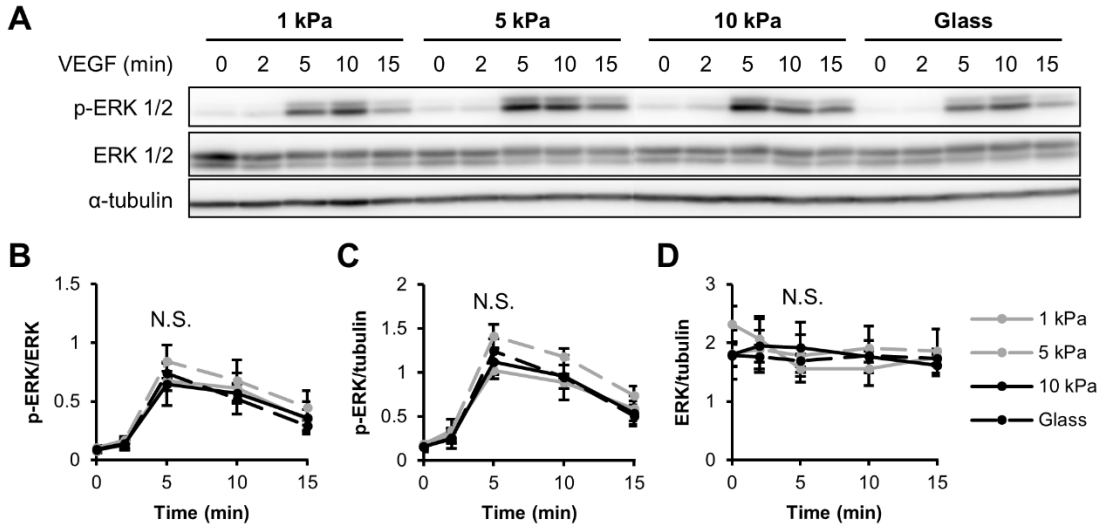

Figure 2.8. VEGF-induced ERK 1/2 phosphorylation is not influenced by ECM compliance in confluent endothelial cells. (A-D) Following 5 ng/ml VEGF stimulation for the indicated amounts of time, confluent HUVECs on various stiffness collagen-coated gels or glass were probed for T202/Y204 ERK 1/2 phosphorylation and ERK 1/2 expression using a Western blot (A) and corresponding densitometry analysis (B-D). α-tubulin was used as a loading control. Plots are mean ± SE. N = 3 independent sets of lysates. N.S. not significant.

Matrix stiffness and VEGF stimulate actin stress fiber formation in endothelial cells

VEGF has been shown to induce the formation of actin stress fibers in endothelial cells cultured on glass or plastic [100,101]. To investigate the role of matrix stiffness in VEGF-mediated stress fiber formation, sub-confluent endothelial monolayers seeded on 1 and 10 kPa gels were subjected to 5 ng mL^{-1} VEGF stimulation for 15 min, fixed, and stained for actin (Figure 2.9A). Quantification of control conditions revealed a more than three-fold increase in the number of stress fibers per cell on stiffer gels compared to more compliant substrates (Figure 2.9B), as has been previously observed [53]. Moreover, adding VEGF increased the actin intensity (Figure 2.9A) as well as increased the number of fibers more than 1.3-fold for each gel stiffness (Figure 2.9B). Together, HUVECs on stiff gels with VEGF treatment displayed over a four-fold increase in the number of stress fibers compared to cells on compliant substrates without VEGF stimulation (Figure 2.9B). While comparing the increase in stress fiber formation due to stiffness with the increase in stress fiber formation due to VEGF, our results indicate that the effects of both stiffness and VEGF were approximately additive (Figure 2.9B), suggesting a complementary, non-competitive enhancement from each signaling pathway.

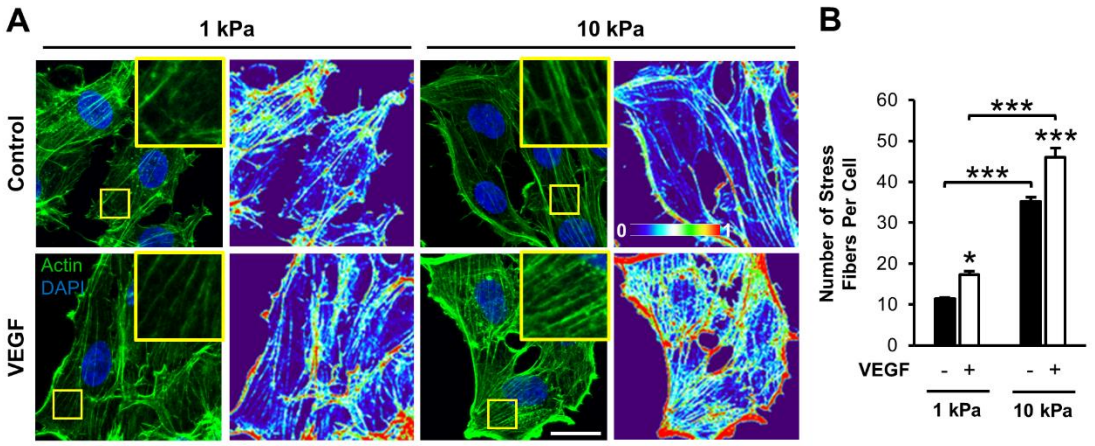

Figure 2.9. Matrix stiffness and VEGF stimulate actin stress fiber formation in endothelial cells. (A) Phalloidin (green) staining and corresponding fluorescence intensity heat maps of sub-confluent HUVECs on 1 or 10 kPa collagen-coated substrates under control conditions (upper panel) or 15 min VEGF stimulation (lower panel). Cells were counterstained with DAPI (blue). Heat maps represent low (0) to high (1) intensity (A.U.). Insert is a 3x zoom of the boxed region. Images were acquired with identical exposure settings (Scale bar, 20 μm). (B) Quantification of the average number of stress fibers per cell for each condition. Plot is mean ± SE. N = 3 independent experiments, at least 30 cells per condition. * $p<0.05$, *** $p<0.001$ from ANOVA with post hoc Tukey's test.

2.5 Discussion

Since VEGF signaling and altered matrix mechanics are both integral parts of tumor progression, specifically tumor angiogenesis, and signal through similar pathways, we sought to study their cooperative effects on endothelial cell behavior. Our data indicate that ECM stiffness increases VEGFR-2 internalization, which heightens downstream VEGF response and signaling, specifically ERK 1/2 phosphorylation, cell proliferation, and the formation of actin stress fibers, in sub-confluent endothelial cells.

Matrix stiffness is an important regulator of endothelial cell behavior [88] and more recently, matrix mechanics have also been shown to alter protein expression [74,75,82,102]. Importantly, Mammoto et al. [74] observed that increasing ECM stiffness elicits a VEGF-independent, biphasic response in VEGFR-2 levels due to stiffness-mediated regulation of VEGFR-2 transcription factors. In the present study, we also found that VEGFR-2 levels are sensitive to matrix stiffness in HUVECs, further supporting stiffness-mediated control of receptor expression. We observed different levels of VEGFR-2 phosphorylation to total VEGFR-2 with stiffness, but we would not expect complete receptor occupancy to occur with the conditions in our system [103–105]. Notably, we did not observe changes in VEGFR-2 phosphorylation levels as a function of matrix stiffness compared to the total cellular protein content. This finding suggests that ECM compliance does not influence VEGFR-2 responsiveness to VEGF stimulation. However, at increased levels of VEGF treatment where complete receptor occupancy occurs at each matrix stiffness, different response and signaling may be observed.

VEGF stimulation promotes VEGFR-2 endocytosis [95,96], and our data also indicate increased VEGFR-2 clustering and decreased total VEGFR-2 levels following VEGF treatment. This correlates with increased VEGFR-2 colocalization with EEA-1 and reduced surface-bound VEGFR-2 levels. However, no significant change in response to VEGF treatment was observed with changes in matrix stiffness. Interestingly, in the absence of exogenous stimuli, we did detect significantly increased VEGFR-2 internalization in cells cultured on stiff matrices compared to compliant substrates, as well as elevated downstream signaling, cell proliferation, and actin stress fiber formation following VEGF treatment. Together, these findings demonstrate that changes in receptor internalization are VEGF-independent but stiffness-mediated.

It is known that matrix stiffening influences cell contractility via Rho/ROCK signaling [73,106]. Elevated Rho activity is observed in endothelial cells cultured on stiff substrates compared to compliant matrices [73,77] and inhibiting ROCK with Y-27632 treatment reduces endothelial cell contractility [73]. Previously, others have probed the interactions of signaling pathways involving VEGF and Rho/ROCK and found that VEGF induces Rho activation [37,101] and its membrane recruitment [101]. Y-27632 pretreatment disrupts VEGF-induced endothelial cell migration [37,101], angiogenesis [37], and permeability [37]. Here, we show an additional role of Rho/ROCK signaling in VEGF-independent VEGFR-2 clustering and internalization. We demonstrate that increased matrix stiffness decreased VEGFR-2 intensity, cluster size, and cluster number compared to compliant matrices, suggesting more VEGFR-2 clusters are endocytosed on stiff substrates. Indeed, matrix stiffness also significantly

increased VEGFR-2 and EEA-1 colocalization, indicating elevated VEGFR-2 internalization. These results suggest that VEGFR-2 internalization is more active on stiff substrates compared to compliant matrices. Since internalization is required for many downstream VEGF signaling events including ERK 1/2 phosphorylation [15,96], increased internalization provides a possible explanation for enhanced proliferation and behavior, such as the formation of stress fibers seen on stiff substrates following VEGF treatment. Notably, Y-27632 treatment abrogated the stiffness-mediated decrease in VEGFR-2 intensity, cluster size, and cluster number initially observed in endothelial cells on stiff substrates, as well as VEGFR-2 packaging into EEA-1-positive endocytic vesicles in endothelial cells. Together, our data indicate that, even in the absence of exogenous VEGF ligand, Rho/ROCK signaling is at least partially involved in the stiffness-mediated changes in VEGFR-2 internalization and downstream signaling we observe. This suggests that increased Rho/ROCK signaling could modify or enhance the molecular interactions of VEGFR-2 with integrins or other associated intracellular signaling molecules, resulting in altered VEGF-stimulated endocytosis and downstream signaling.

However, others have observed increased VEGFR-2 internalization in bovine aortic endothelial cells cultured on compliant substrates [87]. Strikingly, this study observed reduced β1 integrin activation with increasing matrix stiffness, whereas many others report heightened integrin activation and signaling as a function of ECM stiffness [67,89,94,107], which could contribute to the differences in results. Utilizing a different gel system and endothelial cell type, our data show that HUVECs display enhanced

VEGFR-2 internalization and VEGF-stimulated downstream signaling with elevated matrix stiffness.

Matrix stiffness is known to promote Rho-mediated endothelial proliferation [53,108,109]. In agreement with other studies, we report elevated proliferation of sub-confluent endothelial cells cultured on stiff substrates compared to compliant matrices without VEGF treatment, which was reduced by inhibiting ERK 1/2. VEGF has also been shown to stimulate endothelial proliferation [23–30], primarily mediated though VEGFR-2 signaling [15]. While integrating multiple cues, our results indicate increased ERK 1/2 activation and proliferation in endothelial cells on stiff matrices following VEGF treatment. PD98059, an ERK 1/2 inhibitor, has previously been shown to inhibit VEGF-induced proliferation of HUVECs [25,29,30] and other endothelial cell types [23,26,27] cultured on glass or plastic. Further, our data demonstrate that PD98059 treatment reduced proliferation following VEGF stimulation of endothelial cells cultured on both compliant and stiff substrates. Since VEGFR-2 is internalized prior to ERK 1/2 activation [15,96], our data suggests that increased matrix stiffness promotes VEGFR-2 internalization, resulting in elevated ERK 1/2 phosphorylation and cell proliferation. Together, this suggests that aberrant Rho/ROCK signaling in the tumor microenvironment may modify the normal interaction between Rho/ROCK and ERK 1/2 pathways during healthy angiogenesis [109] to promote sustained ERK 1/2 activation [110], resulting in elevated proliferation during cancer.

Another downstream response to VEGF stimulation in endothelial cells is the formation of actin stress fibers. Cells form stress fibers when they encounter a mechanical force, and their formation is essential to cell adhesion and migration. As such, we also investigated changes in the cytoskeleton and actin stress fiber formation at different matrix stiffness to evaluate the role of matrix mechanics in VEGF-induced signaling. Previously, Yeh and colleagues [53] observed increased actin intensity in endothelial cells cultured on stiff gels compared to compliant matrices. Our data further support stiffness-enhanced fiber formation without VEGF treatment and quantify the average number of stress fibers per cell. Additionally, VEGF stimulation triggers stress fiber formation in endothelial cells within our system and others [100,101]. Since stress fiber formation also requires VEGFR-2 internalization, this suggests that cells cultured on stiffer substrates display an enhanced number of fibers due to more receptor internalization compared to compliant substrates.

Previously, others have also observed changes in intracellular signaling [111–115] and cell morphology and behavior [27,116,117] as monolayers reach confluence. Importantly, the relationship between VE-cadherin, an adherens junctional protein whose activity is highly upregulated as endothelial cells establish cell-cell contacts [118], and VEGFR-2 has been studied extensively [27,31,35,99]. In the absence of a stimulus, VE-cadherin binds VEGFR-2 to reinforce its inactive state [119] while being continuously endocytosed and recycled back to the membrane [120]. With the addition of VEGF to sub-confluent endothelial cells, VE-cadherin is phosphorylated and endocytosed to downregulate its activity, allowing VEGFR-2 activation [31,35]. Upon

reaching confluence, VE-cadherin inhibits VEGF-stimulated endothelial proliferation by associating with VEGFR-2, dramatically decreasing its internalization and signaling [27,99]. In the present study, we did not observe stiffness-enhanced signaling in confluent cells, suggesting that matrix stiffening does not overcome the negative regulation from VE-cadherin in our system.

2.6 Conclusions

The individual impacts of VEGF and matrix stiffness on endothelial behavior have been previously investigated, however their concerted efforts are less well understood. Here, we show enhanced VEGFR-2 endocytosis and downstream VEGF-induced ERK 1/2 signaling, cell proliferation, and formation of stress fibers in endothelial cells cultured on stiffer substrates. This work helps to provide a possible mechanism to explain several observations about stiffness-mediated activation of growth factor receptors. Importantly, identifying mechanistic crosstalk and subsequent behavioral effects may aid in developing therapeutics to combat their dysregulation during diseases such as cancer.

2.7 Acknowledgments

This work was supported by grants from the National Institute of Health (R01HL127499) to C.A.R.-K., a scholarship for the Next Generation of Scientist from the Cancer Society to F.B., and the National Science Foundation Graduate Research Fellowship Program to D.J.L. and M.R.Z.

REFERENCES

1. Carmeliet P, Jain RK. Angiogenesis in cancer and other diseases. Nature. 2000;407:249–57.
2. Papetti M, Herman IM. Mechanisms of normal and tumor-derived angiogenesis. Am J Cell Physiol. 2002;282:C947–70.
3. Carmeliet P, Jain RK. Molecular mechanisms and clinical applications of angiogenesis. Nature. 2011;473:298–307.
4. Fukumura D, Jain RK. Tumor microenvironment abnormalities: causes, consequences, and strategies to normalize. J Cell Biochem. 2007;101:937–49.
5. Chauhan VP, Stylianopoulos T, Boucher Y, Jain RK. Delivery of molecular and nanoscale medicine to tumors: transport barriers and strategies. Annu Rev Chem Biomol Eng. 2011;2:281–98.
6. Munn LL. Aberrant vascular architecture in tumors and its importance in drug-based therapies. Drug Discov Today. 2003 May 1;8(9):396–403.
7. Ebos JML, Lee CR, Cruz-Munoz W, Bjarnason GA, Christensen JG, Kerbel RS. Accelerated Metastasis after Short-Term Treatment with a Potent Inhibitor of Tumor Angiogenesis. Cancer Cell. 2009;15(3):232–9.
8. Pàez-Ribes M, Allen E, Hudock J, Takeda T, Okuyama H, Viñals F, Inoue M, Bergers G, Hanahan D, Casanovas O. Antiangiogenic Therapy Elicits Malignant Progression of Tumors to Increased Local Invasion and Distant Metastasis. Cancer Cell. 2009;15(3):220–31.
9. Gilkes DM, Semenza GL, Wirtz D. Hypoxia and the extracellular matrix: drivers of tumour metastasis. Nat Rev Cancer. 2014 Jun;14(6):430–9.

10. Bergers G, Hanahan D. Modes of resistance to anti-angiogenic therapy. Nat Rev Cancer. 2008;8:592–603.
11. Ferrara N. Pathways mediating VEGF-independent tumor angiogenesis. Cytokine Growth Factor Rev. 2010;21(1):21–6.
12. Jain RK. Normalizing tumor vasculature with anti-angiogenic therapy: A new paradigm for combination therapy. Nat Med. 2001;7(9):987–9.
13. Jain RK. Normalization of tumor vasculature: an emerging concept in antiangiogenic therapy. Science. 2005;307:58–62.
14. Carmeliet P, Jain RK. Principles and mechanisms of vessel normalization for cancer and other angiogenic diseases. Nat Rev Drug Discov. 2011 Jun;10(6):417–27.
15. Holmes K, Roberts OL, Thomas AM, Cross MJ. Vascular endothelial growth factor receptor-2: structure, function, intracellular signalling and therapeutic inhibition. Cell Signal. 2007;19:2003–12.
16. Hanjaya-Putra D, Yee J, Ceci D, Truitt R, Yee D, Gerecht S. Vascular endothelial growth factor and substrate mechanics regulate in vitro tubulogenesis of endothelial progenitor cells. J Cell Mol Med. 2010;14(10):2436–47.
17. Shamloo A, Heilshorn SC. Matrix density mediates polarization and lumen formation of endothelial sprouts in VEGF gradients. Lab Chip. 2010;10:3061–8.
18. Wu Y, Al-Ameen MA, Ghosh G. Integrated effects of matrix mechanics and vascular endothelial growth factor (VEGF) on capillary sprouting. Ann Biomed

Eng. 2014;42(5):1024–36.

19. Saunders RL, Hammer DA. Assembly of human umbilical vein endothelial cells on compliant hydrogels. Cell Mol Bioeng. 2010;3(1):60–7.

20. Morales-Ruiz M, Fulton D, Sowa G, Languino LR, Fujio Y, Walsh K, Sessa WC. Vascular Endothelial Growth Factor – Stimulated Actin Reorganization and Migration of Endothelial Cells Is Regulated via the Serine/Threonine Kinase Akt. Circ Res. 2000;86:892–6.

21. Abu-Ghazaleh R, Kabir J, Jia H, Lobo M, Zachary I. Src mediates stimulation by vascular endothelial growth factor of the phosphorylation of focal adhesion kinase at tyrosine 861, and migration and anti-apoptosis in endothelial cells. Biochem J. 2001;360:255–64.

22. Hutchings H, Ortega N, Plouet J. Extracellular matrix-bound vascular endothelial growth factor promotes endothelial cell adhesion, migration, and survival through integrin ligation. FASEB J. 2003;17:1520–2.

23. Pedram A, Razandi M, Levin ER. Extracellular signal-regulated protein kinase/jun kinase cross-talk underlies vascular endothelial cell growth factor-induced endothelial cell proliferation. J Biol Chem. 1998;273(41):26722–8.

24. Soker S, Gollamudi-Payne S, Fidder H, Charmahelli H, Klagsbrun M. Inhibition of vascular endothelial growth factor (VEGF) induced endothelial cell proliferation by a peptide corresponding to the exon-7 encoded domain of VEGF165. J Biol Chem. 1997;272(50):31582–8.

25. Zeng H, Dvorak HF, Mukhopadhyay D. Vascular permeability factor (VPF)/vascular endothelial growth factor (VEGF) receptor-1 down-modulates

VPF/VEGF receptor-2-mediated endothelial cell proliferation, but not migration, through phosphatidylinositol 3-kinase-dependent pathways. J Biol Chem. 2001;276(29):26969–79.

26. Kroll J, Waltenberger J. The vascular endothelial growth factor receptor KDR activates multiple signal transduction pathways in porcine aortic endothelial cells. J Biol Chem. 1997;272(51):32521–7.

27. Lampugnani MG, Zanetti A, Corada M, Takahashi T, Balconi G, Breviario F, Orsenigo F, Cattelino A, Kemler R, Daniel TO, Dejana E. Contact inhibition of VEGF-induced proliferation requires vascular endothelial cadherin, B-catenin, and the phosphatase DEP-1/CD148. J Cell Biol. 2003;161(4):793–804.

28. Yoshida A, Anand-apte B, Zetter BR. Differential endothelial migration and proliferation to basic fibroblast growth factor and vascular endothelial growth factor. Growth factors. 1996;13:57–64.

29. Kanno S, Oda N, Abe M, Terai Y, Ito M, Shitara K, Tabayashi K, Shibuya M, Sato Y. Roles of two VEGF receptors, Flt-1 and KDR, in the signal transduction of VEGF effects in human vascular endothelial cells. Oncogene. 2000;19:2138–46.

30. Ali N, Yoshizumi M, Fujita Y, Izawa Y, Kanematsu Y, Ishizawa K, Tsuchiya K, Yano S, Sone S, Tamaki T. A novel src kinase inhibitor, M475271, inhibits VEGF-induced human umbilical vein endothelial cell proliferation and migration. J Pharmacol Sci. 2005;98:130–41.

31. Esser S, Lampugnani MG, Corada M, Dejana E, Risau W. Vascular endothelial growth factor induces VE-cadherin tyrosine phosphorylation in endothelial

cells. J Cell Sci. 1998;111:1853–65.

32. Eliceiri BP, Paul R, Schwartzberg PL, Hood JD, Leng J, Cheresh DA. Selective requirement for Src kinases during VEGF-induced angiogenesis and vascular permeability. Mol Cell. 1999;4:915–24.

33. Breslin JW, Pappas PJ, Cerveira JJ, Hobson RW, Durán WN. VEGF increases endothelial permeability by separate signaling pathways involving ERK-1/2 and nitric oxide. Am J Physiol Hear Circ Physiol. 2003 Jan;284:H92–100.

34. Behzadian MA, Windsor LJ, Ghaly N, Liou G, Tsai NT, Caldwell RB. VEGF-induced paracellular permeability in cultured endothelial cells involves urokinase and its receptor. FASEB J. 2003;17:752–4.

35. Gavard J, Gutkind JS. VEGF controls endothelial-cell permeability by promoting the beta-arrestin-dependent endocytosis of VE-cadherin. Nat Cell Biol. 2006;8(11):1223–34.

36. Harhaj NS, Felinski EA, Wolpert EB, Sundstrom JM, Gardner TW, Antonetti DA. VEGF activation of protein kinase C stimulates occludin phosphorylation and contributes to endothelial permeability. Investig Ophthalmol Vis Sci. 2006;47:5106–15.

37. Bryan BA, Dennstedt E, Mitchell DC, Walshe TE, Noma K, Loureiro R, Saint-Geniez M, Campaigniac J-P, Liao JK, D'Amore PA. RhoA/ROCK signaling is essential for multiple aspects of VEGF-mediated angiogenesis. FASEB J. 2010;24:3186–95.

38. Senger DR, Galli SJ, Dvorak AM, Perruzzi CA, Harvey VS, Dvorak HF. Tumor cells secrete a vascular permeability factor that promotes accumulation

of ascites fluid. Science. 1983;219(4587):983–5.

39. Senger DR, Perruzzi CA, Feder J, Dvorak HF. A Highly Conserved Vascular Permeability Factor Secreted by a Variety of Human and Rodent Tumor Cell Lines. Cancer Res. 1986;46:5629–32.

40. Fukumura D, Xavier R, Sugiura T, Chen Y, Park EC, Lu N, Selig M, Nielsen G, Taksir T, Jain RK, Seed B. Tumor induction of VEGF promoter activity in stromal cells. Cell. 1998;94:715–25.

41. Takahashi Y, Kitadai Y, Bucana CD, Cleary KR, Ellis LM. Expression of vascular endothelial growth factor and its receptor, KDR, correlates with vascularity, metastasis, and proliferation of human colon cancer. Cancer Res. 1995;55:3964–8.

42. Ferrara N, Davis-Smyth T. The biology of vascular endothelial growth factor. Endocr Rev. 1997;18(1):4–25.

43. Ferrara N, Hillan KJ, Gerber H-P, Novotny W. Discovery and development of bevacizumab, an anti-VEGF antibody for treating cancer. Nat Rev Drug Discov. 2004;3:391–400.

44. Batchelor TT, Sorensen AG, di Tomaso E, Zhang W-T, Duda DG, Cohen KS, Kozak KR, Cahill DP, Chen P-J, Zhu M, Ancukiewicz M, Mrugala MM, Plotkin S, Drappatz J, Louis DN, Ivy P, Scadden DT, Benner T, Loeffler JS, Wen PY, Jain RK. AZD2171, a Pan-VEGF Receptor Tyrosine Kinase Inhibitor, Normalizes Tumor Vasculature and Alleviates Edema in Glioblastoma Patients. Cancer Cell. 2007;11(1):83–95.

45. Mendel DB, Laird AD, Xin X, Louie SG, Christensen JG, Li G, Schreck RE,

Abrams TJ, Ngai TJ, Lee LB, Murray LJ, Carver J, Chan E, Moss KG, Joshua O, Sukbuntherng J, Blake RA, Sun L, Tang C, Miller T, Shirazian S, Mcmahon G, Cherrington JM. In Vivo Antitumor Activity of SU11248, a Novel Tyrosine Kinase Inhibitor Targeting Vascular Endothelial Growth Factor and Platelet-derived Growth Factor Receptors: Determination of a Pharmacokinetic/Pharmacodynamic Relationship. Clin Cancer Res. 2003;9:327–37.

46. Jayson GC, Kerbel R, Ellis LM, Harris AL. Antiangiogenic therapy in oncology: current status and future directions. Lancet. 2016;388:518–29.

47. Dickinson LE, Rand DR, Tsao J, Eberle W, Gerecht S. Endothelial cell responses to micropillar substrates of varying dimensions and stiffness. J Biomed Mater Res A. 2012 Jun;100(6):1457–66.

48. Lu P, Takai K, Weaver VM, Werb Z. Extracellular matrix degradation and remodeling in development and disease. Cold Spring Harb Perspect Biol. 2011 Dec;3:a005058.

49. Discher DE, Janmey P, Wang Y-L. Tissue cells feel and respond to the stiffness of their substrate. Science. 2005;310:1139–43.

50. Califano JP, Reinhart-King CA. A balance of substrate mechanics and matrix chemistry regulates endothelial cell network assembly. Cell Mol Bioeng. 2008;1(2–3):122–32.

51. Sun J, Jamilpour N, Wang F-Y, Wong PK. Geometric control of capillary architecture via cell-matrix mechanical interactions. Biomaterials. 2014 Mar;35(10):3273–80.

52. Reinhart-King CA, Dembo M, Hammer DA. Cell-cell Mechanical Communication through Compliant Substrates. Biophys J. 2008 Dec 15;95(12):6044–51.

53. Yeh Y-T, Hur SS, Chang J, Wang K-C, Chiu J-J, Li Y-S, Chien S. Matrix stiffness regulates endothelial cell proliferation through septin 9. PLoS One. 2012;7(10):e46889.

54. Ghajar CM, Chen X, Harris JW, Suresh V, Hughes CCW, Jeon NL, Putnam AJ, George SC. The effect of matrix density on the regulation of 3-D capillary morphogenesis. Biophys J. 2008 Mar 1;94:1930–41.

55. Edgar LT, Underwood CJ, Guilkey JE, Hoying JB, Weiss JA. Extracellular matrix density regulates the rate of neovessel growth and branching in sprouting angiogenesis. PLoS One. 2014 Jan;9(1):e85178.

56. Yamamura N, Sudo R, Ikeda M, Tanishita K. Effects of the mechanical properties of collagen gel on the in vitro formation of microvessel networks by endothelial cells. Tissue Eng. 2007 Jul;13(7):1443–53.

57. Mason BN, Starchenko A, Williams RM, Bonassar LJ, Reinhart-King CA. Tuning three-dimensional collagen matrix stiffness independently of collagen concentration modulates endothelial cell behavior. Acta Biomater. 2013;9:4635–44.

58. Bordeleau F, Mason BN, Lollis EM, Mazzola MC, Zanotelli MR, Somasegar S, Califano JP, Montague CR, LaValley DJ, Huynh J, Negrón Abril YL, Bonassar LJ, Butcher JT, Weiss RS, Reinhart-King CA. Matrix stiffening promotes a tumor vasculature phenotype. Proc Natl Acad Sci. 2016;114(3):492–7.

59. Francis-Sedlak ME, Moya ML, Huang J-J, Lucas S a, Chandrasekharan N, Larson JC, Cheng M-H, Brey EM. Collagen glycation alters neovascularization in vitro and in vivo. Microvasc Res. 2010 Jul;80(1):3–9.

60. Sieminski AL, Hebbel RP, Gooch KJ. The relative magnitudes of endothelial force generation and matrix stiffness modulate capillary morphogenesis in vitro. Exp Cell Res. 2004 Jul 15;297:574–84.

61. Kniazeva E, Putnam AJ. Endothelial cell traction and ECM density influence both capillary morphogenesis and maintenance in 3-D. Am J Physiol - Cell Physiol. 2009;297:179–87.

62. Chung AWY, Yang HHC, Sigrist MK, Brin G, Chum E, Gourlay W a, Levin A. Matrix metalloproteinase-2 and -9 exacerbate arterial stiffening and angiogenesis in diabetes and chronic kidney disease. Cardiovasc Res. 2009 Dec 1;84(3):494–504.

63. Charest JM, Califano JP, Carey SP, Reinhart-King CA. Fabrication of substrates with defined mechanical properties and topographical features for the study of cell migration. Macromol Biosci. 2012 Jan;12:12–20.

64. Bauer AL, Jackson TL, Jiang Y. Topography of extracellular matrix mediates vascular morphogenesis and migration speeds in angiogenesis. PLoS Comput Biol. 2009 Jul;5(7):e1000445.

65. van Oers RFM, Rens EG, LaValley DJ, Reinhart-King CA, Merks RMH. Mechanical cell-matrix feedback explains pairwise and collective endothelial cell behavior in vitro. PLoS Comput Biol. 2014;10(8):e1003774.

66. Bauer AL, Jackson TL, Jiang Y. A cell-based model exhibiting branching and

anastomosis during tumor-induced angiogenesis. Biophys J. 2007 May 1;92(9):3105–21.

67. Levental KR, Yu H, Kass L, Lakins JN, Egeblad M, Erler JT, Fong SFT, Csiszar K, Giaccia A, Weninger W, Yamauchi M, Gasser DL, Weaver VM. Matrix crosslinking forces tumor progression by enhancing integrin signaling. Cell. 2009;139:891–906.

68. Lopez JI, Kang I, You W-K, McDonald DM, Weaver VM. In situ force mapping of mammary gland transformation. Integr Biol. 2011;3:910–21.

69. Shen Y-I, Abaci HE, Krupski Y, Weng L-C, Burdick JA, Gerecht S. Hyaluronic acid hydrogel stiffness and oxygen tension affect cancer cell fate and endothelial sprouting. Biomater Sci. 2014;2:655–65.

70. Ghosh K, Thodeti CK, Dudley AC, Mammoto A, Klagsbrun M, Ingber DE. Tumor-derived endothelial cells exhibit aberrant Rho-mediated mechanosensing and abnormal angiogenesis in vitro. Proc Natl Acad Sci. 2008 Aug 12;105(32):11305–10.

71. Liang Y, Jeong J, DeVolder RJ, Cha C, Wang F, Tong YW, Kong H. A cell-instructive hydrogel to regulate malignancy of 3D tumor spheroids with matrix rigidity. Biomaterials. 2011 Dec;32(35):9308–15.

72. Krishnan R, Klumpers DD, Park CY, Rajendran K, Trepat X, Bezu J Van, Hinsbergh VWM Van, Carman C V, Brain JD, Fredberg JJ, Butler JP, Van Nieuw Amerongen GP. Substrate stiffening promotes endothelial monolayer disruption through enhanced physical forces. Am J Physiol Cell Physiol. 2011;300:146–54.

73. Huynh J, Nishimura N, Rana K, Peloquin JM, Califano JP, Montague CR, King MR, Schaffer CB, Reinhart-King CA. Age-related intimal stiffening enhances endothelial permeability and leukocyte transmigration. Sci Transl Med. 2011;3(112):112ra122.

74. Mammoto A, Connor KM, Mammoto T, Yung CW, Huh D, Aderman CM, Mostoslavsky G, Smith LEH, Ingber DE. A mechanosensitive transcriptional mechanism that controls angiogenesis. Nature. 2009;457:1103–8.

75. Bordeleau F, Califano JP, Abril YLN, Mason BN, LaValley DJ, Shin SJ, Weiss RS, Reinhart-King CA. Tissue stiffness regulates serine/arginine-rich protein-mediated splicing of the extra domain B-fibronectin isoform in tumors. Proc Natl Acad Sci. 2015;112(27):8314–9.

76. Deroanne CF, Lapiere CM, Nusgens B V. In vitro tubulogenesis of endothelial cells by relaxation of the coupling extracellular matrix-cytoskeleton. Cardiovasc Res. 2001;49:647–58.

77. Lampi MC, Faber CJ, Huynh J, Bordeleau F, Zanotelli MR, Reinhart-King CA. Simvastatin ameliorates matrix stiffness-mediated endothelial monolayer disruption. PLoS One. 2016;11(1):e0147033.

78. Urbano RL, Furia C, Basehore S, Clyne AM. Stiff Substrates Increase Inflammation-Induced Endothelial Monolayer Tension and Permeability. Biophys J. 2017;113(3):645–55.

79. Mammoto A, Mammoto T, Kanapathipillai M, Wing Yung C, Jiang E, Jiang A, Lofgren K, Gee EPS, Ingber DE. Control of lung vascular permeability and endotoxin-induced pulmonary oedema by changes in extracellular matrix

mechanics. Nat Commun. 2013;4:1759.

80. Ingber DE. Mechanical signaling and the cellular response to extracellular matrix in angiogenesis and cardiovascular physiology. Circ Res. 2002;91:877–87.

81. Paszek MJ, Zahir N, Johnson KR, Lakins JN, Rozenberg GI, Gefen A, Reinhart-King CA, Margulies SS, Dembo M, Boettiger D, Hammer DA, Weaver VM. Tensional homeostasis and the malignant phenotype. Cancer Cell. 2005;8:241–54.

82. Leight JL, Wozniak MA, Chen S, Lynch ML, Chen CS. Matrix rigidity regulates a switch between TGF-B1-induced apoptosis and epithelial-mesenchymal transition. Mol Biol Cell. 2012;23:781–91.

83. Kim J-H, Asthagiri AR. Matrix stiffening sensitizes epithelial cells to EGF and enables the loss of contact inhibition of proliferation. J Cell Sci. 2011;124:1280–7.

84. Brown XQ, Bartolak-Suki E, Williams C, Walker ML, Weaver VM, Wong JY. Effect of substrate stiffness and PDGF on the behavior of vascular smooth muscle cells: implications for atherosclerosis. J Cell Physiol. 2010;225:115–22.

85. Huynh J, Bordeleau F, Kraning-Rush CM, Reinhart-King CA. Substrate stiffness regulates PDGF-induced circular dorsal ruffle formation through MLCK. Cell Mol Bioeng. 2013;6(2):138–47.

86. Wingate K, Floren M, Tan Y, Tseng PON, Tan W. Synergism of matrix stiffness and vascular endothelial growth factor on mesenchymal stem cells for vascular endothelial regeneration. Tissue Eng Part A. 2014;20(17–18):2503–12.

87. Sack KD, Teran M, Nugent MA. Extracellular matrix stiffness controls VEGF signaling and processing in endothelial cells. J Cell Physiol. 2016;231(9):2026–39.

88. LaValley DJ, Reinhart-King CA. Matrix stiffening in the formation of blood vessels. Adv Regen Biol. 2014;1(1):25247.

89. Huveneers S, Danen EHJ. Adhesion signaling - crosstalk between integrins, Src and Rho. J Cell Sci. 2009;122:1059–69.

90. Reinhart-King CA, Dembo M, Hammer DA. Endothelial cell traction forces on RGD-derivatized polyacrylamide substrata. Langmuir. 2003;19:1573–9.

91. Peloquin J, Huynh J, Williams RM, Reinhart-King CA. Indentation measurements of the subendothelial matrix in bovine carotid arteries. J Biomech. 2011;44:815–21.

92. Gallagher SR. Electrophoresis and Immunoblotting. In: Bonifacino JS, Harford JB, Lippincott-Swartz J, Yamada KM, editors. Current Protocols in Cell Biology. 37th ed. Bethesda, MD: John Wiley and Sons, Inc.; 2007. p. 6.1.1-6.1.38.

93. Bordeleau F, Lapierre M-EM, Sheng Y, Marceau N. Keratin 8/18 regulation of cell stiffness-extracellular matrix interplay through modulation of Rho-mediated actin cytoskeleton dynamics. PLoS One. 2012;6(7):e38780.

94. Butcher DT, Alliston T, Weaver VM. A tense situation: forcing tumour progression. Nat Rev Cancer. 2009;9:108–22.

95. Nakayama M, Nakayama A, van Lessen M, Yamamoto H, Hoffmann S, Drexler HCA, Itoh N, Hirose T, Breier G, Vestweber D, Cooper JA, Ohno S,

Kaibuchi K, Adams RH. Spatial regulation of VEGF receptor endocytosis in angiogenesis. Nat Cell Biol. 2013;15(3):249–60.

96. Simons M. An Inside View: VEGF Receptor Trafficking and Signaling. Physiol Rev. 2012;27:213–22.

97. Du J, Chen X, Liang X, Zhang G, Xu J, He L, Zhan Q, Feng X-Q, Chien S, Yang C. Integrin activation and internalization on soft ECM as a mechanism of induction of stem cell differentiation by ECM elasticity. Proc Natl Acad Sci. 2011;108(23):9466–71.

98. Ishizaki T, Uehata M, Tamechika I, Keel J, Nonomura K, Maekawa M, Narumiya S. Pharmacological properties of Y-27632, a specific inhibitor of Rho-associated kinases. Mol Pharmacol. 2000;57:976–83.

99. Lampugnani MG, Orsenigo F, Gagliani MC, Tacchetti C, Dejana E. Vascular endothelial cadherin controls VEGFR-2 internalization and signaling from intracellular compartments. J Cell Biol. 2006;174(4):593–604.

100. Rousseau S, Houle F, Kotanides H, Witte L, Waltenberger J, Landry J, Huot J. Vascular endothelial growth factor (VEGF)-driven actin-based motility is mediated by VEGFR2 and requires concerted activation of stress-activated protein kinase 2 (SAPK2/p38) and geldanamycin-sensitive phosphorylation of focal adhesion kinase. J Biol Chem. 2000;275(14):10661–72.

101. van Nieuw Amerongen GP, Koolwijk P, Versteilen A, van Hinsbergh VW. Involvement of RhoA/Rho kinase signaling in VEGF-induced endothelial cell migration and angiogenesis in vitro. Arterioscler Thromb Vasc Biol. 2003;23:211–7.

102. Mouw JK, Yui Y, Damiano L, Bainer RO, Lakins JN, Acerbi I, Ou G, Wijekoon AC, Levental KR, Gilbert PM, Hwang ES, Chen Y-Y, Weaver VM. Tissue mechanics modulate microRNA-dependent PTEN expression to regulate malignant progression. Nat Med. 2014;20(4):360–7.

103. Mac Gabhann F, Popel AS. Model of competitive binding of vascular endothelial growth factor and placental growth factor to VEGF receptors on endothelial cells. Am J Physiol Circ Physiol. 2004;286(1):H153–64.

104. Mac Gabhann F, Yang MT, Popel AS. Monte Carlo simulations of VEGF binding to cell surface receptors in vitro. Biochim Biophys Acta. 2005;1746(2):95–107.

105. Bentley K, Gerhardt H, Bates PA. Agent-based simulation of notch-mediated tip cell selection in angiogenic sprout initialisation. J Theor Biol. 2008;250(1):25–36.

106. Wang H-B, Dembo M, Wang Y-L. Substrate flexibility regulates growth and apoptosis of normal but not transformed cells. Am J Physiol Cell Physiol. 2000;279:C1345–50.

107. Delcommenne M, Streulis CH. Control of Integrin Expression by Extracellular Matrix. J Biol Chem. 1995;270(45):26794–801.

108. Provenzano PP, Keely PJ. Mechanical signaling through the cytoskeleton regulates cell proliferation by coordinated focal adhesion and Rho GTPase signaling. J Cell Sci. 2011;124:1195–205.

109. Mavria G, Vercoulen Y, Yeo M, Paterson H, Karasarides M, Marais R, Bird D, Marshall CJ. ERK-MAPK signaling opposes Rho-kinase to promote endothelial

cell survival and sprouting during angiogenesis. Cancer Cell. 2006;9:33–44.

110. Welsh CF, Roovers K, Villanueva J, Liu Y, Schwartz MA, Assoian RK. Timing of cyclin D1 expression within G1 phase is controlled by Rho. Nat Cell Biol. 2001;3:950–7.

111. Lampugnani MG, Corada M, Andriopoulou P, Esser S, Risau W, Dejana E. Cell confluence regulates tyrosine phosphorylation of adherens junction components in endothelial cells. J Cell Sci. 1997;110:2065–77.

112. Corvera S, DiBonaventura C, Shpetner HS. Cell confluence-dependent remodeling of endothelial membranes mediated by cholesterol. J Biol Chem. 2000;275(40):31414–21.

113. Jiang H, Weyrich AS, Zimmerman GA, McIntyre TM. Endothelial cell confluence regulates cyclooxygenase-2 and prostaglandin E2 production that modulate motility. J Biol Chem. 2004;279(53):55905–13.

114. Faust D, Dolado I, Cuadrado A, Oesch F, Weiss C, Nebreda AR, Dietrich C. p38alpha MAPK is required for contact inhibition. Oncogene. 2005;24:7941–5.

115. Curto M, Cole BK, Lallemand D, Liu CH, McClatchey AI. Contact-dependent inhibition of EGFR signaling by Nf2/Merlin. J Cell Biol. 2007;177(5):893–903.

116. Puliafito A, Hufnagel L, Neveu P, Streichan S, Sigal A, Fygenson DK, Shraiman BI. Collective and single cell behavior in epithelial contact inhibition. Proc Natl Acad Sci. 2012;109(3):739–44.

117. Ishibe S, Haydu JE, Togawa A, Marlier A, Cantley LG. Cell confluence regulates hepatocyte growth factor-stimulated cell morphogenesis in a B-catenin-dependent manner. Mol Cell Biol. 2006;26(24):9232–43.

118. Vestweber D. VE-cadherin: the major endothelial adhesion molecule controlling cellular junctions and blood vessel formation. Arterioscler Thromb Vasc Biol. 2008;28:223–32.

119. Simons M, Gordon E, Claesson-Welsh L. Mechanisms and regulation of endothelial VEGF receptor signalling. Nat Rev Mol Cell Biol. 2016;17:611–25.

120. Gampel A, Moss L, Jones MC, Brunton V, Norman JC, Mellor H. VEGF regulates the mobilization of VEGFR2/KDR from an intracellular endothelial storage compartment. Blood. 2006;108(8):2624-31.

CHAPTER 3

PUMPLESS, UNIDIRECTIONAL MICROPHYSIOLOGICAL SYSTEM FOR TESTING METABOLISM-DEPENDENT CHEMOTHERAPEUTIC TOXICITY

This chapter is in preparation for *Lab on a Chip* [1]

3.1 Abstract

Drug development is often hindered by the failure of preclinical models to accurately assess and predict the efficacy and safety of drug candidates. Therefore, body-on-a-chip microfluidic devices, also called micro cell culture analogs (μCCAs), are being created to better predict human responses to drugs. Each μCCA is designed with separate organ chambers interconnected with microfluidic channels mimicking blood circulation. Here, we propose the first pumpless, unidirectional, multiorgan system to aid in anti-cancer drug testing. HCT-116 colon cancer spheroids, HepG2/C3A hepatocytes, and HL-60 promyeloblasts were embedded in collagen hydrogels and cultured within compartments representing a colon tumor, liver, and bone marrow, respectively. The microfluidic channel design promoted unidirectional flow patterns on a pumpless

[1] LaValley DJ and Shuler ML. Pumpless, Unidirectional Microphysiological System for Testing Metabolism-Dependent Chemotherapeutic Toxicity. In preparation.
Author Contributions: D.J.L. designed and performed research, analyzed data, and wrote the paper. M.L.S. designed research and wrote the paper.

platform. The metabolism-dependent toxic effect of Tegafur, an oral prodrug of 5-fluorouracil, combined with uracil was examined in each cell type. Tegafur-uracil treatment induced substantial cell death in HCT-116 cells and this cytotoxic response was reduced for multicellular spheroids compared to a single cell suspension, likely due to diffusion-limited drug penetration. Additionally, off-target toxicity was detected by HL-60 cells, which may provide useful information on dose-limiting side effects. Collectively, the μCCA is a valuable physiologically-based pharmacokinetic drug screening platform to support cancer drug development.

3.2 Introduction

Cancer Drug Development

With the cancer diagnosis rate steadily increasing [1], researchers are continually trying to create new therapeutics for the treatment of cancer. Despite their extensive research, only 10.4% of drug candidates entering preclinical trials ultimately become FDA approved, with a dismal 6.7% approval rate for oncology drugs [2]. The estimated cost to bring a drug to market is $2.8 billion [3], highlighting the need for more effective drug screening to increase the transition from drug development to FDA approval. Thus, if the drug approval rate could be increased even slightly, these high costs of drug development could be drastically reduced.

Drug attrition, or failure to gain approval, is mainly due to lack of drug efficacy or failure to detect toxicity [4]. Approximately 50% of drug candidates entering phase

III of clinical trials, the most expensive period of the drug pipeline, fail [5]. This failure emphasizes the need to create better preclinical models that more accurately predict the potential efficacy of new drug compounds. More importantly, such systems help to eliminate drugs with high toxicity and other side effects at earlier times in the drug development process.

Current *in vitro* and preclinical models are insufficient at predicting drug response within clinical trials [6]. Cell behaviors differ depending on their culture environment (i.e. 2D monolayer versus 3D organoid) [7], and while culture in 2D is easy to implement, this culture method does not accurately recapitulate microenvironments present within the body. In contrast, 3D cell culture is more representative of *in vivo* tissue architectures and promotes relevant cell-cell and cell-ECM interactions, suggesting 3D environments facilitate more authentic cell behaviors. Nonetheless, 3D systems are limited in their variability, requirement for a large number of cells and reagents, and typically lack fluid flow [7,8]. Preclinical cancer models often include animal models [9,10] which are more physiologically relevant, genetically adaptable, and feature complex, whole organism interactions. However, animal models do not represent human physiology, and therefore, their outcomes do not universally translate to clinical outcomes [11]. With this limitation in mind, groups have turned towards models that utilize patient-derived tumor xenografts that include human tumor cells. However, these models require the use of immunocompromised mice [12], and thereby neglect the immune response to a therapeutic compound. Altogether, these

limitations of current preclinical models highlight the need to create better human-based mimetics to aid in the development of new cancer therapeutics.

Tumor Microfluidic Models

Compared to traditional monolayer and organoid preclinical models that solely assess the response of cancer cells, 3D microfluidic devices can better represent the complex, dynamic environment found within the human body. Importantly, 3D microfluidic cancer models are able to recreate important cell-cell and cell-ECM interactions between tumor cells and the tumor stroma that can promote cancer progression [11,13]. Because of their multifactorial nature, these models are potentially more predictive disease models and aid in the development of new therapeutics to combat a wide variety of maladies.

Cancer drug screening via 3D microfluidic models shows promise due to the capability for high parallelization and on-chip readouts. For example, many devices are capable of promoting the formation of multicellular tumor spheroids directly within wells on a microfluidic chip [14–18] for rapid, high throughput testing of up to 80 microwells on a single device [18]. Further, built-in microsensors allow for real-time assessment of drug efficacy [19]. Considering many drug delivery approaches rely on circulation through the bloodstream, some models included vasculature as well as tumor chambers in their designs [20,21]. Consequently, this allows for screening of both anti-cancer and anti-angiogenic therapeutics. Additionally, the tumor microenvironment can significantly influence drug delivery to the tumor core, which motivated some groups

to incorporate fibroblasts into their systems to better mimic *in vivo* tumors [22,23]. These systems demonstrated that fibroblasts protected cancer cells from chemotherapeutic-induced cytotoxicity [24].

Since most current cancer treatment strategies include a regimen of multiple therapeutic agents, tumor-on-chip platforms can be useful models to study and optimize drug combination dosing and timing schedules [25]. The unique microchannel design described by Fan et al. [14] generated a spatio-temporal gradient, which allowed investigation of drug combinations over a wide range of concentrations. Moreover, previous work from our lab studied the simultaneous delivery of two or more therapeutics within physiologically-relevant microfluidic devices [26–28].

It is well known that metastasis accounts for most cancer-related deaths. Thus, numerous microfluidic platforms have been developed to study the intricate steps of cancer dissemination [13]. As solute gradients are important drivers in the early steps of metastasis, models have examined cancer cell chemotaxis and demonstrated that cell migration can be influenced by surrounding stromal cells [29,30]. Additionally, several devices, especially those produced in the Kamm lab, have exquisitely recapitulated both intravasation [31–34] and extravasation [34–38] of cancer cell transmigration across the endothelium into or out of the blood vessel, respectively. Furthermore, as hypoxia is a known driver of metastasis *in vivo* [39], researchers have shown enhanced metastasis in microfluidic systems operated under oxygen-deficient conditions [32,40]. Interestingly, Skardal et al. [41] created a metastasis-on-a-chip platform to model colon cancer

metastasis from the gut to the liver, and their data show that the addition of a matrix metalloproteinase inhibitor in their system reduced cancer cell migration and invasion.

Collectively, these and other microfluidic models of cancer are vital to parse apart and better understand the complex dynamics of the tumor microenvironment. As more sophisticated platforms are being developed, they better represent *in vivo* tumors. The addition of stromal cells is important because they are influencers of cancer cell behavior and drug delivery [42]. More recently, complex 3D structures representing vasculature have been incorporated into some models to mimic the tortuous architecture of native tumor vessels [20,43]. Also, as the immune system can play an important role in cancer development, an emerging area of research is designing microfluidic systems to explore interactions between cancer and immune cells [44,45]. With some designs incorporating primary cancer cells from patients [46], the future of cancer microfluidic devices may include testing new patient-specific therapeutics.

Body-on-a-Chip Technology

Organ-on-a-chip technology refers to microfluidic devices that recapitulate the structure and function of a single human organ using only basic, fundamental units [47]. They are utilized for numerous applications, especially drug discovery and toxicology studies. Previous work from our lab and others have developed models representing the liver [48–53], gastrointestinal tract [54–56], heart [57–59], kidney [60–62], brain [63–65], bone marrow [66], lung [67–69], muscle [70], and skin [71,72], among others.

Perhaps even more beneficial is the combination of several organ-on-a-chip devices to create a more complex, physiologically-relevant body-on-a-chip [73–78].

A body-on-a-chip platform, also called a micro cell culture analog (μCCA) or a microphysiological system (MPS), is a microfluidic device containing chambers representing "organs" interconnected with microchannels to mimic *in vivo* blood flow patterns. Each organ chamber is seeded with living cells, either primary or cell lines, in 2D or 3D microenvironments. Microfluidic channels demonstrate well behaved, laminar flow of a blood surrogate [79]. Body-on-a-chip is a physical representation of a physiologically-based pharmacokinetic (PBPK) model where, using human parameters, each organ is modeled as a chemical reactor and all organs are connected in a physiologically realistic order. PBPK models can describe the adsorption, distribution, metabolism, and excretion, collectively termed ADME, of a drug compound [79,80].

The design criteria for a body-on-a-chip platform includes physiological organ residence times and shear rates, authentic cell responses, and blood flow ratios comparable to those found within the human body [79]. Additionally, a μCCA should mimic the liquid-to-cell ratio of *in vivo* tissue. Each MPS is capable of recapitulating vital cell-cell and organ-organ interactions not possible with conventional methods [81,82]. Importantly, this platform can be used to predict human responses to a potential therapeutic compound, including drug metabolism or other toxic side effects [81,83,84].

Early cell culture analogs (CCAs) were created to investigate naphthalene toxicity within a device based on physiological parameters of a rat [85–87]. Utilizing separate liver and lung chambers, their results showed that hepatocytes created toxic byproducts from naphthalene metabolism that subsequently caused lung cytoxicity [85–87]. Later, CCAs were scaled down to the microscale to create more realistic liquid-to-cell ratios and better mimic *in vivo* fluid residence times [81,88]. Additional μCCAs were developed to further study naphthalene metabolism, and identified which metabolites (i.e. naphthoquinone) induced lung cell death [89] and the impact of drug accumulation within fat tissue [90].

Body-on-a-chip as Alternative Drug Development Models

Body-on-a-chip technology seems promising to aid current preclinical models during the development of new pharmaceuticals. Each MPS is more physiologically relevant than *in vitro* 2D or 3D culture systems and more humanized than current animal models [81,84]. These systems aim to reduce the number of potential drugs needed to be tested on animals by better predicting human responses to the compounds prior to animal testing [84]. Furthermore, a PBPK model and μCCA can be used in conjunction with one another to describe and test the ADME of a drug candidate and predict potential toxic side effects [81].

Previously, our lab has created μCCA devices to assess drug metabolism and cytotoxicity. In a representative GI tract model, Mahler et al. [91] developed a four-chamber device that displayed dose-dependent liver toxicity following acetaminophen

metabolism in both the GI and liver compartments. Additionally, Tatosian et al. [26] designed a four-chamber platform to test drug combinations for multidrug resistant uterine cancer treatment. Interestingly, the data revealed enhanced toxicity of the resistant cancer cells when treated with doxorubicin and two additional modulators. As a chemotherapeutic screening platform, Sung et al. [27] created a three-organ μCCA featuring colon tumor, liver, and bone marrow organs seeded with HCT-116, HepG2/C3A, and Kasumi-1 cells, respectively. Tegafur, an oral prodrug of 5-fluorouracil (5-FU) clinically used to treat colorectal cancer, required bioactivation by hepatocytes, but subsequently induced cancer cell death within the system. Kasumi-1 cells also displayed lower viability following drug treatment due to metabolite circulation. In a related study, Sung et al. [28] created a pumpless μCCA device and a corresponding pharmacokinetic-pharmacodynamic (PK-PD) model to investigate cellular responses to 5-FU. These data highlight the usefulness of combining PK-PD models and body-on-a-chip devices to computationally and experimentally evaluate and develop therapeutics against cancer.

Other body-on-a-chip research also aims to improve the drug development process. Frey et al. [92] created a hanging drop microfluidic device to promote HCT-116 colon cell and primary rat liver cell spheroid formation in multiple parallel wells. Administration of a chemotherapeutic prodrug, cyclophosphamide, induced HCT-116 toxicity only when liver cells were also present. In a similar study, a pumpless μCCA containing the same cell types experienced decreased tumor growth following activation of cyclophosphamide by liver cells [93]. To test an anti-cancer drug, Lee et al. [94]

designed a MPS platform and corresponding PK-PD model containing liver and tumor compartments. Strikingly, their data showed less HeLa cancer cell death than expected following drug administration, which their PK-PD model suggested was the result of competing drug metabolism and cell-killing signaling mechanisms.

In addition, the Marx lab has created multiorgan devices for substance testing in systems containing liver tissue and neurons [95] or liver and skin tissues [96]. Apoptosis of cells was detected in both μCCAs following a two-week treatment period. Kimura et al. [97] constructed a MPS containing separate intestine, liver, and lung compartments separated by a microporous membrane. Various co-culture conditions influenced the extent of induced toxicity upon anti-cancer drug testing. Moreover, Ma et al. [98] designed a two-organ μCCA device and observed toxicity to glioblastoma cells due to metabolites generated in the liver compartment following chemotherapeutic administration. Interestingly, this effect was sensitive to the amount of CYP enzymatic activity within the HepG2/C3A liver cells. Since nephrotoxicity can be result from drug or substance treatment, devices containing liver and kidney compartments have been designed to study kidney cytotoxicity following metabolism of drugs and toxicants [99,100]. Altogether, these examples describe the potential impact of body-on-a-chip technology, along with established *in vitro* and preclinical animal models, to select drug candidates that are more likely to be successful in clinical trials.

In this study, we describe a novel three-chamber μCCA device for anti-cancer drug testing. The colon tumor, liver, and bone marrow chamber sizes and flow rates

were scaled from human data to maintain a physiological residence time for each organ. Recently, our lab designed a microfluidic platform to achieve unidirectional perfusion within a desired channel based on the unique placement of supporting channels and passive valves [101]. Here, a μCCA was constructed utilizing the same design principles as the first physical demonstration featuring unidirectional perfusion to multiple parallel channels. Compared to standard bidirectional flow devices, this multiorgan system mimics the unidirectional flow pattern of the human circulatory system. When applied for drug testing applications, our data show therapeutic efficiency as a function of cell culture geometry and the presence of flow. Further, undesired toxicity was detected in distant organs, which may help to determine tolerable drug doses.

3.3 Materials and Methods

Cell Culture

Three cell lines were used in this study: HCT-116 colorectal carcinoma cell line (ATCC, Manassas, VA) maintained in McCoy's 5A (Thermo Fisher Scientific, Waltham, MA) supplemented with 10% v/v FBS (Thermo Fisher Scientific), HepG2/C3A hepatocellular carcinoma cells (ATCC) cultured in MEM (Thermo Fisher Scientific) with 10% v/v FBS (Thermo Fisher Scientific), and HL-60 promyeloblasts (ATCC) maintained in IMDM (Thermo Fisher Scientific) with 20% v/v FBS (Thermo Fisher Scientific). A common medium utilized within the device consisted of a 1:1:1 v/v ratio of each culture medium.

Device Design and Fabrication

The three-organ microphysiological system was comprised of an outer poly(methyl methacrylate) (PMMA) frame with inner channel layer and cell culture insert (Figure 3.1A). The top housing piece was cut from a 3 mm PMMA sheet (McMaster-Carr, Elmhurst, IL) using a VersaLaser VLS3.60 cutting and engraving CO_2 laser (Universal Laser Systems, Scottsdale, AZ) with two 5.5 mm thick PMMA (McMaster-Carr) reservoirs permanently bonded above with an acrylic cement (McMaster-Carr). Similarly, the bottom piece was cut from a 5.5 mm PMMA sheet (McMaster-Carr) using laser ablation and fit with flanged screw-to-expand inserts (McMaster-Carr). A microfluidic channel layer was created by etching channels into a 1.5 mm PMMA sheet (McMaster-Carr) using the CO_2 laser. The cell culture insert consisted of two 0.8 mm silicone gaskets (Grace Bio-Labs, Bend, OR) sandwiching a polycarbonate membrane (0.4 μm pore size; Whatman, Clifton, NJ). Additional 0.8 mm silicone sealing gaskets (Grace Bio-Labs) were utilized to prevent leaking. All silicone layers were fabricated using laser ablation. Each device was held together with eight stainless steel screws (McMaster-Carr).

The cell culture insert contained three separate chambers representing a colon tumor, liver, and bone marrow tissue scaled appropriately from human physiological organ sizes [102–104] by a factor of approximately 40,000 (Table 3.1).

For static experiments, a similar cell culture insert (overall diameter 25 mm) was cut from silicone gaskets (Grace Bio-Labs) as described above. The insert was placed inside of a sterile 35 mm culture dish with an equivalent amount of media as a single µCCA.

Microfluidic Channel Design

The microfluidic channel layer (Figure 3.1B) was designed to yield unidirectional flow through the center channel network as described previously [101]. Briefly, the inlet and outlet channels were positioned to create an air-liquid interface in the top reservoir, preventing flow into the top outlet hole by capillary forces. Once the device was tilted in the opposite direction, an air-liquid interface was established in the other reservoir, ultimately permitting flow in only one direction from the inlet channel to the outlet channel in both tilt orientations. These passive valves served as an inherent backflow-proof mechanism.

Individual channel dimensions were selected to mimic human organ flow rates obtained from literature [102–104] using a residence time-based scaling approach (Table 3.1). Fluid flow throughout the device was gravity-driven and calculated from the following equations.

$$\tau = \frac{V}{Q} \tag{3.1}$$

where τ is the residence time, V is the organ volume, and Q is the volumetric flow rate.

$$Q = \frac{\Delta P}{R} \tag{3.2}$$

where Q is the volumetric flow rate and ΔP and R are the pressure drop and hydrodynamic resistance, respectively.

$$\Delta P = \rho\, g\, \Delta h = \rho\, g\, L\, \sin(\theta) \tag{3.3}$$

where ΔP is the pressure drop, ρ is the fluid density, g is the gravitational constant, Δh is the height difference, L is the distance between the inlet and outlet, and θ is the rocker tilt angle.

$$R = \frac{12\mu l}{wh^3}\left[1 - \frac{192h}{\pi^5 w}\tanh\left(\frac{\pi w}{2h}\right)\right]^{-1} \tag{3.4}$$

where R is the hydrodynamic resistance, μ is the dynamic fluid viscosity, and l, w, h are the channel length, width, and height, respectively [105].

Device Assembly and Operation

One day prior to assembly, cells were seeded onto autoclaved cell culture inserts. Inserts were coated with 0.2 mg mL^{-1} type I collagen (Thermo Fisher Scientific) in 1x PBS for 1 h at 37°C. Two day old HCT-116 hanging drops initially seeded at 2.5 cells mm^{-3} were collected and embedded within a 3.5 mg mL^{-1} collagen hydrogel as previously described [106] with slight modifications. Briefly, high density type I collagen solution (Corning, Corning, NY) was neutralized with 500 mM HEPES (VWR, Radnor, PA) in 10x PBS and polymerized for 15 min at room temperature followed by 60 min at 37°C. Similarly, HepG2/C3A and HL-60 cells were resuspended at 2400 cells mm^{-3} and 1800 cells mm^{-3}, respectively, and embedded within 2 mg mL^{-1} collagen hydrogels. Following

polymerization, 20 mL device medium was added to the dish containing the cell culture insert and then incubated overnight at 37^{o}C.

Before assembling the device, silicone gaskets were autoclaved and PMMA layers were cleaned with three 30 min washes containing Penicillin-Streptomycin (Thermo Fisher Scientific) in sterile water. Each μCCA was assembled from the bottom-up with media added between layers and each layer lowered slowly on top to prevent bubbles from entering the system. After the top housing piece was placed, the reservoirs were filled with media and the layers were secured with screws. Any remaining bubbles in the system were removed by gentle pipetting from the reservoirs.

Following assembly, 400 μL of media was added to each reservoir and the entire device was placed inside of a sterile dish. Multiple devices were operated simultaneously on a pumpless rocker platform (Next Advance, Averill Park, NY) custom programmed for a $\pm$15^{o} tilt angle at every 1 min interval. The entire system was placed inside of a 5% CO_2 incubator and operated for up to 4 days with 50% daily nutrient replenishment.

Fluid Dynamics Studies

The device was assembled omitting the cell culture insert and placed on a custom-made stand oriented at a 15^{o} tilt angle. A solution containing 0.02 g mL^{-1} violet polyethylene microspheres (45-53 μm diameter; Cospheric, Santa Barbara, CA) was added to the top reservoir. Bead movement through individual channels was recorded with a Flea3 USB

3.1 camera (FLIR Integrated Imaging Solutions Inc, Nashua, NH). Linear bead flow rates were calculated in ImageJ.

Viability Staining and Analysis

After 1 or 4 days of operation, devices were disassembled and the cell culture insert was removed and stained. Cell-embedded hydrogels were rinsed with PBS and incubated with live/dead stain solution (16 μM calcein AM, 16 μM ethidium homodimer; Thermo Fisher Scientific) for 1 h at 37ºC. Following at least 3 washes, cells were fixed with 4% v/v paraformaldehyde (Electron Microscopy Systems, Hatfield, PA) for 30 min at room temperature. Fluorescent images were obtained with a fluorescent microscope (Olympus, Center Valley, PA) equipped with a 4x objective and a Zeiss LSM 800 confocal microscope (Carl Zeiss, Oberkochen, Germany) with a 10x water-immersion objective. Images are presented as maximum intensity projections of z-stacks unless otherwise stated. The average number of cells per image was calculated in ImageJ by thresholding images and analyzing particles. Viability was reported as the ratio of live cells to total cell number.

Albumin and Urea Assays

Spent media samples were collected 1 and 4 days post assembly and stored at -80ºC. Albumin levels were measured using the ELISA Starter Accessory Kit (#E80-129; Bethyl Laboratories, Montgomery, TX) following the manufacturer's instructions. Samples were read on a spectrophotometer at 450 nm. Samples were diluted until

readings were within the linear range of the standard curve. Results were compared to the standard curve and are expressed as μg mL^{-1}.

Similarly, urea production was measured with the QuantiChrom™ Urea Assay Kit (#DIUR-100; BioAssay Systems, Hayward, CA) following the manufacturer's instructions. Briefly, 200 μL of chromogenic reagent was added to 50 μL of media, incubated for 20 min at room temperature, and then samples were read on a spectrophotometer at 520 nm. The results were compared to the standard curve and are expressed as mg dL^{-1}.

CYP450 Enzymatic Activity

Two days after device assembly, cells were incubated with 25 μM rifampicin (Sigma-Aldrich, St. Louis, MO) or DMSO vehicle (Sigma-Aldrich). After two days of incubation with the induction reagent, media samples were collected and stored at -80°C until the assay was run. CYP3A4 enzyme activity was measured using the P450-Glo™ Assay (#V9002; Promega, Madison, WI) following the manufacturer's instructions. Samples were read on a luminometer. The results were compared to a standard curve and are expressed as nM.

Drug Cytotoxicity Studies

To initially test the efficiency of Tegafur-uracil (UFT) combination therapy, 6 well plates were incubated with 0.1 mg mL^{-1} collagen (Thermo Fisher Scientific) in PBS for 1 h at 37°C and then seeded with 175 cells mm^{-3} HCT-116 cells in the center of the well.

If desired, 200 cells mm^{-3} HepG2/C3A were seeded around the edge of the well. One day post seeding, cells were stimulated with 200 µM Tegafur (Sigma-Aldrich), 800 µM uracil (Sigma-Aldrich), 200/800 µM UFT treatment (Sigma-Aldrich), 50 µM 5-FU (Sigma-Aldrich), or DMSO vehicle (Sigma-Aldrich). After 3 days, cells were stained with live/dead solution (2 µM calcein AM, 2 µM ethidium homodimer; Thermo Fisher Scientific) and cell viability was assessed as described previously.

For additional UFT-induced cytotoxicity studies, each cell culture insert was seeded with HCT-116 spheroids as described above, or 350 cells mm^{-3} HCT-116 embedded within a 3.5 mg mL^{-1} collagen gel for experiments where a single cell suspension was desired. Similarly, 2400 cells mm^{-3} HepG2/C3A and 1800 cells mm^{-3} HL-60 were embedded within 2 mg mL^{-1} collagen gels and seeded into their respective chambers on the cell culture insert. Each device was assembled as explained previously. One day post assembly, devices were incubated with 200/800 µM UFT (Sigma-Aldrich) or DMSO vehicle (Sigma-Aldrich). After 3-day drug treatment, cytotoxicity was determined by live/dead staining (16 µM calcein AM, 16 µM ethidium homodimer; Thermo Fisher Scientific) and viability analysis as described above.

Statistical Analysis

Data are presented as mean $\pm$ standard deviation (SD). All analyses were performed in Excel 2016 (Microsoft, Redmond, WA) using one-way ANOVA with post-hoc Tukey's honest significant difference test. $P < 0.05$ was considered significant.

3.4 Results

Three-Chamber, Pumpless, Unidirectional Device Design

We created a novel three-chamber microfluidic platform for chemotherapeutic testing applications, which includes drug metabolism and off-target toxicological effects. Our design contained alternating PMMA sheets patterned with microchannels and reservoirs, and silicone sealing gaskets (Figure 3.1A). Colon cancer cells, hepatocytes, and promyeloblasts were cultured within chambers representing colon, liver, and bone marrow tissue, respectively. The microfluidic channel layer featured a central network of parallel channels delivering individualized flow rates to each organ chamber (Figure 3.1B). Importantly, using previously described design principles [101], it promoted a physiologically-relevant unidirectional flow pattern. Furthermore, the assembled device (Figure 3.1C) was maintained without the need for external pumps or tubing, instead utilizing gravity-driven flow on a rocker platform, as characterized previously [28].

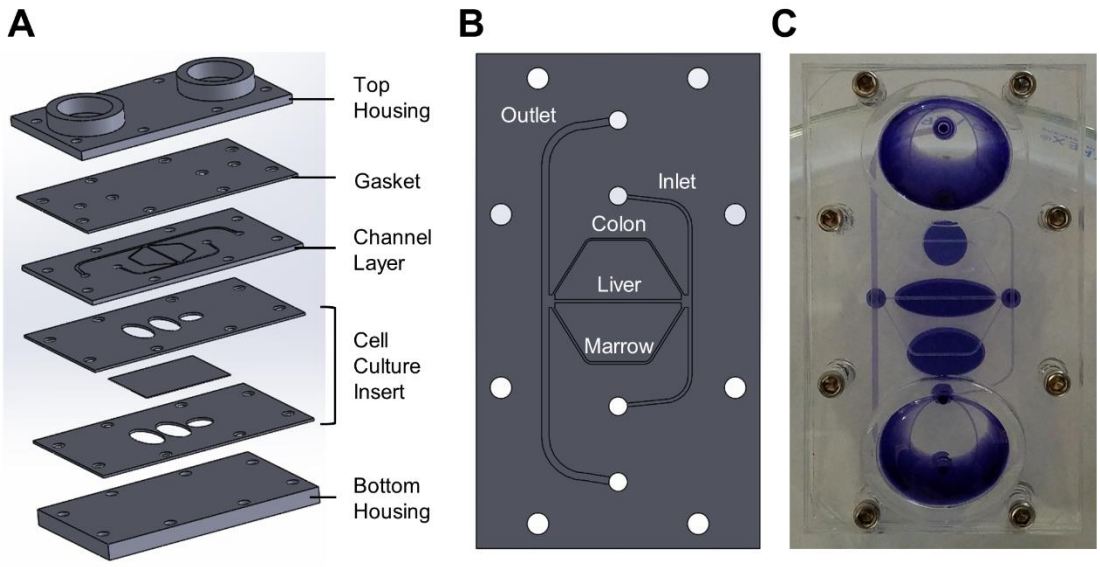

Figure 3.1. Three-chamber microphysiological system design. (A) An assembled view of the device comprised of outer housing pieces with exposed reservoirs, a sealing gasket, and channel layer positioned above the cell culture insert. (B) Schematic of the microfluidic channel layer featuring a network of parallel channels to the inner organ chambers and outer inlet and outlet channels. (C) A picture of an assembled device filled with blue dye for visualization of the cell chambers and channels.

Our design applied a residence time-based scaling approach (Table 3.1) from human data [102–104]. Channel dimensions were selected to mimic physiological blood flow rates within the human body, as 64%, 23%, and 13% of the total flow distribution to the liver, bone marrow, and colon compartments, respectively [102–104]. Flow rates of the individual channels were measured by tracking the movement of colorimetric beads (Table 3.2). The measured values were all within 13% of the calculated flow rates.

Unidirectionality of the channel design was examined by visualization of colored dyes within the assembled μCCA (Figure 3.2). The device was first angled in one orientation and a yellow dye was placed in the top reservoir (Figure 3.2A). Using gravity as the driving force, the yellow dye flowed through the inlet channel, across the central channel network, and accumulated in the lower reservoir (Figure 3.2B). Next, the device was tilted in the opposite orientation and a green dye was placed in the new top reservoir (Figure 3.2C). As before, gravity-driven flow directed the green dye through the center channels (Figure 3.2D) and collected in the initial reservoir (Figure 3.2E). Notably, the direction of flow through the inner channel network remained constant regardless of the tilt orientation, confirming unidirectional flow.

Table 3.1. Physiologically-relevant microfluidic chip values were selected using a residence time-based scaling approach from human data.

	Human Data[a]			**On-Chip Data**	
	Organ Volume (L)	Flow Rate (L/min)	Residence Time (min)	Chamber Volume (µL)	Flow Rate (µL/min)
Colon	0.38	0.26	1.46	10.0	6.91
Liver	1.57	1.32	1.19	41.2	34.6
Bone Marrow	1.59	0.48	3.31	41.7	12.6

a. Price et al. (2003), Brown et al. (1997), Forrester et al. (1980)

Table 3.2. Calculated and measured volumetric flow rates of individual channels within the multiorgan system.

	Flow Rate (mm^3/min)	
	Calculation	*Measurement*
Colon	6.91	7.34 $\pm$ 0.12
Liver	34.6	35.4 $\pm$ 0.96
Bone Marrow	12.6	14.2 $\pm$ 0.46

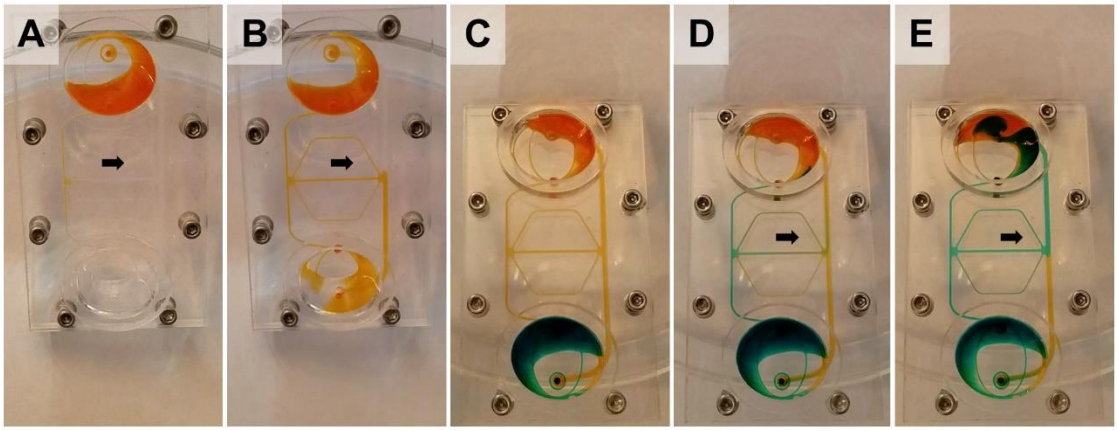

Figure 3.2. Unidirectional flow within the μCCA. (A-B) While tilted in one direction, a yellow dye is placed in the top reservoir and begins to flow into the central channel network to the second reservoir (arrow). (C) The tilt angle is reversed and green dye is placed in the other reservoir. (D-E) The green dye flows through the center channels in the same direction as the previous yellow dye and empties into the initial reservoir. Arrows indicates direction of flow. Backflow is prevented through the central channel network by passive valves.

Viability and Cell Functionality Within the Microphysiological System

To ensure long term operation of the μCCA, cell viability was assessed via live/dead staining 1 and 4 days after device assembly (Figure 3.3). Cell culture inserts were seeded with HCT-116 multicellular spheroids, HepG2/C3A hepatocytes, and HL-60 promyeloblasts, all embedded within collagen hydrogels. Our results demonstrate that all three cell lines maintained over 90% viability when cultured up to 4 days within the device (Figure 3.3B-D), indicating adequate oxygen and nutrient supply to each organ chamber. Moreover, cell viability within the system was comparable to viability achieved within static cultures containing similar a volume of culture medium (Figure 3.3B-D).

Additionally, liver cells were examined for the production of albumin and urea (Figure 3.4), indicators of proper liver function. All three cell lines were cultured up to 4 days within the μCCA or under static conditions. Our results indicate that, when cultured in either arrangement, albumin synthesis increased dramatically from 1 to 4 days (Figure 3.4A). However, no significant differences were detected between the μCCA and static control at either time point. Likewise, both static and device groups fostered high urea production 1-day post assembly that persisted for up to 4 days (Figure 3.4B), but there were no observable differences between the two systems.

Furthermore, cytochrome P450 enzymes, located mainly in the liver, are vital for the metabolism of drugs and xenobiotics. In particular, CYP3A4 is highly expressed in humans and plays a major role in most P450-mediated drug metabolism events

[107,108]. Therefore, we probed for CYP3A4 enzymatic activity within the μCCA or static setup operated under control conditions or with the addition of rifampicin to induce CYP gene expression (Figure 3.4C). As expected, a greater amount of CYP3A4 activity was measured for induced groups compared to controls. Interestingly, rifampicin-treated cells cultured within the flow device experienced significantly higher CYP3A4 activity compared to the corresponding static control (Figure 3.4C), suggesting more authentic CYP3A4 production when the cells were exposed to flow.

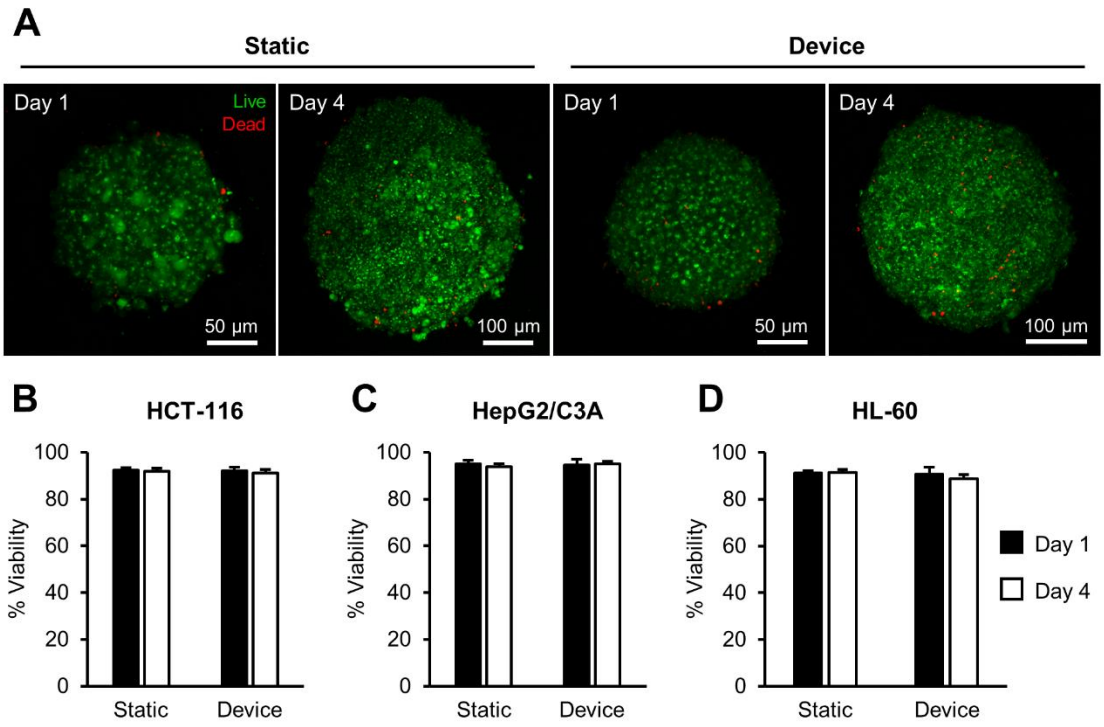

Figure 3.3. High viability of each cell line cultured within the three-organ microphysiological system. (A) Representative live/dead images of HCT-116 colon spheroids embedded in collagen gels cultured up to 4 days in the device or static control. Quantified viability of HCT-116 spheroids (B), HepG2/C3A hepatocytes (C), and HL-60 promyeloblasts (D) embedded within collagen gels and maintained up to 4 days on the µCCA or within a comparable static design. Values are mean $\pm$ SD. N = 3 independent experiments.

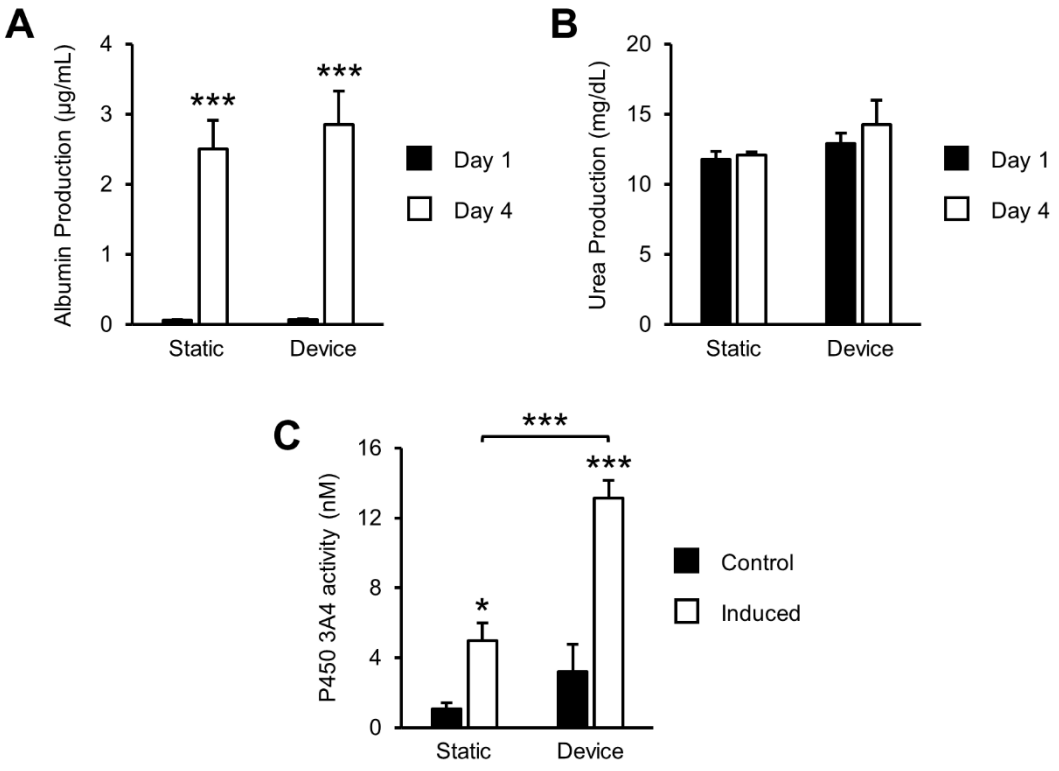

Figure 3.4. Cells within the µCCA maintain vital metabolic functions over four days of device operation. The production of albumin (A) and urea (B) within the three-organ device and static control over 4 days. Values are mean ± SD. N = 3 independent experiments. *** $p<0.001$ compared to Day 1. (C) CYP3A4 enzyme activity on Day 4 for control and rifampicin-induced groups. Values are mean ± SD. N = 2 independent experiments. * $p<0.05$, *** $p<0.001$.

UFT Combination Therapy

5-FU has been widely used in the treatment of cancer, particularly colorectal cancer, for over 50 years [109]. However, 5-FU monotherapy is relatively ineffective, mainly due to rapid degradation by dihydropyrimidine dehydrogenase (DPD) in the liver [110]. Tegafur, an oral prodrug of 5-FU, has increased bioavailability and aims to minimize off-target toxicity [110]. Furthermore, Fujii and colleagues [111] observed enhanced Tegafur toxicity when co-administered with uracil, due to its competitive inhibition for DPD. The optimal combination of Tegafur and uracil (UFT) was identified as a 1:4 molar ratio [111].

Similarly, we investigated Tegafur-induced cytotoxicity with or without uracil supplementation in our system (Figure 3.5). HCT-116 cancer cells were cultured in the presence of HepG2/C3A cells and stimulated with 200 μM Tegafur, 800 μM uracil, 200/800 μM UFT combination therapy, or DMSO control. While the individual components did not significantly affect HCT-116 viability, the combined effect of UFT treatment effectively killed the cancer cells (Figure 3.5B).

To further test UFT-induced cytotoxicity, colon cells were cultured in the presence or absence of liver cells and subjected to various drug conditions (Figure 3.6). As before, the UFT combination regimen reduced HCT-116 cell viability compared to control conditions. However, when liver cells were not present within the system, this cytotoxic effect decreased dramatically (Figure 3.6B), indicating that P450 enzymes present within the liver cells were required to convert Tegafur to its active metabolites.

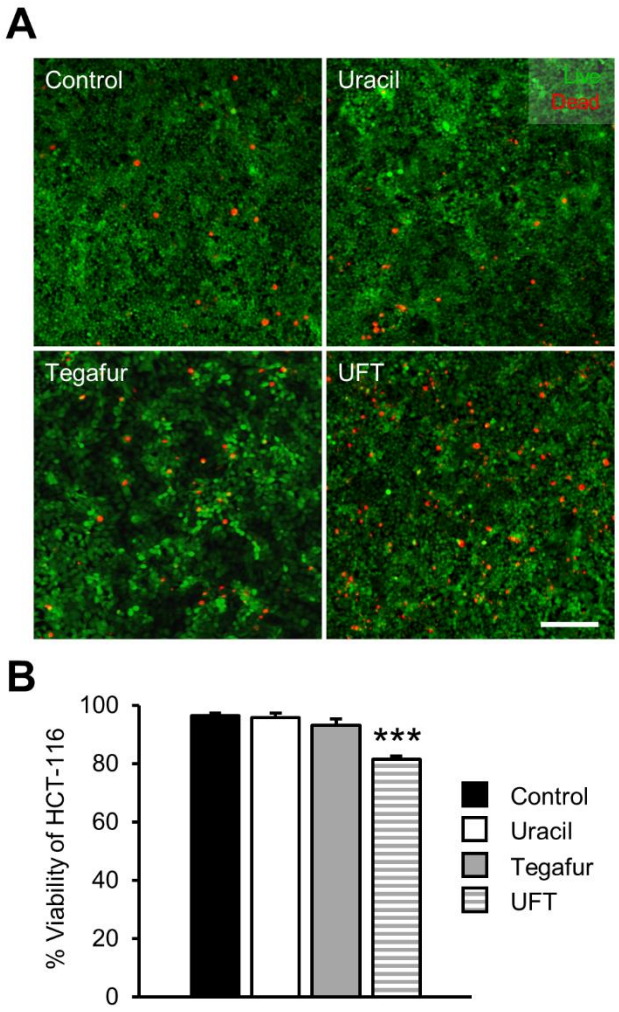

Figure 3.5. Tegafur and uracil (UFT) combination therapy reduces cancer cell viability. Representative live/dead images (A) and quantification (B) of HCT-116 cell viability. With colon and liver cells together in culture, UFT significantly decreased colon cell viability. Each individual agent did not have a significant effect. Values are mean $\pm$ SD. N = 3 independent experiments. *** indicates $p<0.001$ compared to control. Scale bar, 200 μm.

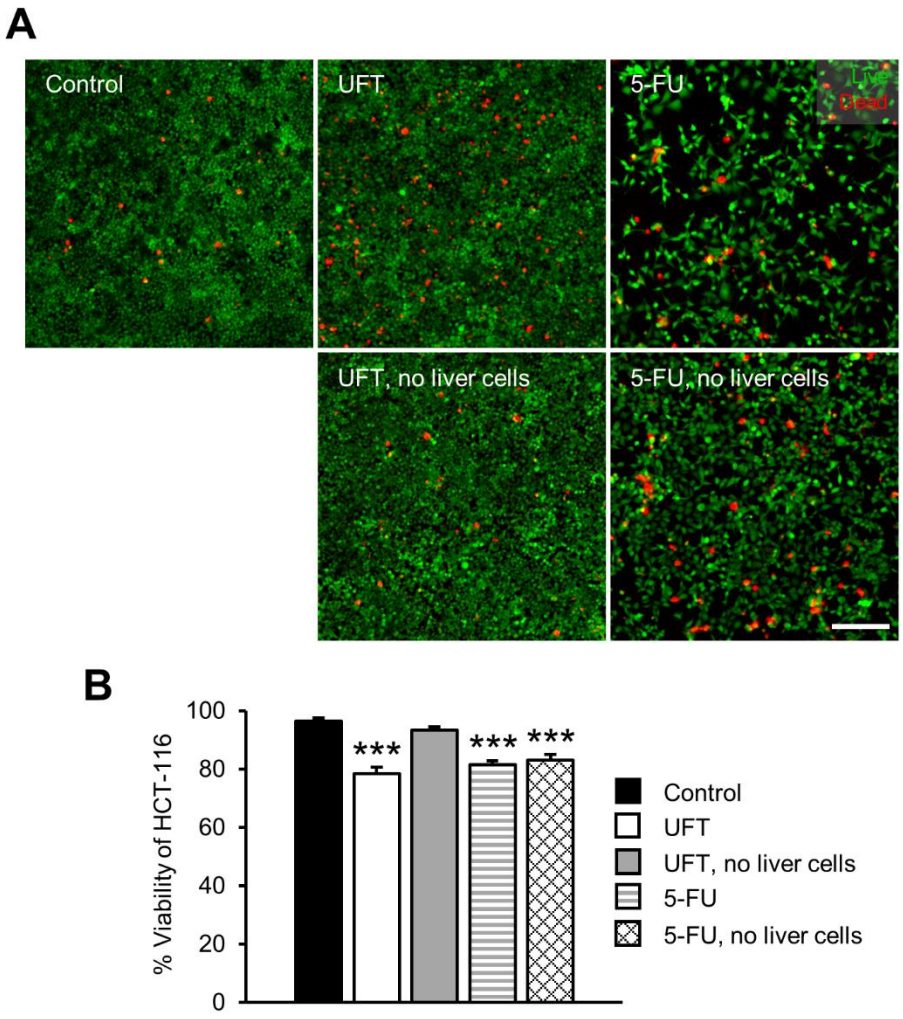

Figure 3.6. Liver enzymes are required to convert Tegafur to its active metabolites. Representative live/dead stained images (A) and quantification of HCT-116 viability (B) following 3-day drug treatment. Compared to control conditions, the administration of UFT reduced HCT-116 viability. When the liver cells were removed, this cytotoxic effect was significantly attenuated. Contrarily, 5-FU treatment induced cytotoxicity regardless of the presence of liver cells in culture. Values are mean $\pm$ SD. N = 3 independent experiments. *** indicates $p<0.001$ compared to control. Scale bar, 200 μm.

Moreover, 5-FU was added to HCT-116 cells cultured with or without HepG2/C3A cells. Our data reveal that, unlike UFT, 5-FU successfully induced cancer cell toxicity under both conditions (Figure 3.6B), verifying its bioactivity without requiring activation from specific liver enzymes.

Anti-Cancer Drug Testing Within the μCCA

Based on the current 6.7% cancer drug approval rate [2], new approaches, such as this MPS, are necessary to improve existing preclinical models for chemotherapeutic drug discovery. As such, we investigated UFT treatment efficacy in our device as a function of cell culture geometry (Figure 3.7). Each μCCA was assembled with all three cell lines, HCT-116, HepG2/C3A, and HL-60, embedded in collagen gels in their respective organ chambers on the cell culture insert. HCT-116 cancer cells were either cultured as a single cell suspension, which proliferated into small cell clusters over the 3-day period, or multicellular spheroids. Both devices and static cultures were challenged with a 200/800 μM UFT regimen or DMSO vehicle for 3 days, and then analyzed by live/dead staining. Our data show that UFT treatment induced significant HCT-116 cell death across all conditions (Figure 3.7B). Compared to static controls, cancer cells within the devices exhibited greater toxicity, indicating the presence of flow promoted increased circulation of metabolites to the colon chamber. Interestingly, UFT-treated multicellular spheroids cultured within the μCCA displayed higher viability than the HCT-116 single cell suspension in the device following UFT treatment (Figure 3.7B). Collectively, these data demonstrate how fluid flow and cell geometry can evoke differential toxicological responses to an anti-cancer therapeutic.

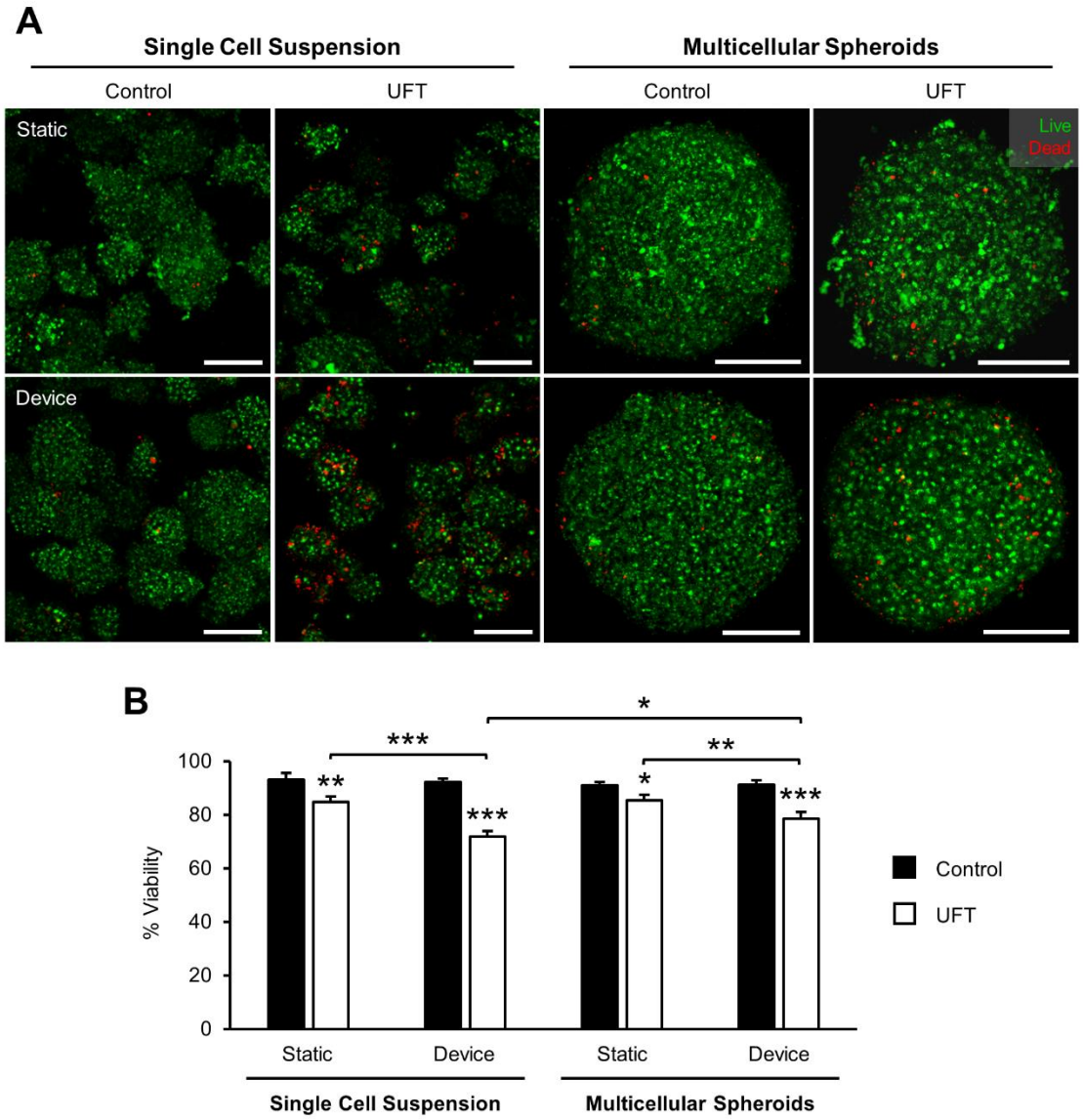

Figure 3.7. Chemotherapeutic efficiency is influenced by cell culture geometry and the presence of flow within the μCCA. Representative live/dead images (A) and quantification (B) of HCT-116 cell viability following 3-day UFT treatment. Cells were initially seeded as a single cell suspension (left panels) or within multicellular spheroids (right panels). The addition of UFT reduced viability across all conditions. While in the device, HCT-116 cells experienced enhanced toxicity compared to static controls. Further, the UFT-induced cytotoxic effect was weakened for multicellular spheroids. Values are mean ± SD. N = 3 independent experiments. * $p<0.05$, ** $p<0.01$, *** $p<0.001$. Scale bars, 100 μm.

Drug attrition is frequently due to off-target toxicity [4]. Since current preclinical models often fail to identify this, toxic effects are not detected until later stages of clinical trials, at which point most of the high drug development costs have already been incurred [3]. One possible solution is to create better human-based mimics to correctly predict toxicity within humans at early stages in the process. Therefore, our three-organ MPS design included one chamber representing bone marrow to study undesired toxicity during chemotherapeutic testing. Colon, liver, and bone marrow chambers were seeded with HCT-116, HepG2/C3A, and HL-60 cells, respectively, cultured within the μCCA or under static conditions, and subjected to 3-day UFT treatment. Our results indicate that HepG2/C3A liver cells did not experience any significant UFT-induced toxicity in either the device or static control (Figure 3.8A-B). Contrarily, HL-60 cells displayed reduced viability following UFT administration in the μCCA (Figure 3.8C-D), suggesting that recirculation of active metabolites generated within the liver compartment subsequently induced toxicity in other organs.

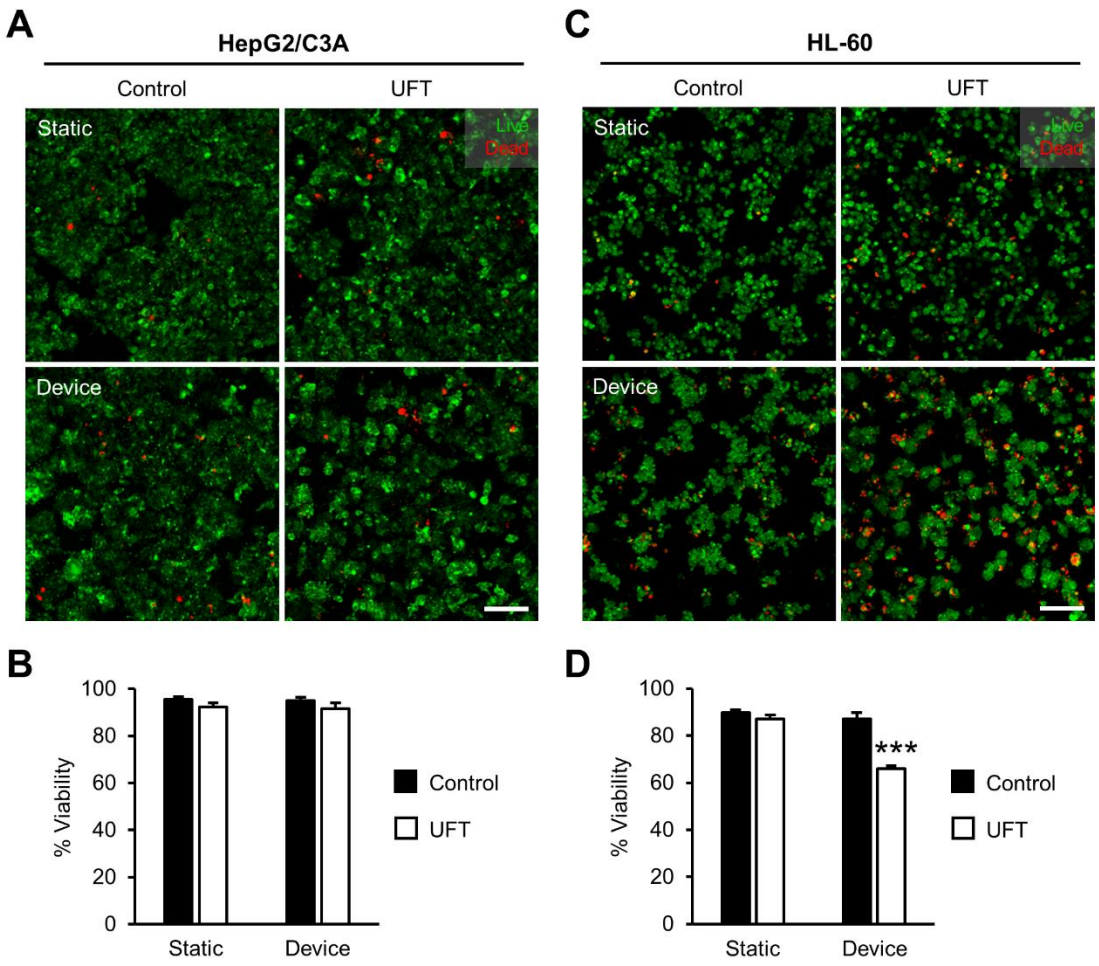

Figure 3.8. Off-target effects of UFT treatment in the multiorgan device induce HL-60 cytotoxicity. Images of live/dead staining (A) and HepG2/C3A cell viability (B) cultured within the μCCA or static conditions after 3 days of UFT therapy. HepG2/C3A viability is not significantly influenced by the addition of UFT in either system. Representative live/dead images (C) and quantification (D) of HL-60 cell viability with or without 3-day UFT treatment. Within the device only, HL-60 viability is substantially reduced following UFT administration. Values are mean ± SD. N = 4 independent experiments. *** $p<0.001$. Scale bars, 100 μm.

3.5 Discussion

We designed and characterized a three-chamber MPS suitable for anti-cancer drug testing which included many beneficial aspects. The device consisted of alternating PMMA and silicone layers. PMMA was selected as the device material for its rigidity, transparency, and inertness, whereas other materials commonly used in microfluidic devices, such as PDMS, can absorb small molecules [112], which may influence drug screening results. The use of silicone promoted biocompatibility and prevented leaking of the overall device. Although silicone can also absorb small molecules, the surface area of silicone exposed to medium was minimal. In addition, the separate cell culture layer reduced the risk of contamination and allowed for a flexible culturing schedule, where specific conditions could be optimized for each cell type prior to device assembly.

Blood circulation within the human body follows a specific route to ensure proper oxygen delivery to all organs. To mimic pulsatile flow in the same distinct pattern, many microfluidic devices utilize a peristatic pump, however, it requires the use of external tubing, increases the medium volume requirement, and increases the cost and complexity to operate the devices. Often, bubbles generate during longer time operation, which led to the design of several bubble traps [113]. To alleviate these issues, our lab developed a gravity-driven, pumpless system featuring reciprocating flow between two reservoirs [28]. Consequently, buoyancy restrictions prevented bubble formation within the system. Further, our lab recently designed a pumpless microfluidic platform to achieve unidirectional perfusion within a desired channel [101]. The device was tested with shear stress-sensitive endothelial cells and

recapitulated cell behavior similar to native tissue under laminar flow. In this study, a μCCA was designed as the first physical demonstration of the previously depicted unidirectional design [101] applied to a multiorgan system. Thus, the three-chamber μCCA device serves as a physiologically-relevant model of blood circulation and could incorporate endothelial cells into future experiments to investigate the effects of anti-cancer drugs on endothelial cell biology.

Uracil supplementation has been shown to enhance Tegafur efficacy clinically [114–116] and within *in vitro* experiments [27,28,111,117], including our own. An estimated 80% of administered 5-FU is metabolized by DPD, typically in the liver, resulting in a half-life of only 8 to 20 minutes [118]. Therefore, 5-FU degradation by DPD significantly limits its potential use as a monotherapy [109,110]. However, uracil acts as a natural substrate for DPD, and when co-administered with either 5-FU or Tegafur, the metabolic rate of 5-FU decreases and a larger concentration of drug remains available due to competitive inhibition of both uracil and 5-FU for DPD [110]. Moreover, the optimal combination of Tegafur and uracil at a 1:4 molar ratio was selected after it resulted in the greatest ratio of 5-FU concentration in the tumor to that in the blood during preclinical testing [111]. Additional *in vitro* studies demonstrated that the addition of uracil in excess could reduce up to 70% of 5-FU degradation by liver enzymes [119]. Altogether, the μCCA may be a useful tool to study the complex dynamics of DPD-mediated metabolism of 5-FU, Tegafur, and uracil in a physiologically-relevant manner. Further, since the level of DPD expression varies over

20-fold in the human population [120], a device with patient-derived cells could be used to predict the best dosing schedule for that patient.

Multicellular spheroids have long been used as tumor models because they mimic *in vivo* cell-cell and cell-matrix interactions and contain distinct regions of proliferating, quiescent, and necrotic cells. They can also accurately recreate physiochemical gradients, including oxygen and nutrient diffusion and metabolic waste accumulation within the tumor core [121,122]. Here, UFT efficiency as a function of cell culture geometry was examined, and our results indicate significantly less HCT-116 cytotoxicity when cultured as multicellular spheroids within the μCCA, as compared to a single cell suspension. Since diffusion of many molecules, especially oxygen, within spheroids is limited to distances of approximately 200 μm [123,124], this suggests reduced drug penetration in spheroids cultured within our device. Others have observed a similar phenomenon in both *in vitro* [125–129] and computational [130,131] experiments. Therefore, our model accurately reflects some of the drug transport limitations that occur *in vivo*, such as complex tumor architecture and dense extracellular matrix surrounding a tumor that can severely limit the diffusive delivery of therapeutics [132,133].

Off-target toxicity accounts for approximately 40% of new drug failures, the largest cause of drug attrition [4]. In particular, a known major side effect to 5-FU therapy is myelotoxicity [110,134]. Thus, we designed our system with the capability to examine cytotoxic effects on non-tumor cells following administration of anti-cancer

therapeutics. Within the μCCA, the bone marrow chamber cultured with HL-60 promyeloblasts in a collagen hydrogel displayed significant cell death following a 3-day UFT regimen. The amount of HL-60 cytotoxicity was comparable to that observed by the intended HCT-116 colon cancer cells. Accordingly, hematological toxicity is often one of the dose-limiting toxicities reducing the clinical use of intensive 5-FU dosing strategies [134,135]. Therefore, this MPS could be utilized to test dose-dependent adverse side effects in bone marrow or other various organs during preclinical drug testing.

Although it is a more physiologically-relevant model for drug testing, body-on-a-chip technology does contain its limitations. Compared to 2D systems, it is currently more expensive to design and operate μCCAs, and results in lower throughput, than traditional drug screening methods. Many devices, including this one, rely on the use of serum-containing medium and immortalized cell lines, which often have lower enzymatic expression and activity than cells *in vivo* [136]. Future studies could be done using primary cells and a serum-free defined medium composition, as described previously [73], to alleviate these problems. Moreover, the culture of a patient's cells within the device would allow for a patient-specific body-on-a-chip device, an opportunity for personalized medicine [137].

In addition, we explored the use of a single treatment, UFT, within this system. However, clinically, CRC is typically treated with combination therapy [138]. As such, this device has the potential to examine countless combinations of drugs and provide

efficacy and toxicity data that may better inform CRC clinical trials [139–141]. Furthermore, each μCCA design must select which organs to include and exclude within the model. Here, we chose to include only three organs within our μCCA device, which ultimately excludes other interactions that are known to occur within the body, such as drug elimination via the kidneys [60].

3.6 Conclusion

Only recently have organ- and body-on-a-chip technologies begun to reach the commercial market space [142], with a major focus on reducing the excessively high costs for drug development. Herein, we propose a novel body-on-a-chip device to aid in the discovery of new cancer therapeutics. The three-chamber μCCA features pumpless, gravity-driven, unidirectional flow to closely represent *in vivo* blood flow patterns. Multicellular colon cancer spheroids were incorporated to recapitulate complex tumor architecture and cell heterogeneity. The multiorgan system displayed cytotoxicity against the intended cancer cells following Tegafur-uracil treatment, along with undesired toxicity in bone marrow cells due to metabolite circulation. Altogether, this drug testing platform could be a valuable tool to study the pharmacokinetics of novel anti-cancer therapeutic candidates, including toxicological side effects in distant organs.

3.7 Acknowledgments

This work was performed in part at the Cornell NanoScale Science and Technology Facility, a member of the National Nanotechnology Coordinated Infrastructure, which is supported by the National Science Foundation (grant NNCI-1542081). Confocal imaging was performed at the Biotechnology Resource Center (NYSTEM CO29155 and NIH S10OD018516) at Cornell. This work was also supported by grants from the National Institute of Health (U01CA214300) to M.L.S and the National Science Foundation Graduate Research Fellowship Program to D.J.L. M.L.S. is the CEO and president of Hesperos, Inc., which is commercializing body-on-a-chip devices.

REFERENCES

1. Siegel RL, Miller KD, Jemal A. Cancer Statistics, 2018. CA Cancer J Clin. 2018;68(1):7–30.
2. Hay M, Thomas DW, Craighead JL, Economides C, Rosenthal J. Clinical development success rates for investigational drugs. Nat Biotechnol. 2014;32(1):40–51.
3. DiMasi JA, Grabowski HG, Hansen RW. Innovation in the pharmaceutical industry: New estimates of R&D costs. J Health Econ. 2016;47:20–33.
4. Waring MJ, Arrowsmith J, Leach AR, Leeson PD, Mandrell S, Owen RM, Pairaudeau G, Pennie WD, Pickett SD, Wang J, Wallace O, Weir A. An analysis of the attrition of drug candidates from four major pharmaceutical companies. Nat Rev Drug Discov. 2015;14:475–86.
5. Hwang TJ, Carpenter D, Lauffenburger JC, Wang B, Franklin JM, Kesselheim AS. Failure of investigational drugs in late-stage clinical development and publication of trial results. JAMA Intern Med. 2016;176(12):1826–33.
6. Johnson JI, Decker S, Zaharevitz D, Rubinstein L V, Venditti JM, Schepartz S, Kalyandrug S, Christian M, Arbuck S, Hollingshead M, Sausville EA. Relationships between drug activity in NCI preclinical in vitro and in vivo models and early clinical trials. Br J Cancer. 2001;84(10):1424–31.
7. Baker BM, Chen CS. Deconstructing the third dimension - how 3D culture microenvironments alter cellular cues. J Cell Sci. 2012;125(13):3015–24.
8. Yamada KM, Cukierman E. Modeling Tissue Morphogenesis and Cancer in 3D. Cell. 2007;130(4):601–10.

9. Cheon D-J, Orsulic S. Mouse Models of Cancer. Annu Rev Pathol Mech Dis. 2011;6(1):95–119.

10. Ruggeri BA, Camp F, Miknyoczki S. Animal models of disease: Pre-clinical animal models of cancer and their applications and utility in drug discovery. Biochem Pharmacol. 2014;87(1):150–61.

11. Sung KE, Beebe DJ. Microfluidic 3D models of cancer. Adv Drug Deliv Rev. 2014;79–80:68–78.

12. Tentler JJ, Tan AC, Weekes CD, Jimeno A, Leong S, Pitts TM, Arcaroli JJ, Messersmith WA, Eckhardt SG. Patient-derived tumour xenografts as models for oncology drug development. Nat Rev Clin Oncol. 2012;9:338–50.

13. Portillo-Lara R, Annabi N. Microengineered cancer-on-a-chip platforms to study the metastatic microenvironment. Lab Chip. 2016;16:4063–81.

14. Fan Y, Nguyen DT, Akay Y, Xu F, Akay M. Engineering a Brain Cancer Chip for High-throughput Drug Screening. Sci Rep. 2016;6:1–12.

15. Astolfi M, Péant B, Lateef MA, Rousset N, Kendall-Dupont J, Carmona E, Monet F, Saad F, Provencher D, Mes-Masson A-M, Gervais T. Micro-dissected tumor tissues on chip: an ex vivo method for drug testing and personalized therapy. Lab Chip. 2016;16(2):312–25.

16. Chen Y, Gao D, Liu H, Lin S, Jiang Y. Drug cytotoxicity and signaling pathway analysis with three-dimensional tumor spheroids in a microwell-based microfluidic chip for drug screening. Anal Chim Acta. 2015;898:85–92.

17. Kwapiszewska K, Michalczuk A, Rybka M, Kwapiszewski R, Brzózka Z. A microfluidic-based platform for tumour spheroid culture, monitoring and drug

screening. Lab Chip. 2014;14(12):2096–104.

18. Kim C, Bang JH, Kim YE, Lee SH, Kang JY. On-chip anticancer drug test of regular tumor spheroids formed in microwells by a distributive microchannel network. Lab Chip. 2012;12(20):4135.

19. Pandya HJ, Dhingra K, Prabhakar D, Chandrasekar V, Natarajan SK, Vasan AS, Kulkarni A, Shafiee H. A microfluidic platform for drug screening in a 3D cancer microenvironment. Biosens Bioelectron. 2017;94:632–42.

20. Phan DTT, Wang X, Craver BM, Sobrino A, Zhao D, Chen JC, Lee LYN, George SC, Lee AP, Hughes CCW. A vascularized and perfused organ-on-a-chip platform for large-scale drug screening applications. Lab Chip. 2017;17(3):511–20.

21. Kim C, Kasuya J, Jeon J, Chung S, Kamm RD. A quantitative microfluidic angiogenesis screen for studying anti-angiogenic therapeutic drugs. Lab Chip. 2015;15:301–10.

22. Hwang H, Park J, Shin C, Do Y, Cho YK. Three dimensional multicellular co-cultures and anti-cancer drug assays in rapid prototyped multilevel microfluidic devices. Biomed Microdevices. 2013;15(4):627–34.

23. Xu Z, Gao Y, Hao Y, Li E, Wang Y, Zhang J, Wang W, Gao Z, Wang Q. Application of a microfluidic chip-based 3D co-culture to test drug sensitivity for individualized treatment of lung cancer. Biomaterials. 2013;34(16):4109–17.

24. Jeong SY, Lee JH, Shin Y, Chung S, Kuh HJ. Co-culture of tumor spheroids and fibroblasts in a collagen matrix-incorporated microfluidic chip mimics

reciprocal activation in solid tumor microenvironment. PLoS One. 2016;11(7):1–17.

25. Wlodkowic D, Cooper JM. Tumors on chips: Oncology meets microfluidics. Curr Opin Chem Biol. 2010;14:556–67.

26. Tatosian DA, Shuler ML. A Novel System for Evaluation of Drug Mixtures for Potential Efficacy in Treating Multidrug Resistant Cancers. Biotechnol Bioeng. 2009;103:187–98.

27. Sung JH, Shuler ML. A micro cell culture analog (uCCA) with 3-D hydrogel culture of multiple cell lines to assess metabolism-dependent cytotoxicity of anti-cancer drugs. Lab Chip. 2009;9:1385–94.

28. Sung JH, Kam C, Shuler ML. A microfluidic device for a pharmacokinetic-pharmacodynamic (PK-PD) model on a chip. Lab Chip. 2010;10:446–55.

29. Hsu T-H, Kao Y-L, Lin W-L, Xiao J-L, Kuo P-L, Wu C-W, Liao W-Y, Lee C-H. The migration speed of cancer cells influenced by macrophages and myofibroblasts co-cultured in a microfluidic chip. Integr Biol. 2012;4(2):177–82.

30. Aung A, Theprungsirikul J, Lim HL, Varghese S. Chemotaxis-driven assembly of endothelial barrier in a tumor-on-a-chip platform. Lab Chip. 2016;16:1886–98.

31. Zervantonakis IK, Hughes-Alford SK, Charest JL, Condeelis JS, Gertler FB, Kamm RD. Three-dimensional microfluidic model for tumor cell intravasation and endothelial barrier function. Proc Natl Acad Sci. 2012;109(34):13515–20.

32. Ehsan SM, Welch-Reardon KM, Waterman ML, Hughes CCW, George SC. A

three-dimensional in vitro model of tumor cell intravasation. Integr Biol. 2014;6(6):603.

33. Lee H, Park W, Ryu H, Jeon NL. A microfluidic platform for quantitative analysis of cancer angiogenesis and intravasation. Biomicrofluidics. 2014;8(5):054102.

34. Shin MK, Kim SK, Jung H. Integration of intra- and extravasation in one cell-based microfluidic chip for the study of cancer metastasis. Lab Chip. 2011;11(22):3880.

35. Jeon JS, Bersini S, Gilardi M, Dubini G, Charest JL, Moretti M, Kamm RD, Jeon JS, Bersini S, Gilardi M, Dubini G, Charest JL, Moretti M, Kamm RD. Human 3D vascularized organotypic microfluidic assays to study breast cancer cell extravasation. Proc Natl Acad Sci. 2015;112(1):214–9.

36. Jeon JS, Zervantonakis IK, Chung S, Kamm RD, Charest JL. In Vitro Model of Tumor Cell Extravasation. PLoS One. 2013;8(2):e56910.

37. Chen MB, Whisler JA, Jeon JS, Kamm RD. Mechanisms of tumor cell extravasation in an in vitro microvascular network platform. Integr Biol. 2013;5:1262–71.

38. Chaw KC, Manimaran M, Tay EH, Swaminathan S. Multi-step microfluidic device for studying cancer metastasis. Lab Chip. 2007;7:1041–7.

39. Gilkes DM, Semenza GL, Wirtz D. Hypoxia and the extracellular matrix: drivers of tumour metastasis. Nat Rev Cancer. 2014 Jun;14(6):430–9.

40. Acosta MA, Jiang X, Huang P-K, Cutler KB, Grant CS, Walker GM, Gamcsik MP. A microfluidic device to study cancer metastasis under chronic and

intermittent hypoxia. Biomicrofluidics. 2014;8(5):054117.

41. Skardal A, Devarasetty M, Forsythe S, Atala A, Soker S. A reductionist metastasis-on-a-chip platform for in vitro tumor progression modeling and drug screening. Biotechnol Bioeng. 2016;113(9):2020–32.

42. Young EWK. Cells, tissues, and organs on chips: challenges and opportunities for the cancer tumor microenvironment. Integr Biol. 2013;5:1096–109.

43. Wan L, Skoko J, Yu J, Leduc PR, Neumann CA. Mimicking Embedded Vasculature Structure for 3D Cancer on a Chip Approaches through Micromilling. Sci Rep. 2017;7(1):1–8.

44. Boussommier-Calleja A, Li R, Chen MB, Wong SC, Kamm RD. Microfluidics: A new tool for modeling cancer-immune interactions. Trends Cancer. 2016;2(1):6–19.

45. Hirt C, Papadimitropoulos A, Mele V, Muraro MG, Mengus C, Iezzi G, Terracciano L, Martin I, Spagnoli GC. “In vitro” 3D models of tumor-immune system interaction. Adv Drug Deliv Rev. 2014;79:145–54.

46. Ruppen J, Wildhaber FD, Strub C, Hall SRR, Schmid RA, Geiser T, Guenat OT. Towards personalized medicine: chemosensitivity assays of patient lung cancer cell spheroids in a perfused microfluidic platform. Lab Chip. 2015;15(14):3076–85.

47. Balijepalli A, Sivaramakrishan V. Organs-on-chips: research and commercial perspectives. Drug Discov Today. 2016;22(2):397–403.

48. Ware BR, Khetani SR. Engineered Liver Platforms for Different Phases of Drug Development. Trends Biotechnol. 2017;35(2):172–83.

49. Clark AM, Wheeler SE, Taylor DP, Pillai VC, Young CL, Prantil-Baun R, Nguyen T, Stolz DB, Borenstein JT, Lauffenburger DA, Venkataramanan R, Griffith LG, Wells A. A microphysiological system model of therapy for liver micrometastases. Exp Biol Med. 2014;239(9):1170–9.

50. Prodanov L, Jindal R, Bale SS, Hegde M, McCarty WJ, Golberg I, Bhushan A, Yarmush ML, Usta OB. Long-term maintenance of a microfluidic 3D human liver sinusoid. Biotechnol Bioeng. 2016;113(1):241–6.

51. Kang YB (Abraham), Sodunke TR, Lamontagne J, Cirillo J, Rajiv C, Bouchard MJ, Noh M. Liver sinusoid on a chip: Long-term layered co-culture of primary rat hepatocytes and endothelial cells in microfluidic platforms. Biotechnol Bioeng. 2015;112(12):2571–82.

52. Lee J, Kim SH, Kim YC, Choi I, Sung JH. Fabrication and characterization of microfluidic liver-on-a-chip using microsomal enzymes. Enzyme Microb Technol. 2013;53(3):159–64.

53. Toh Y-C, Lim TC, Tai D, Xiao G, van Noort D, Yu H. A microfluidic 3D hepatocyte chip for drug toxicity testing. Lab Chip. 2009;9(14):2026.

54. Kim HJ, Li H, Collins JJ, Ingber DE. Contributions of microbiome and mechanical deformation to intestinal bacterial overgrowth and inflammation in a human gut-on-a-chip. Proc Natl Acad Sci. 2016;113:E7–15.

55. Shah P, Fritz J V, Glaab E, Desai MS, Greenhalgh K, Frachet A, Niegowska M, Estes M, Jäger C, Seguin-Devaux C, Zenhausern F, Wilmes P. A microfluidics-based in vitro model of the gastrointestinal human-microbe interface. Nat Commun. 2016;7:11535.

56. Chen Y, Lin Y, Davis KM, Wang Q, Rnjak-Kovacina J, Li C, Isberg RR, Kumamoto CA, Mecsas J, Kaplan DL. Robust bioengineered 3D functional human intestinal epithelium. Sci Rep. 2015;5:1–11.

57. Marsano A, Conficconi C, Lemme M, Occhetta P, Gaudiello E, Votta E, Cerino G, Redaelli A, Rasponi M. Beating heart on a chip: a novel microfluidic platform to generate functional 3D cardiac microtissues. Lab Chip. 2016;16(3):599–610.

58. Wang G, McCain ML, Yang L, He A, Pasqualini FS, Agarwal A, Yuan H, Jiang D, Zhang D, Zangi L, Geva J, Roberts AE, Ma Q, Ding J, Chen J, Wang DZ, Li K, Wang J, Wanders RJA, Kulik W, Vaz FM, Laflamme MA, Murry CE, Chien KR, Kelley RI, Church GM, Parker KK, Pu WT. Modeling the mitochondrial cardiomyopathy of Barth syndrome with induced pluripotent stem cell and heart-on-chip technologies. Nat Med. 2014;20(6):616–23.

59. Agarwal A, Goss JA, Cho A, McCain ML, Parker KK. Microfluidic heart on a chip for higher throughput pharmacological studies. Lab Chip. 2013;13(18):3599.

60. Wilmer MJ, Ng CP, Lanz HL, Vulto P, Suter-Dick L, Masereeuw R. Kidney-on-a-Chip Technology for Drug-Induced Nephrotoxicity Screening. Trends Biotechnol. 2016;34(2):156–70.

61. Jang K-J, Mehr AP, Hamilton GA, McPartlin LA, Chung S, Suh K-Y, Ingber DE. Human kidney proximal tubule-on-a-chip for drug transport and nephrotoxicity assessment. Integr Biol. 2013;5(9):1119.

62. Baudoin R, Griscom L, Monge M, Legallais C, Leclerc E. Development of a

renal microchip for in vitro distal tubule models. Biotechnol Prog. 2007;23(5):1245–53.

63. Wang YI, Abaci HE, Shuler ML. Microfluidic Blood–Brain Barrier Model Provides In Vivo-Like Barrier Properties for Drug Permeability Screening. Biotechnol Bioeng. 2017;114:184–94.

64. Park J, Lee BK, Jeong GS, Hyun JK, Lee CJ, Lee S-H. Three-dimensional brain-on-a-chip with an interstitial level of flow and its application as an in vitro model of Alzheimer's disease. Lab Chip. 2015;15(1):141–50.

65. Prabhakarpandian B, Shen M-C, Nichols JB, Mills IR, Sidoryk-Wegrzynowicz M, Aschner M, Pant K. SyM-BBB: a microfluidic blood brain barrier model. Lab Chip. 2013;13(6):1093.

66. Torisawa YS, Spina CS, Mammoto T, Mammoto A, Weaver JC, Tat T, Collins JJ, Ingber DE. Bone marrow-on-a-chip replicates hematopoietic niche physiology in vitro. Nat Methods. 2014;11(6):663–9.

67. Doryab A, Amoabediny G, Salehi-Najafabadi A. Advances in pulmonary therapy and drug development: Lung tissue engineering to lung-on-a-chip. Biotechnol Adv. 2016;34(5):588–96.

68. Huh D, Leslie DC, Matthews BD, Fraser JP, Jurek S, Hamilton GA, Thorneloe KS, Mcalexander MA, Ingber DE. A Human Disease Model of Drug Toxicity – Induced Pulmonary Edema in a Lung-on-a-Chip Microdevice. Sci Transl Med. 2012;4(159):1–9.

69. Huh D, Matthews BD, Mammoto A, Montoya-Zavala M, Hsin HY, Ingber DE. Reconstituting Organ-Level Lung Functions on a Chip. Science.

2010;328:1662–8.

70. Grosberg A, Nesmith AP, Goss JA, Brigham MD, McCain ML, Parker KK. Muscle on a chip: In vitro contractility assays for smooth and striated muscle. J Pharmacol Toxicol Methods. 2012;65(3):126–35.

71. Abaci HE, Gledhill K, Guo Z, Christiano AM, Shuler ML. Pumpless microfluidic platform for drug testing on human skin equivalents. Lab Chip. 2015;15:882–8.

72. Ataç B, Wagner I, Horland R, Lauster R, Marx U, Tonevitsky AG, Azar RP, Lindner G. Skin and hair on-a-chip: in vitro skin models versus ex vivo tissue maintenance with dynamic perfusion. Lab Chip. 2013;13(18):3555.

73. Oleaga C, Bernabini C, Smith AST, Srinivasan B, Jackson M, McLamb W, Platt V, Bridges R, Cai Y, Santhanam N, Berry B, Najjar S, Akanda N, Guo X, Martin C, Ekman G, Esch MB, Langer J, Ouedraogo G, Cotovio J, Breton L, Shuler ML, Hickman JJ. Multi-Organ toxicity demonstration in a functional human in vitro system composed of four organs. Sci Rep. 2016;6:20030.

74. Miller PG, Shuler ML. Design and demonstration of a pumpless 14 compartment microphysiological system. Biotechnol Bioeng. 2016;113(10):2213–27.

75. Esch MB, Ueno H, Applegate R, Shuler ML. Modular, pumpless body-on-a-chip platform for the co-culture of GI tract epthelium and 3D primary liver tissue. Lab Chip. 2016;16:2719–29.

76. Vernetti L, Gough A, Baetz N, Blutt S, Broughman JR, Brown JA, Foulke-Abel J, Hasan N, In J, Kelly E, Kovbasnjuk O, Repper J, Senutovitch N, Stabb J,

Yeung C, Zachos NC, Donowitz M, Estes M, Himmelfarb J, Truskey G, Wikswo JP, Taylor DL. Functional Coupling of Human Microphysiology Systems: Intestine, Liver, Kidney Proximal Tubule, Blood-Brain Barrier and Skeletal Muscle. Sci Rep. 2017;7:42296.

77. Maschmeyer I, Lorenz AK, Schimek K, Hasenberg T, Ramme AP, Hübner J, Lindner M, Drewell C, Bauer S, Thomas A, Sambo NS, Sonntag F, Lauster R, Marx U. A four-organ-chip for interconnected long-term co-culture of human intestine, liver, skin and kidney equivalents. Lab Chip. 2015;15(12):2688–99.

78. Zhang C, Zhao Z, Abdul Rahim NA, van Noort D, Yu H. Towards a human-on-chip: Culturing multiple cell types on a chip with compartmentalized microenvironments. Lab Chip. 2009;9(22):3185.

79. Shuler ML. Modeling Life. Ann Biomed Eng. 2012;40(7):1399–407.

80. Esch MB, Sung JH, Shuler ML. Promises, challenges and future directions of uCCAs. J Biotechnol. 2010;148:64–9.

81. Esch MB, King TL, Shuler ML. The Role of Body-on-a-Chip Devices in Drug and Toxicity Studies. Annu Rev Biomed Eng. 2011;13:55–72.

82. Bhatia SN, Ingber DE. Microfluidic organs-on-chips. Nat Biotechnol. 2014;32(8):760–72.

83. Esch MB, Smith AST, Prot J-M, Oleaga C, Hickman JJ, Shuler ML. How multi-organ microdevices can help foster drug development. Adv Drug Deliv Rev. 2014 Apr;69–70:158–69.

84. Wang YI, Carmona C, Hickman JJ, Shuler ML. Multiorgan Microphysiological Systems for Drug Development: Strategies, Advances, and Challenges. Adv

Healthc Mater. 2017;1701000:1701000.

85. Sweeney LM, Shuler ML, Babish JG, Ghanem A. A Cell Culture Analogue of Rodent Physiology: Application to Naphthalene Toxicology. Toxicol Vitr. 1995;9(3):307–16.

86. Ghanem A, Shuler ML. Characterization of a Perfusion Reactor Utilizing Mammalian Cells on Microcarrier Beads. Biotechnol Prog. 2000;16(3):471–9.

87. Ghanem A, Shuler ML. Combining Cell Culture Analogue Reactor Designs and PBPK Models to Probe Mechanisms of Naphthalene Toxicity. Biotechnol Prog. 2000;16(3):334–45.

88. Sin A, Chin KC, Jamil MF, Kostov Y, Rao G, Shuler ML. The Design and Fabrication of Three-Chamber Microscale Cell Culture Analog Devices with Integrated Dissolved Oxygen Sensors. Biotechnol Prog. 2004;20:338–45.

89. Viravaidya K, Sin A, Shuler ML. Development of a Microscale Cell Culture Analog To Probe Naphthalene Toxicity. Biotechnol Prog. 2004;20:316–23.

90. Viravaidya K, Shuler ML. Incorporation of 3T3-L1 Cells To Mimic Bioaccumulation in a Microscale Cell Culture Analog Device for Toxicity Studies. Biotechnol Prog. 2004;20:590–7.

91. Mahler GJ, Esch MB, Glahn RP, Shuler ML. Characterization of a Gastrointestinal Tract Microscale Cell Culture Analog Used to Predict Drug Toxicity. Biotechnol Bioeng. 2009;104(1):193–205.

92. Frey O, Misun PM, Fluri DA, Hengstler JG, Hierlemann A. Reconfigurable microfluidic hanging drop network for multi-tissue interaction and analysis. Nat Commun. 2014;5:4250.

93. Kim J-Y, Fluri DA, Marchan R, Boonen K, Mohanty S, Singh P, Hammad S, Landuyt B, Hengstler JG, Kelm JM, Hierlemann A, Frey O. 3D spherical microtissues and microfluidic technology for multi-tissue experiments and analysis. J Biotechnol. 2015;205:24–35.

94. Lee H, Kim DS, Ha SK, Choi I, Lee JM, Sung JH. A pumpless multi-organ-on-a-chip (MOC) combined with a pharmacokinetic-pharmacodynamic (PK-PD) model. Biotechnol Bioeng. 2016;114(2):432–43.

95. Materne EM, Ramme AP, Terrasso AP, Serra M, Alves PM, Brito C, Sakharov DA, Tonevitsky AG, Lauster R, Marx U. A multi-organ chip co-culture of neurospheres and liver equivalents for long-term substance testing. J Biotechnol. 2015;205:36–46.

96. Wagner I, Materne E-M, Brincker S, Süßbier U, Frädrich C, Busek M, Sonntag F, Sakharov DA, Trushkin E V, Tonevitsky AG, Lauster R, Marx U. A dynamic multi-organ-chip for long-term cultivation and substance testing proven by 3D human liver and skin tissue co-culture. Lab Chip. 2013;13(18):3538.

97. Kimura H, Ikeda T, Nakayama H, Sakai Y, Fujii T. An On-Chip Small Intestine–Liver Model for Pharmacokinetic Studies. J Lab Autom. 2015;20(3):265–73.

98. Ma L, Barker J, Zhou C, Li W, Zhang J, Lin B, Foltz G, Küblbeck J, Honkakoski P. Towards personalized medicine with a three-dimensional micro-scale perfusion-based two-chamber tissue model system. Biomaterials. 2012;33:4353–61.

99. Li Z, Jiang L, Zhu Y, Su W, Xu C, Tao T, Shi Y, Qin J. Assessment of hepatic metabolism-dependent nephrotoxicity on an organs-on-a-chip microdevice. Toxicol Vitr. 2018;46:1–8.

100. Choucha-Snouber L, Aninat C, Grsicom L, Madalinski G, Brochot C, Poleni PE, Razan F, Guillouzo CG, Legallais C, Corlu A, Leclerc E. Investigation of ifosfamide nephrotoxicity induced in a liver-kidney co-culture biochip. Biotechnol Bioeng. 2013;110(2):597–608.

101. Wang YI, Shuler ML. UniChip enables long-term recirculating unidirectional perfusion with gravity-driven flow for microphysiological systems. Lab Chip. 2018;18:2563–74.

102. Price PS, Conolly RB, Chaisson CF, Gross EA, Young JS, Mathis ET, Tedder DR. Modeling Interindividual Variation in Physiological Factors Used in PBPK Models of Humans. Crit Rev Toxicol. 2003;33(5):469–503.

103. Brown RP, Delp MD, Lindstedt SL, Rhomberg LR, Beliles RP. Physiological parameter values for physiologically based pharmacokinetic models. Toxicol Ind Health. 1997;13(4):407–84.

104. Forrester DW, Spence VA, Walker WF. The measurement of colonic mucosal-submucosal blood flow in man. J Physiol. 1980;299:1–11.

105. Bruus H. Governing Equations in Microfluidics. In: Laurell T, Lenshof A, editors. Microscale Acoustofluidics. Royal Society of Chemistry; 2015. p. 1–28.

106. Burkel B, Morris BA, Ponik SM, Riching KM, Eliceiri KW, Keely PJ. Preparation of 3D Collagen Gels and Microchannels for the Study of 3D

Interactions In Vivo. J Vis Exp. 2016;111:e53989.

107. Nebert DW, Dalton TP. The role of cytochrome P450 enzymes in endogenous signalling pathways and environmental carcinogenesis. Nat Rev Cancer. 2006;6(12):947–60.

108. Zanger UM, Schwab M. Cytochrome P450 enzymes in drug metabolism: Regulation of gene expression, enzyme activities, and impact of genetic variation. Pharmacol Ther. 2013;138(1):103–41.

109. Longley DB, Harkin DP, Johnston PG. 5-Fluorouracil: Mechanisms of Action and Clinical Strategies. Nat Rev Cancer. 2003;3:330–8.

110. Malet-Martino M, Martino R. Clinical Studies of Three Oral Prodrugs of 5-Fluorouracil (Capecitabine, UFT, S-1): A Review. Oncologist. 2002;7:288–323.

111. Fujii S, Kitano S, Ikenaka K, Shirasaka T. Effect of coadministration of uracil or cytosine on the anti-tumor activity of clinical doses of 1-(2-tetrahydrofuryl)-5-fluorouracil and level of 5-fluorouracil in rodents. Gann. 1979;70:209–14.

112. Toepke MW, Beebe DJ. PDMS absorption of small molecules and consequences in microfluidic applications. Lab Chip. 2006;6(12):1484–6.

113. Sung JH, Shuler ML. Prevention of air bubble formation in a microfluidic perfusion cell culture system using a microscale bubble trap. Biomed Microdevices. 2009;11:731–8.

114. Ota K, Taguchi T, Kimura K. Report on nationwide pooled data and cohort investigation in UFT phase II study. Cancer Chemother Pharmacol. 1988;22(4):333–8.

115. Takiuchi H, Ajani JA. Uracil-tegafur in gastric carcinoma: A comprehensive

review. J Clin Oncol. 1998;16(8):2877–85.

116. Tokyo Liver Cancer Chemotherapy Study Group. Phase II Study of Co-Administration of Uracil and Tegafur (UFT) in Hepatocellular Carcinoma. Jpn J Clin Oncol. 1985;15(3):559–62.

117. Fujii S, Ikenaka K, Fukushima M, Tetsuhiko S. Effect of uracil and its derivatives on antitumor activity 5-fluorouracil and 1-(2-tetrahydrofuryl)-5-fluorouracil. Gann. 1978;69(6):763–72.

118. Diasio RB, Harris BE. Clinical Pharmacology of 5-Fluorouracil. Clin Pharmacokinet. 1989;16:215–37.

119. Ikenaka K, Shirasaka T, Kitano S, Fujii S. Effect of uracil on the metabolism of 5-fluorouracil in vitro. Gann. 1979;70:353–9.

120. van Kuilenburg ABP. Dihydropyrimidine dehydrogenase and the efficacy and toxicity of 5-fluorouracil. Eur J Cancer. 2004;40(7):939–50.

121. Ham SL, Joshi R, Thakuri PS, Tavana H. Liquid-based three-dimensional tumor models for cancer research and drug discovery. Exp Biol Med. 2016;241(9):939–54.

122. Nath S, Devi GR. Three-dimensional culture systems in cancer research: Focus on tumor spheroid model. Pharmacol Ther. 2016;163:94–108.

123. Curcio E, Salerno S, Barbieri G, De Bartolo L, Drioli E, Bader A. Mass transfer and metabolic reactions in hepatocyte spheroids cultured in rotating wall gas-permeable membrane system. Biomaterials. 2007;28(36):5487–97.

124. Mehta G, Hsiao AY, Ingram M, Luker GD, Takayama S. Opportunities and challenges for use of tumor spheroids as models to test drug delivery and

efficacy. J Control Release. 2012;164(2):192–204.

125. Reynolds DS, Tevis KM, Blessing WA, Colson YL, Zaman MH, Grinstaff MW. Breast Cancer Spheroids Reveal a Differential Cancer Stem Cell Response to Chemotherapeutic Treatment. Sci Rep. 2017;7:10382.

126. Knuchel R, Hofstadter F, Jenkins WEA, Masters JRW. Sensitivities of Monolayers and Spheroids of the Human Bladder Cancer Cell Line MGH-U1 to the Drugs Used for Intravesical Chemotherapy. Cancer Res. 1989;49(6):1397–401.

127. Kerr DJ, Wheldon TE, Hydns S, Kaye SB. Cytotoxic drug penetration studies in multicellular tumour spheroids. Xenobiotica. 1988;18(6):641–8.

128. Kwok TT, Twentyman PR. The response to cytotoxic drugs of EMT6 cells treated either as intact or disaggregated spheroids. Br J Cancer. 1985;51(2):211–8.

129. Wibe E. Resistance to vincristine of human cells grown as multicellular spheroids. Br J Cancer. 1980;42(6):937–41.

130. Frieboes HB, Edgerton ME, Fruehauf JP, Rose FRAJ, Worrall LK, Gatenby RA, Ferrari M, Cristini V. Prediction of drug response in breast cancer using integrative experimental/computational modeling. Cancer Res. 2009;69(10):4484–92.

131. Ward JP, King JR. Mathematical modelling of drug transport in tumour multicell spheroids and monolayer cultures. Math Biosci. 2003;181(2):177–207.

132. Jang SH, Wientjes MG, Lu D, Au JL-S. Drug Delivery and Transport to Solid

Tumors. Pharm Res. 2003;20(9):1337–50.

133. Minchinton AI, Tannock IF. Drug penetration in solid tumours. Nat Rev Cancer. 2006;6(8):583–92.

134. Gamelin E, Boisdron-Celle M. Dose monitoring of 5-fluorouracil in patients with colorectal or head and neck cancer-status of the art. Crit Rev Oncol Hematol. 1999;30(1):71–9.

135. Spicer D V, Ardalan B, Daniels JR, Silberman H, Johnson K. Reevaluation of the Maximum Tolerated Dose of Continuous Venous Infusion of 5-Fluorouracil with Pharmacokinetics. Cancer Res. 1988;48(2):459–61.

136. Wilkening S, Stahl F, Bader A. Comparison of Primary Human Hepatocytles and Hepatoma Cell Line HepG2 with Regard to Their Biotransformation Properties. Drug Metab Dispos. 2003;31(8):1035–42.

137. Williamson A, Singh S, Fernekorn U, Schober A. The future of the patient-specific Body-on-a-chip. Lab Chip. 2013;13(18):3471–80.

138. Gustavsson B, Carlsson G, MacHover D, Petrelli N, Roth A, Schmoll HJ, Tveit KM, Gibson F. A review of the evolution of systemic chemotherapy in the management of colorectal cancer. Clin Colorectal Cancer. 2015;14:1–10.

139. Pazdur R, Lassere Y, Rhodes V, Ajani JA, Sugarman SM, Patt YZ, Jones Jr D V, Markowitz AB, Abbruzzese JL, Bready B. Phase II trial of uracil and tegafur plus oral leucovorin: An effective oral regimen in the treatment of metastatic colorectal carcinoma. J Clin Oncol. 1994;12(11):2296–300.

140. Douillard JY, Cunningham D, Roth AD, Navarro M, James RD, Karasek P, Jandik P, Iveson T, Carmichael J, Alakl M, Gruia G, Awad L, Rougier P.

Irinotecan combined with fluorouracil compared with fluorouracil alone as first-line treatment for metastatic colorectal cancer: a multicentre randomised trial. Lancet. 2000;355:1041–7.

141. Goldberg RM, Sargent DJ, Morton RF, Fuchs CS, Ramanathan RK, Williamson SK, Findlay BP, Pitot HC, Alberts SR. A randomized controlled trial of fluorouracil plus leucovorin, irinotecan, and oxaliplatin combinations in patients with previously untreated metastatic colorectal cancer. J Clin Oncol. 2004;22(1):23–30.

142. Zhang B, Radisic M. Organ-on-a-chip devices advance to market. Lab Chip. 2017;17(14):2395–420.

CHAPTER 4

CONCLUSIONS AND FUTURE DIRECTIONS

4.1 Conclusions

The tumor microenvironment, comprised of genetically mutated cancer cells, tumor-associated stromal cells, soluble signals, and extracellular matrix (ECM), collectively contributes to cancer initiation, progression, and treatment. In a feedback system, biochemical and mechanical cues in the tumor microenvironment influence the behavior of both the cancer cells and tumor-associated stromal cells, which, reciprocally alters the biochemical and mechanical cues. With this complexity in mind, the work within this dissertation seeks to advance cancer understanding and treatment. Since many of the molecular mechanisms contributing to cancer remain poorly understood, it is imperative to assess endothelial cell (EC) behavior when complex stimuli are present, namely matrix stiffness and vascular endothelial growth factor (VEGF) stimulation, which were probed to understand how biochemical and biophysical cues influence the cancer niche both alone and in concert with one other (Chapter 2). While furthering our understanding of the cancer microenvironment is essential to treatment, it is also crucial that our continually evolving understanding of the cancer microenvironment is translated to clinically-relevant models. Taking this into account, I constructed a human-based mimetic capable of recapitulating chemotherapeutic-induced cytotoxicity within

colon cancer cells (Chapter 3). Altogether, this work may reveal new drug targets to combat tumor angiogenesis and translate these findings to generate a drug screening model to further test such therapeutic targets for responses to various chemotherapeutics.

In Chapter 2, I investigated the downstream effects of simultaneous activation of molecular pathways implicated for tumor angiogenesis. Specifically, matrix stiffening is known to occur during cancer development [1,2] and is conveyed through crosstalk between integrins and the Rho/ROCK pathway [3]. Additionally, elevated VEGF production is reported in cancer patients [4,5] and plays a key role in VEGF receptor-2 (VEGFR-2)-mediated tumor angiogenesis [6]. While probing both mechanics and signaling, my data indicate altered VEGF receptor trafficking, intracellular signaling, and proliferation within ECs when both stimuli were present. In particular, cells cultured on compliant substrates experienced increased VEGFR-2 expression and clustering, but stiffer matrices fostered its internalization. Further, increased ECM stiffness elevated VEGF-stimulated ERK 1/2 phosphorylation and downstream cell proliferation. In addition, ECs cultured on stiff substrates and subjected to VEGF stimulation demonstrated robust actin stress fiber formation to a higher degree than when either stimuli were present alone. Altogether, these data demonstrate complex crosstalk between matrix stiffness and VEGF signaling pathways.

Interestingly, the concerted effects of ECM stiffness and VEGF noted above were sensitive to cell confluency. The stiffness-mediated differential responses in

VEGFR-2 levels and ERK 1/2 phosphorylation following VEGF treatment were demonstrated in sub-confluent ECs only, but once the cells reached confluence, these effects were no longer observed. The relationship between VEGFR-2 and vascular endothelial (VE)-cadherin has been extensively studied and shows VE-cadherin association with VEGFR-2 upon monolayer confluence to downregulate its activation and intracellular signaling mechanisms [7,8]. Therefore, this suggests that the combined effort of matrix stiffening and VEGF could not overcome VE-cadherin regulation of VEGFR-2 in the system.

With a more translational approach to advancing cancer treatment, I designed and tested a body-on-a-chip microfluidic platform for chemotherapeutic drug screening. The novel three-chamber micro cell culture analog (μCCA) features gravity-driven, pumpless flow following physiologically-relevant blood circulatory patterns to organ compartments representing colon tumor, liver, and bone marrow tissue. With this device it is possible to achieve unidirectional flow which is particularly important for EC biology [9]. Additionally, the microphysiological system (MPS) was challenged with Tegafur administration and successfully demonstrated its conversion to active 5-FU metabolites. The combined Tegafur-uracil (UFT) treatment was more effective than either component administered alone. Further, UFT therapy induced toxicity within HCT-116 colon cancer cells, but the cytotoxic effect was significantly reduced when cancer cells were cultured within multicellular spheroids compared to a single cell suspension, presumably due to diffusion-limited drug penetration. Compared to static controls, the presence of flow within the μCCA enhanced UFT-induced cytotoxicity by

increasing the circulation of metabolites to each organ chamber. Moreover, my device detected off-target toxicity within the bone marrow cells upon UFT treatment. Collectively, the human-based body-on-a-chip platform aims to support current preclinical models for cancer drug development by testing for both efficacy and toxicity of the drug compound.

Importantly, this μCCA is the first demonstration of pumpless, unidirectional perfusion to multiple channels simultaneously. Recently, our lab designed a microfluidic device to yield fluid flow in a unidirectional manner through the establishment of an air-liquid interface in the medium reservoir to dictate the direction of flow through a central channel [9]. Using the same design principles, this μCCA promotes unidirectional flow to multiple central channels located directly above the tumor, liver, and bone marrow chambers. Notably, this unidirectional design is a better representation of *in vivo* blood circulation patterns compared to platforms using pumpless, bidirectional flow between medium reservoirs. Additionally, unidirectional perfusion promoted authentic endothelial behaviors, including cell alignment in the direction of flow, F-actin realignment, and reduced cell proliferation, that were not observed under bidirectional flow [9]. Therefore, future studies could incorporate ECs into the three-chamber μCCA with unidirectional flow to investigate anti-cancer therapeutics with relevant EC biology.

In summary, the data presented within this dissertation aim to expand our comprehensive knowledge of cancer biology and treatment strategies. The successful

development of novel cancer therapeutics will require approaches from multiple perspectives within the realms of both basic science and translational research.

4.2 Future Directions

The research presented in this dissertation investigates the influence of factors within the tumor microenvironment that emerge from cancer-associated stromal cells and ECM on tumor angiogenesis and chemotherapeutic toxicity. This work aims to improve cancer treatment by expanding our current knowledge of mechanical mechanisms contributing to cancer progression and create physiologically-relevant models to screen anti-cancer therapeutics. Future experiments will build upon these findings.

Chemical and Mechanical Regulation of Tumor Angiogenesis

In Chapter 2, I investigated the combined effect of VEGF signaling and matrix stiffening on specific endothelial responses. Within the 2D experimental setup, I observed significant changes in intracellular signaling, cell proliferation, and actin stress formation when both biophysical and biochemical stimuli were present. Previously, research within the Reinhart-King lab revealed that ECM stiffening resulted in enhanced blood vessel growth and impaired vessel integrity in 2D, 3D, *in vivo*, and *ex ovo* models [10]. Since the present data highlights the importance of simultaneous VEGF and increased matrix stiffness stimuli in 2D, it is essential to investigate how this translates to both 3D and *in vivo* environments. Importantly, blood flow also contributes to

numerous endothelial behaviors *in vivo* [11,12], and previous work in the Shuler lab demonstrated that unidirectional, but not bidirectional, fluid flow recapitulated specific EC responses observed in the body [9]. Thus, increasing the complexity of the experimental system, for example, by increasing the dimensionality and adding fluid perfusion, will better recapitulate the native environment of ECs within the human body, but it will also make it more difficult to delineate the contributions from each individual factor. Furthermore, this work may reveal situations where one stimulus may dominate the outcome.

In addition to reproducing this work in more physiological systems, it is important to utilize relevant cell sources to produce authentic endothelial behaviors. One potential source is ECs isolated from *ex vivo* murine models, such as those isolated from MMTV-PyMT tumor tissue in Appendix B. Furthermore, the effect of matrix stiffness can be investigated by treating the mice with a lysyl oxidase inhibitor such as β-aminopropionitrile (BAPN) to inhibit collagen cross-linking and reduce tissue stiffness [13]. The addition of VEGF to ECs derived from healthy or BAPN-treated mice would reveal the influence of such chemical and mechanical factors on vascular behaviors. This cell source could serve as a physiologically-relevant model to begin to isolate the effects found in Chapter 2 on cells that have been chronically exposed to different biophysical niches.

Since my work and the work of others have demonstrated the significance of VEGF in promoting multiple aspects of angiogenesis during cancer [14–17], VEGF

emerges as a natural target for developing anti-angiogenic therapeutics. Although targeting VEGF can temporarily curb tumor angiogenesis, patients often develop resistance to anti-VEGF therapeutics in the clinic [18,19]. This resistance is often attributed to the upregulation or activation of alternative pro-angiogenic pathways [18]. Like VEGF, several of these other chemical stimuli share many of the same intracellular molecules as those implicated in the Rho/ROCK pathway activated by matrix stiffening [3]. As such, future studies should investigate the dynamic relationship between other pro-angiogenic factors and ECM stiffness to aid in the development of alternative therapeutics to combat tumor angiogenic behaviors.

In addition to the therapeutic targets described above, one additional chemical target worthy of further investigation is the ECM protein fibronectin (Fn). In addition to elevated VEGF expression during cancer progression [4,5], increased production of Fn is reported in cancer patients and correlates with the degree of malignancy [20–22]. Fn is a mechanotransducer; in cancer, the molecule is known to adapt an unfolded conformation, which reveals cryptic binding sites such as those for VEGF, and can modify integrin activity [23]. Furthermore, matrix stiffening is known to enhance Fn unfolding, creating a feed-forward cascade for tumor progression [23]. Moreover, previous work from our lab [24] and my preliminary data in Appendix A further demonstrate connections between ECM stiffness and Fn. Specifically, my data indicates that EC permeability was increased when cells were cultured on stiff, fibronectin-coated matrices compared to those on stiff, collagen-coated substrates. This suggests crosstalk between the intracellular signaling pathways activated by matrix stiffness and Fn stimuli

resulting in an additive phenotypic effect. These findings warrant further attention towards the molecular mechanisms involved in this complex relationship.

Current Limitations of Body-on-a-Chip Platforms

Along with advancing the development of anti-angiogenic therapeutics, the work within this dissertation also strives to improve current screening modalities for cancer drug development. In Chapter 3, I designed a body-on-a-chip device for testing chemotherapeutics to predict toxicity to the desired tumor target and undesired side effects in other organs. While body-on-a-chip technology better recapitulates the dynamic environment of the body compared to traditional 2D or 3D *in vitro* preclinical models and is more humanized than animal models [25,26], it does require further improvement to resolve its current limitations, such as a limited range of available cell sources and device materials.

As with many experiments, there is always a balance to consider when selecting which cells to utilize within microfluidic chips. The cost and availability of cell sources is constantly balanced with the ability for reproducible scientific results and the authenticity of those results to mimic *in vivo* cellular behavior. This study (Chapter 3), like many others, utilized immortalized cell lines, which boast a low cost, highly available, easy to culture *in vitro* cell source. However, repeated passaging often results in genotypic and phenotypic changes to the cells [27]. Alternatively, primary cells obtained from human or animal tissue are cultured as representative organ models within microfluidic devices. While primary tissue is directly derived from the organ

source it is intending to represent and can include all cell types and ECM relevant to that organ, cells are often recovered in limited numbers and it can be difficult to maintain their phenotype once they are removed from their native tissue [28]. Recently, induced pluripotent stem cells (iPSCs) have become increasingly popular for *in vitro* use. iPSCs are a self-renewing cell source derived from human somatic cells, which can provide a near limitless supply of cells compared to primary cells [29], and these cells have recently been implemented in human disease models [30]. Thus, the use of iPSCs in body-on-a-chip offers the possibility to create human surrogates using patient-derived cells to predict drug efficacy and toxicity within genetically-similar groups of people [31]. Currently, iPSC technology cannot yield mature phenotypes of all types of cells [32], but as the technology evolves it will be possible to develop increasingly authentic organ mimetics. Overall, regardless of cell source, it is vital to reproduce authentic cell behavior within body-on-a-chip devices to accurately predict human responses to drug candidates to optimize drug screening capabilities.

Another current constraint within body-on-a-chip systems is the limited supply of materials that enable easy, highly reproducible fabrication of microfluidic devices. Traditionally, polydimethylsiloxane (PDMS) has been used for prototype devices due to its optical transparency and ease for patterning complex device features in a rapid fashion [33]. However, the porous, network structure of PDMS enables high gas permeability, promoting extensive medium evaporation and absorption of small molecules into the bulk structure [34]. Altogether, PDMS-containing microfluidic devices may significantly skew the results of drug screening experiments.

To avoid PDMS, the μCCA developed in Chapter 3 consisted of alternating poly(methyl methacrylate) (PMMA) and silicone layers. Like PDMS, silicone can also absorb small molecules and influence drug testing data. However, in our system only a minimal surface area of silicone was exposed to the medium to minimize the amount of drug absorption. In the future, new materials need to be developed to better resist drug adsorption altogether. Although not yet widely adopted, new materials such as styrene-ethylene/butylene-styrene, and polyurethane elastomers [35,36] are being developed for use in organ-on-a-chip systems to minimize the above stated limitations.

In addition to improved cell sources and materials, body-on-a-chip technology would benefit greatly from addressing other current limitations, including minimal multiplexing, limited scalability, and intensive validation of devices [37]. On-chip micropumps [38,39], gravity-driven pumpless operation [40], 3D printing techniques [41], and even industrial collaborations to foster higher efficiency [42] may provide possible avenues to alleviate some of these issues.

Anti-Angiogenic Drug Testing Within a Body-on-a-Chip Device

In this dissertation, the data presented in Chapter 2 highlights the importance of tumor-associated microenvironmental cues on angiogenesis and a physiologically-relevant cancer drug screening model was designed in Chapter 3. Altogether, this implies that body-on-a-chip devices could be useful for developing and testing therapeutics to combat tumor angiogenesis, a potential research avenue that has not yet been explored.

Previously, many others have sought to study the complex tumor-endothelial cell interactions that contribute to cancer progression. Traditional 3D culture platforms including Transwells, hydrogel systems, and tumor spheroids, have been used to study how co-culture influences intracellular signaling [43,44], cell morphology [45,46], migration and invasion [43,45,47–49], and proliferation [46,48,50] of both cell types. Furthermore, tumor cells can stimulate ECs to form capillary-like network structures [43,44,46–48]. Although these models promote cell-cell interactions, they cannot accurately recapitulate the complex architectures and dynamic microenvironment found within tumors *in vivo* [51].

Recently, more physiologically-relevant models of tumor angiogenesis that include fluid perfusion have been designed. In particular, Kim et al. [52] designed a device to screen anti-angiogenic compounds. Their three-channel device contained a blood vessel-mimetic where ECs are exposed to drug-supplemented medium, a center collagen gel as an ECM-mimic, and a tumor-mimic channel containing VEGF-supplemented medium. Pro-angiogenic, chemotactic signaling stimulates ECs to sprout into the collagen gel, and the effectiveness of the anti-angiogenic therapeutic dictates the extent of endothelial sprouting. Additionally, other 3D microfluidic models to investigate endothelial morphology and sprouting have been established [53–60]. Importantly, these models better mimic the intricate geometry of blood vessels within tumors *in vivo*. However, such models are limited by complex fabrication methods (e.g. multi-step hydrogel polymerization and assembly) [54,57,60], but ultimately could be incorporated into body-on-a-chip technology.

Thus, in a modified approach, a body-on-a-chip platform to simultaneously investigate tumor angiogenesis and organ-organ interactions would provide useful assessment of metabolism- and toxicity-mediated effects on a variety of cell types. To complete this work, the μCCA would include a tumor compartment, along with additional representative organs, such as the liver to mimic drug metabolism and a marker for off-target toxicity to sensitive cells like those within bone marrow. Since many clinical cancer treatment regimens include the combination of chemotherapeutics and anti-angiogenic compounds [61], this device could potentially investigate both monotherapy and clinically-relevant therapeutic combinations. It could also be used to optimize the timing and dosing schedules for new and existing combination regimens and predict harmful drug-drug interactions. Moreover, the influence of tumor-specific factors on therapeutic efficacy and toxicity could be investigated and may reveal novel targets to combat cancer-associated angiogenesis.

REFERENCES

1. Levental KR, Yu H, Kass L, Lakins JN, Egeblad M, Erler JT, Fong SFT, Csiszar K, Giaccia A, Weninger W, Yamauchi M, Gasser DL, Weaver VM. Matrix crosslinking forces tumor progression by enhancing integrin signaling. Cell. 2009;139:891–906.
2. Lopez JI, Kang I, You W-K, McDonald DM, Weaver VM. In situ force mapping of mammary gland transformation. Integr Biol. 2011;3:910–21.
3. Huveneers S, Danen EHJ. Adhesion signaling - crosstalk between integrins, Src and Rho. J Cell Sci. 2009;122:1059–69.
4. Takahashi Y, Kitadai Y, Bucana CD, Cleary KR, Ellis LM. Expression of vascular endothelial growth factor and its receptor, KDR, correlates with vascularity, metastasis, and proliferation of human colon cancer. Cancer Res. 1995;55:3964–8.
5. Ferrara N, Davis-Smyth T. The biology of vascular endothelial growth factor. Endocr Rev. 1997;18(1):4–25.
6. Carmeliet P, Jain RK. Angiogenesis in cancer and other diseases. Nature. 2000;407:249–57.
7. Lampugnani MG, Zanetti A, Corada M, Takahashi T, Balconi G, Breviario F, Orsenigo F, Cattelino A, Kemler R, Daniel TO, Dejana E. Contact inhibition of VEGF-induced proliferation requires vascular endothelial cadherin, B-catenin, and the phosphatase DEP-1/CD148. J Cell Biol. 2003;161(4):793–804.
8. Lampugnani MG, Orsenigo F, Gagliani MC, Tacchetti C, Dejana E. Vascular endothelial cadherin controls VEGFR-2 internalization and signaling from

intracellular compartments. J Cell Biol. 2006;174(4):593–604.

9. Wang YI, Shuler ML. UniChip enables long-term recirculating unidirectional perfusion with gravity-driven flow for microphysiological systems. Lab Chip. 2018;18:2563–74.

10. Bordeleau F, Mason BN, Lollis EM, Mazzola MC, Zanotelli MR, Somasegar S, Califano JP, Montague CR, LaValley DJ, Huynh J, Negrón Abril YL, Bonassar LJ, Butcher JT, Weiss RS, Reinhart-King CA. Matrix stiffening promotes a tumor vasculature phenotype. Proc Natl Acad Sci. 2016;114(3):492–7.

11. Baratchi S, Khoshmanesh K, Woodman OL, Potocnik S, Peter K, McIntyre P. Molecular Sensors of Blood Flow in Endothelial Cells. Trends Mol Med. 2017;23(9):850–68.

12. Tarbell JM. Shear stress and the endothelial transport barrier. Cardiovasc Res. 2010;87(2):320–30.

13. Xiao Q, Ge G. Lysyl oxidase, extracellular matrix remodeling and cancer metastasis. Cancer Microenviron. 2012;5:261–73.

14. Papetti M, Herman IM. Mechanisms of normal and tumor-derived angiogenesis. Am J Cell Physiol. 2002;282:C947–70.

15. Hutchings H, Ortega N, Plouet J. Extracellular matrix-bound vascular endothelial growth factor promotes endothelial cell adhesion, migration, and survival through integrin ligation. FASEB J. 2003;17:1520–2.

16. Kroll J, Waltenberger J. The vascular endothelial growth factor receptor KDR activates multiple signal transduction pathways in porcine aortic endothelial cells. J Biol Chem. 1997;272(51):32521–7.

17. Bryan BA, Dennstedt E, Mitchell DC, Walshe TE, Noma K, Loureiro R, Saint-Geniez M, Campaigniac J-P, Liao JK, D'Amore PA. RhoA/ROCK signaling is essential for multiple aspects of VEGF-mediated angiogenesis. FASEB J. 2010;24:3186–95.

18. Bergers G, Hanahan D. Modes of resistance to anti-angiogenic therapy. Nat Rev Cancer. 2008;8:592–603.

19. Ferrara N. Pathways mediating VEGF-independent tumor angiogenesis. Cytokine Growth Factor Rev. 2010;21(1):21–6.

20. D'Ardenne AJ, McGee JO. Fibronectin in disease. J Pathol. 1984;142:235–51.

21. Bae YK, Kim A, Kim MK, Choi JE, Kang SH, Lee SJ. Fibronectin expression in carcinoma cells correlates with tumor aggressiveness and poor clinical outcome in patients with invasive breast cancer. Hum Pathol. 2013;44(10):2028–37.

22. Fernandez-Garcia B, Eiró N, Marín L, González-Reyes S, González LO, Lamelas ML, Vizoso FJ. Expression and prognostic significance of fibronectin and matrix metalloproteases in breast cancer metastasis. Histopathology. 2014;64(4):512–22.

23. Wang K, Seo BR, Fischbach C, Gourdon D. Fibronectin Mechanobiology Regulates Tumorigenesis. Cell Mol Bioeng. 2016;9(1):1–11.

24. Bordeleau F, Califano JP, Abril YLN, Mason BN, LaValley DJ, Shin SJ, Weiss RS, Reinhart-King CA. Tissue stiffness regulates serine/arginine-rich protein-mediated splicing of the extra domain B-fibronectin isoform in tumors. Proc Natl Acad Sci. 2015;112(27):8314–9.

25. Esch MB, King TL, Shuler ML. The Role of Body-on-a-Chip Devices in Drug and Toxicity Studies. Annu Rev Biomed Eng. 2011;13:55–72.

26. Wang YI, Carmona C, Hickman JJ, Shuler ML. Multiorgan Microphysiological Systems for Drug Development: Strategies, Advances, and Challenges. Adv Healthc Mater. 2017;1701000:1701000.

27. Pan C, Kumar C, Bohl S, Klingmueller U, Mann M. Comparative Proteomic Phenotyping of Cell Lines and Primary Cells to Assess Preservation of Cell Type-specific Functions. Mol Cell Proteomics. 2009;8(3):443–50.

28. Unger RE, Krump-Konvalinkova V, Peters K, Kirkpatrick CJ. In vitro expression of the endothelial phenotype: Comparative study of primary isolated cells and cell lines, including the novel cell line HPMEC-ST1.6R. Microvasc Res. 2002;64(3):384–97.

29. Malik N, Rao MS. A review of the methods for human iPSC derivation. Methods Mol Biol. 2013;997:23–33.

30. Tiscornia G, Vivas EL, Belmonte JCI. Diseases in a dish: Modeling human genetic disorders using induced pluripotent cells. Nat Med. 2011;17(12):1570–6.

31. Wang YI, Oleaga C, Long CJ, Esch MB, McAleer CW, Miller PG, Hickman JJ, Shuler ML. Self-contained, low-cost Body-on-a-Chip systems for drug development. Exp Biol Med. 2017;242:1701–13.

32. Lee G, Studer L. Induced pluripotent stem cell technology for the study of human disease. Nat Methods. 2010;7(1):25–7.

33. Sia SK, Whitesides GM. Microfluidic devices fabricated in

poly(dimethylsiloxane) for biological studies. Electrophoresis. 2003;24(21):3563–76.

34. Toepke MW, Beebe DJ. PDMS absorption of small molecules and consequences in microfluidic applications. Lab Chip. 2006;6(12):1484–6.

35. Borysiak MD, Yuferova E, Posner JD. Simple, low-cost styrene-ethylene/butylene-styrene microdevices for electrokinetic applications. Anal Chem. 2013;85(24):11700–4.

36. Domansky K, Leslie DC, McKinney J, Fraser JP, Sliz JD, Hamkins-Indik T, Hamilton GA, Bahinski A, Ingber DE. Clear castable polyurethane elastomer for fabrication of microfluidic devices. Lab Chip. 2013;13(19):3956–64.

37. Zhang B, Korolj A, Lai BFL, Radisic M. Advances in organ-on-a-chip engineering. Nat Rev Mater. 2018;3(8):257–78.

38. Maschmeyer I, Lorenz AK, Schimek K, Hasenberg T, Ramme AP, Hübner J, Lindner M, Drewell C, Bauer S, Thomas A, Sambo NS, Sonntag F, Lauster R, Marx U. A four-organ-chip for interconnected long-term co-culture of human intestine, liver, skin and kidney equivalents. Lab Chip. 2015;15(12):2688–99.

39. Schimek K, Busek M, Brincker S, Groth B, Hoffmann S, Lauster R, Lindner G, Lorenz A, Menzel U, Sonntag F, Walles H, Marx U, Horland R. Integrating biological vasculature into a multi-organ-chip microsystem. Lab Chip. 2013;13(18):3588.

40. Sung JH, Kam C, Shuler ML. A microfluidic device for a pharmacokinetic-pharmacodynamic (PK-PD) model on a chip. Lab Chip. 2010;10:446–55.

41. Murphy S V, Atala A. 3D bioprinting of tissues and organs. Nat Biotechnol.

2014;32(8):773–85.

42. Zhang B, Radisic M. Organ-on-a-chip devices advance to market. Lab Chip. 2017;17(14):2395–420.

43. Khodarev NN, Yu J, Labay E, Darga T, Brown CK, Mauceri HJ, Yassari R, Gupta N, Weichselbaum RR. Tumour-endothelium interactions in co-culture: coordinated changes of gene expression profiles and phenotypic properties of endothelial cells. J Cell Sci. 2003;116(6):1013–22.

44. Chiew GGY, Wei N, Sultania S, Lim S, Luo KQ. Bioengineered three-dimensional co-culture of cancer cells and endothelial cells: A model system for dual analysis of tumor growth and angiogenesis. Biotechnol Bioeng. 2017;26297.

45. Cross VL, Zheng Y, Won Choi N, Verbridge SS, Sutermaster BA, Bonassar LJ, Fischbach C, Stroock AD. Dense type I collagen matrices that support cellular remodeling and microfabrication for studies of tumor angiogenesis and vasculogenesis in vitro. Biomaterials. 2010;31(33):8596–607.

46. Szot CS, Buchanan CF, Freeman JW, Rylander MN. In Vitro Angiogenesis Induced by Tumor-Endothelial Cell Co-Culture in Bilayered, Collagen I Hydrogel Bioengineered Tumors. Tissue Eng Part C Methods. 2013;19(11):864–74.

47. Timmins N, Dietmair S, Nielsen L. Hanging-drop multicellular spheroids as a model of tumour angiogenesis. Angiogenesis. 2004;7:97–103.

48. Chen Y, Gou X, Ke X, Cui H, Chen Z. Human tumor cells induce angiogenesis through positive feedback between CD147 and insulin-like growth factor-I.

PLoS One. 2012;7(7):e40965.

49. Patra B, Peng Y-S, Peng C-C, Liao W-H, Chen Y-A, Lin K-H, Tung Y-C, Lee C-H. Migration and vascular lumen formation of endothelial cells in cancer cell spheroids of various sizes. Biomicrofluidics. 2014;8:052109.

50. Ingthorsson S, Sigurdsson V, Fridriksdottir AJR, Jonasson JG, Kjartansson J, Magnusson MK, Gudjonsson T. Endothelial cells stimulate growth of normal and cancerous breast epithelial cells in 3D culture. BMC Res Notes. 2010;3:184.

51. Sung KE, Beebe DJ. Microfluidic 3D models of cancer. Adv Drug Deliv Rev. 2014;79–80:68–78.

52. Kim C, Kasuya J, Jeon J, Chung S, Kamm RD. A quantitative microfluidic angiogenesis screen for studying anti-angiogenic therapeutic drugs. Lab Chip. 2015;15:301–10.

53. Chung S, Sudo R, Mack PJ, Wan C-R, Vickerman V, Kamm RD. Cell migration into scaffolds under co-culture conditions in a microfluidic platform. Lab Chip. 2009;9:269–75.

54. Zheng Y, Chen J, Craven M, Choi NW, Totorica S, Diaz-Santana A, Kermani P, Hempstead B, Fischbach-Teschl C, Lopez JA, Stroock AD. In vitro microvessels for the study of angiogenesis and thrombosis. Proc Natl Acad Sci. 2012;109(24):9342–7.

55. Zervantonakis IK, Hughes-Alford SK, Charest JL, Condeelis JS, Gertler FB, Kamm RD. Three-dimensional microfluidic model for tumor cell intravasation and endothelial barrier function. Proc Natl Acad Sci. 2012;109(34):13515–20.

56. Nguyen D-HT, Stapleton SC, Yang MT, Cha SS, Choi CK, Galie P a, Chen CS. Biomimetic model to reconstitute angiogenic sprouting morphogenesis in vitro. Proc Natl Acad Sci. 2013;110(17):6712–7.

57. Baker BM, Trappmann B, Stapleton SC, Toro E, Chen CS. Microfluidics embedded within extracellular matrix to define vascular architectures and pattern diffusive gradients. Lab Chip. 2013;13:3246–52.

58. Bischel LL, Young EW, Mader BR, Beebe DJ. Tubeless microfluidic angiogenesis assay with three-dimensional endothelial-lined microvessels. Biomaterials. 2013;34:1471–7.

59. Lee H, Park W, Ryu H, Jeon NL. A microfluidic platform for quantitative analysis of cancer angiogenesis and intravasation. Biomicrofluidics. 2014;8(5):054102.

60. Buchanan CF, Voigt EE, Szot CS, Freeman JW, Vlachos PP, Rylander MN. Three-Dimensional Microfluidic Collagen Hydrogels for Investigating Flow-Mediated Tumor-Endothelial Signaling and Vascular Organization. Tissue Eng Part C. 2014;20(1):64–75.

61. Jayson GC, Kerbel R, Ellis LM, Harris AL. Antiangiogenic therapy in oncology: current status and future directions. Lancet. 2016;388:518–29.

APPENDIX A

ADDITIONAL RESULTS

This appendix details other work that was completed but is not included in any of the other chapters within this dissertation.

A.1 Endothelial Network Formation on Compliant 2D Substrates

It is known that cells can sense and respond to their surrounding mechanical environment [1] and endothelial cell (EC) response to these biophysical cues can differ in 2D and 3D environments [2]. In particular, previous work from the Reinhart-King lab and other labs observed the formation of capillary network-like structures on compliant but not stiff 2D matrices [3–7]. This behavior is likely the result of decreased cell-matrix adhesivity consequently promoting cell-cell interactions [3].

In addition to experimental approaches, computational studies have been performed to investigate EC assembly on compliant substrates. Notably, the Merks lab (Centrum Wiskunde & Informatica, The Netherlands) develops complex computational models of multicellular systems, including blood vessels. In one study, they created a model of individual and collective EC behavior based on the reciprocal relationship

between a cell and its surrounding extracellular matrix [8]. To complement their computational model, I performed an *in vitro* experiment demonstrating capillary network formation of bovine aortic endothelial cells (BAECs) on a compliant polyacrylamide gel (Figure A.1). Altogether, this publication used a combined computational and *in vitro* approach to better understand the dynamic relations regulating endothelial morphogenesis.

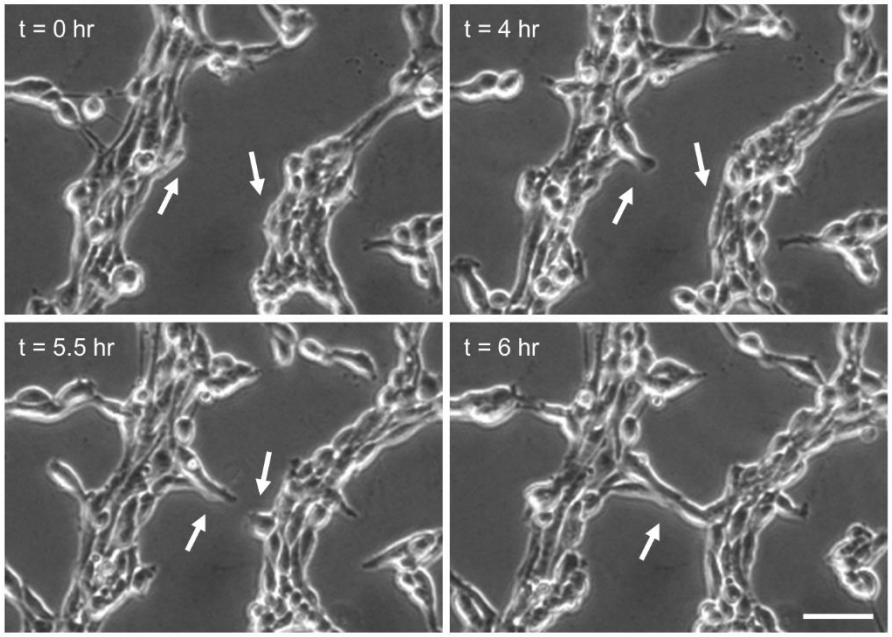

Figure A.1. Endothelial network formation on a compliant substrate. Time-lapse imaging of bovine aortic endothelial cells seeded onto a 2.5 kPa polyacrylamide gel functionalized with an RGD-containing peptide. Arrows indicate cells that join together and elongate into a network. Time scale is in hours. Scale bar, 50 μm.

A.2 Endothelial Permeability with Matrix Stiffness and Fibronectin Cues

During cancer progression many extracellular changes are known to occur within the tumor microenvironment. Importantly, the effects of simultaneous tumor-specific chemical and mechanical cues on cell behavior are not yet fully understood. In Chapter 2, I investigated numerous EC responses to increased matrix stiffness and VEGF stimulation, two known extracellular changes occurring during cancer progression [9,10]. In addition, elevated fibronectin (Fn) production has also been observed during cancer [11–13]. Therefore, to explore the interplay of matrix stiffness and Fn signaling pathways on EC behavior, I investigated endothelial monolayer permeability when both stimuli were present.

Previous data from our lab revealed heightened endothelial permeability with increased extracellular matrix (ECM) stiffness [14,15]. To probe the influence of both matrix stiffening and Fn signaling, BAECs were seeded onto compliant (1 kPa) or stiff (10 kPa) polyacrylamide (PA) hydrogels coated with 100 μg mL^{-1} collagen I or Fn solution. EC permeability was measured as the flux of FITC-dextran supplemented medium through the cell monolayer into the PA gel below (Figure A.2A-B). In agreement with others, my data show increased EC permeability as a function of ECM stiffness (Figure A.2C). Additionally, elevated permeability was observed in BAECs seeded on stiff, Fn-coated matrices compared to cells cultured on stiff, collagen-coated substrates (Figure A.2C), suggesting possible mechanistic crosstalk between matrix stiffness and Fn signaling pathways. Further, since increased ECM protein deposition contributes to ECM stiffening during tumor progression [16], I investigated the

influence of ECM density on permeability for ECs cultured on 10 kPa gels. My results indicate a concentration-dependent increase in endothelial permeability regardless of ECM type (Figure A.2D). In addition, heightened permeability was reported for cells cultured on stiff, Fn-coated matrices compared to collagen-coated gels at higher protein concentrations only (Figure A.2D). This suggests that sufficient integrin engagement may be necessary for an additive phenotypic response mediated by ECM stiffness and Fn pathways. Collectively, this work highlights complex crosstalk between pathways activated by matrix stiffness and Fn, two important microenvironmental stimuli that may promote the development of hyperpermeable vessels during tumor angiogenesis.

Figure A.2. Endothelial monolayer permeability increases as a function of matrix stiffness and ECM protein type and concentration. (A) Schematic of the permeability assay showing the movement of a 40 kDa FITC-dextran fluorescent dye through the endothelial monolayer into the PA gel. (B) A representative image of an acellular gel following 5 min of FITC-dextran medium permeation. (C) BAECs were cultured on 1 kPa or 10 kPa PA gels coated with either 100 μg mL^{-1} collagen I or fibronectin solution and subjected to the aforementioned permeability assay. Elevated permeability was observed with increased ECM stiffness and in cells cultured on stiff, fibronectin-coated substrates compared to those on stiff, collagen-coated matrices. Plots are mean ± SD. N = 2 independent experiments. (D) The permeability assay was performed on BAECs seeded onto 10 kPa PA substrates coated with 10-100 μg mL^{-1} collagen I or fibronectin solution. BAEC monolayer permeability increased as a function of ECM protein density and for cells cultured on fibronectin-coated matrices at higher protein concentrations only. Plots are mean ± SE. N = 3-5 gels per condition. * $p<0.05$, ** $p<0.01$, *** $p<0.001$ from ANOVA with post hoc Tukey's test.

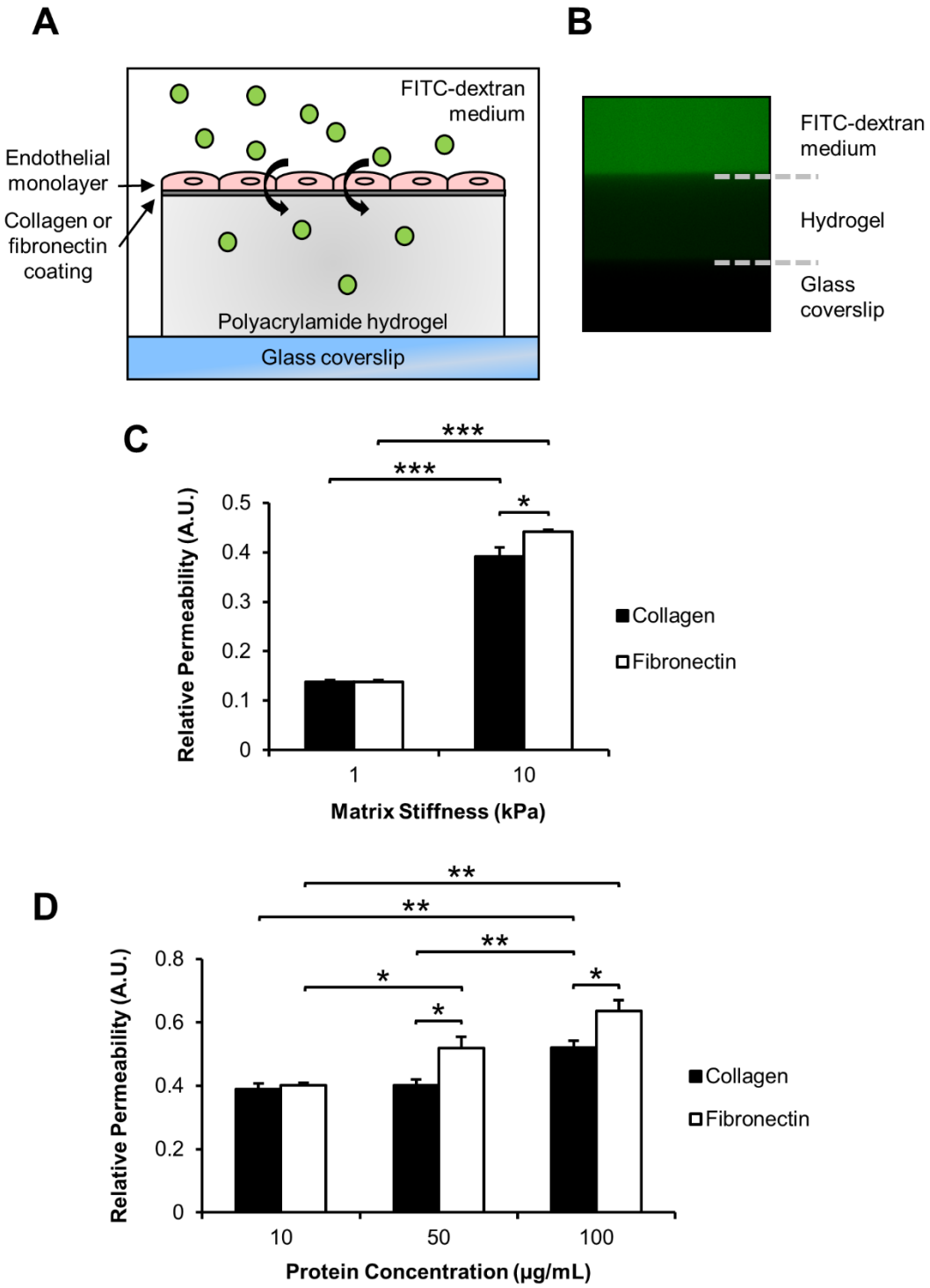
A
B
FITC-dextran medium
Endothelial monolayer
Collagen or fibronectin coating
Polyacrylamide hydrogel
Glass coverslip
FITC-dextran medium
Hydrogel
Glass coverslip
C
***
***
*
Relative Permeability (A.U.)
0.5
0.4
0.3
0.2
0.1
0
1
10
Matrix Stiffness (kPa)
Collagen
Fibronectin
D
**
**
**
*
*
*
Relative Permeability (A.U.)
0.8
0.6
0.4
0.2
0
10
50
100
Protein Concentration (μg/mL)
Collagen
Fibronectin

A.3 Isolation of Endothelial Cells from MMTV-PyMT Tumor Tissue

Aiming to investigate inherent differences between healthy and tumor-derived ECs, I developed a protocol to isolate ECs from MMTV-PyMT mouse tumors based on magnetic selection of CD31 labeled cells (Appendix B). While numerous microenvironmental cues contribute to tumor angiogenesis, I sought to delineate the effect of matrix stiffening on healthy and cancer-associated ECs for alterations in specific cellular characteristics, such as cell morphology and VE-cadherin localization, as well as its role in EC behaviors, including endothelial tube formation and permeability.

In an initial experiment, tumors were isolated from a MMTV-PyMT mouse, digested with collagenase, and the cells were seeded onto glass coverslips (Figure A.3). Cells were then fixed with 3.7% formaldehyde, permeabilized with 1% Triton, and immunostained for fibroblast specific protein 1 (FSP1) and VE-cadherin. Nuclei were counterstained with DAPI. Fluorescent imaging of the samples revealed a few FSP1 positive cells, a small cluster of VE-cadherin positive cells, and many cells were double negative for both of these stains (DAPI positive only; Figure A.3). Therefore, this indicates that ECs were present within the mouse tumors, along with other cell types including fibroblasts.

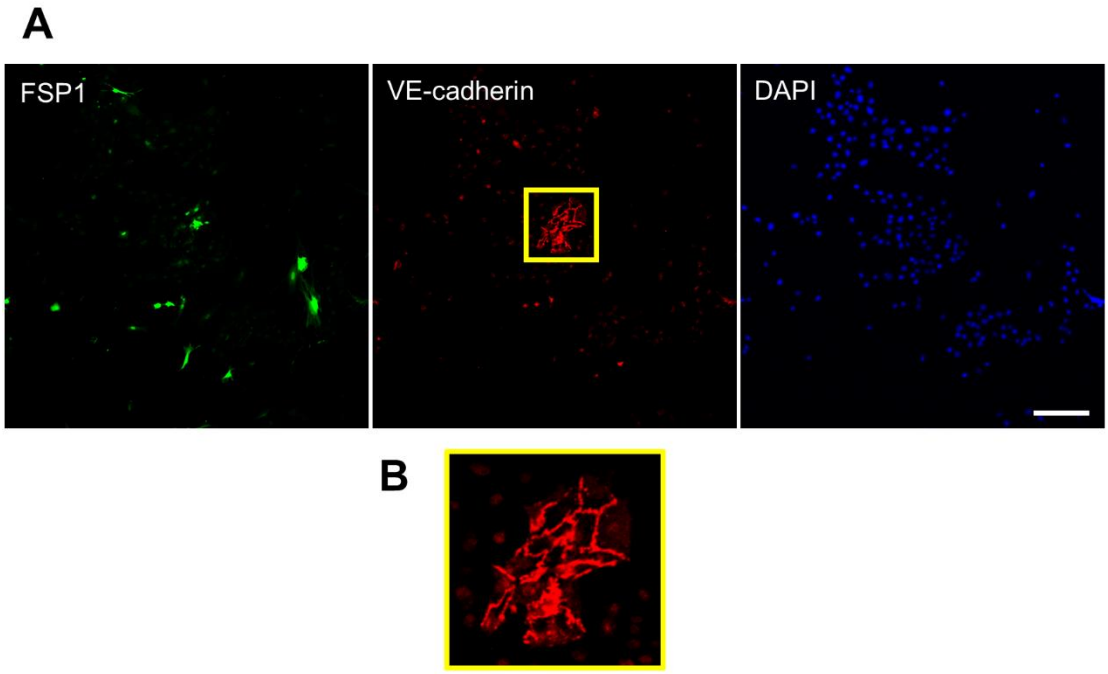

Figure A.3. Tumors isolated from MMTV-PyMT mice contain a wide variety of cell types. (A) Tumor cells were immunostained for fibroblast specific protein 1 (FSP1), VE-cadherin, and DAPI. Fluorescent images indicate that fibroblasts and endothelial cells were present among other cell types. (B) A 3x zoom of the boxed region in (A). Scale bar, 200 μm.

Further, MMTV-PyMT tumor-derived cells were subjected to a magnetic bead separation protocol (Appendix B). Following tissue digestion, filtering through cell strainers, and red blood cell lysing, tumor cells were labeled with CD31 microbeads. Labeled cells were passed over a magnetic column where CD31 positive (CD31+) cells remained bound to the column and CD31 negative (CD31-) cells flowed directly through were collected at the bottom. Imaging of both CD31+ and CD31- cells showed distinct cell morphologies within each fraction (Figure A.4). Notably, CD31+ cells formed small cell clusters that resembled traditional EC cobblestone-like morphology. Moreover, CD31- cells displayed numerous cell shapes, especially those that resembled tight epithelial cell clusters and those with long cell projections that resembled fibroblasts. Altogether, this indicates that tumor-associated ECs can be isolated from MMTV-PyMT mouse tumors using CD31 magnetic bead selection. Future experiments should look to improve the yield and purity of the CD31+ cell fraction through a second round of magnetic separation or alternative strategies (i.e. CD326 depletion followed by CD31 isolation).

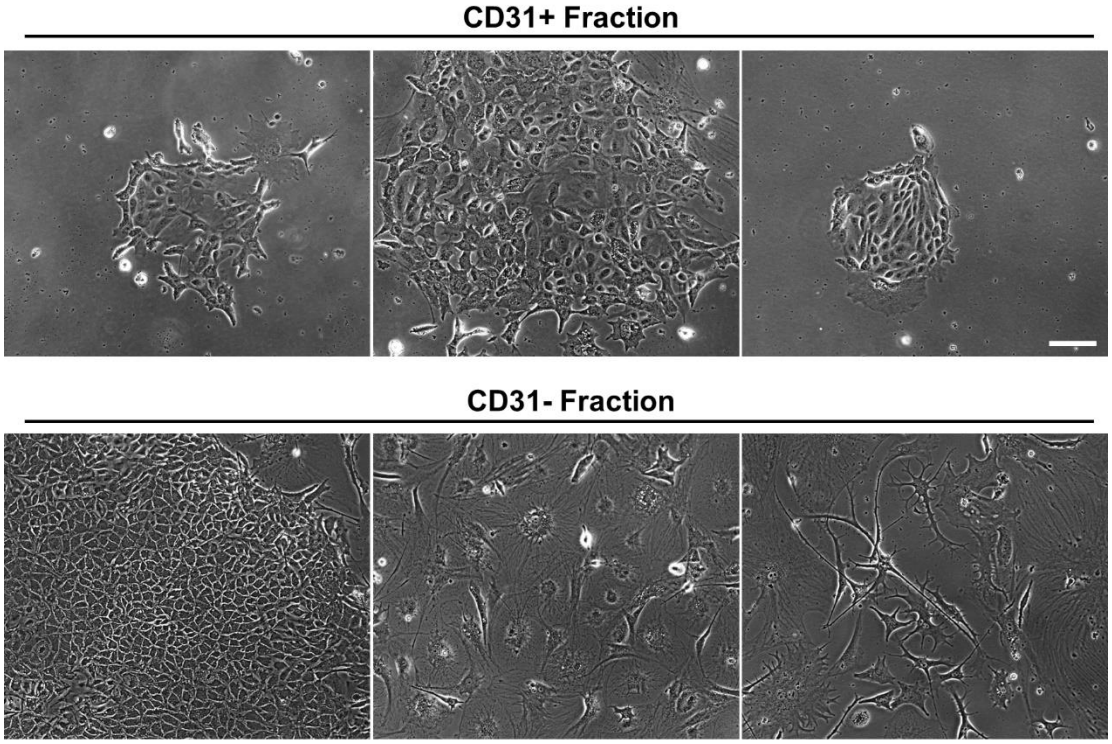

Figure A.4. CD31 magnetic bead separation of a MMTV-PyMT mouse tumor reveals subpopulations of cells with distinct morphologies. The fraction of CD31 positive cells (top panel) resemble the cobblestone-like morphology of endothelial cell clusters. The fraction of CD31 negative cells not retained by the magnetic column (bottom panel) exhibit a wide range of cell morphologies, including epithelial-like clusters and those resembling fibroblasts. Scale bar, 100 μm.

In addition to examining cell morphology, the CD31+ cell fraction was stained for an endothelial-specific marker as a means to identify ECs from other contaminating cell types. Since acetylated low-density lipoprotein (AcLDL) has previously been used to identify ECs from primary culture [17], it was also as a EC marker in this study. Cells were stained with fluorescent AcLDL (Thermo Fisher Scientific #L3484) for 4 h at 37^{o}C. HUVECs were also stained as a control. Fluorescent imaging showed distinct punctated structures within both cell types, indicating ECs that contain numerous LDL complexes. Importantly, this probe allows for staining of live cells which would allow subsequent experiments to be performed on the same population of ECs.

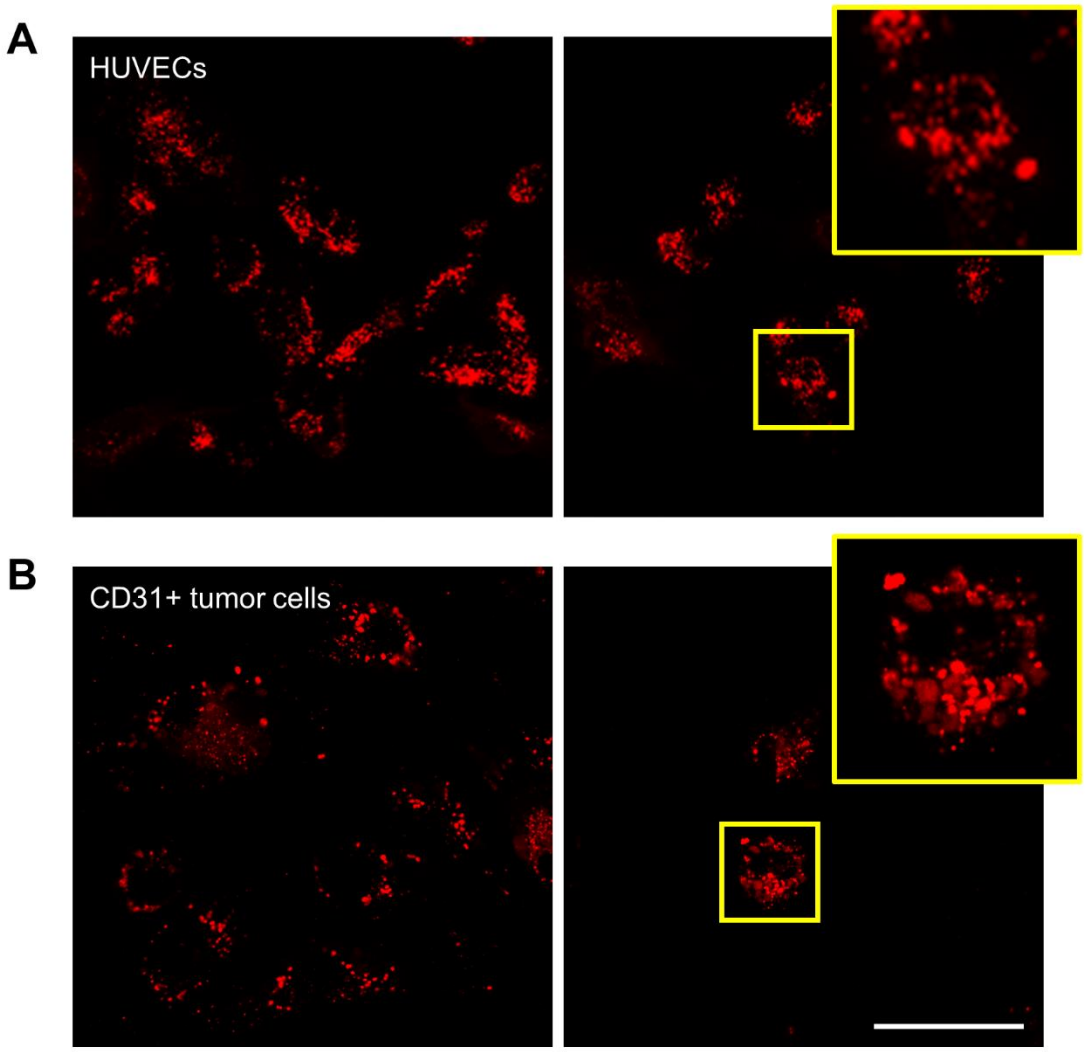

Figure A.5. DiI-labeled AcLDL can be used as a live-cell fluorescent marker to identify tumor-derived endothelial cells. Unfixed HUVECs (A) and tumor cells from the CD31+ fraction after microbead sorting (B) were stained with DiI-labeled AcLDL for 4 h at 37°C. Fluorescent images revealed that both cell types contained punctated AcLDL structures. Insert is a 2.5x zoom of the boxed region. Scale bar, 50 μm.

REFERENCES

1. Discher DE, Janmey P, Wang Y-L. Tissue cells feel and respond to the stiffness of their substrate. Science. 2005;310:1139–43.
2. LaValley DJ, Reinhart-King CA. Matrix stiffening in the formation of blood vessels. Adv Regen Biol. 2014;1(1):25247.
3. Califano JP, Reinhart-King CA. A balance of substrate mechanics and matrix chemistry regulates endothelial cell network assembly. Cell Mol Bioeng. 2008;1(2–3):122–32.
4. Saunders RL, Hammer DA. Assembly of human umbilical vein endothelial cells on compliant hydrogels. Cell Mol Bioeng. 2010;3(1):60–7.
5. Sun J, Jamilpour N, Wang F-Y, Wong PK. Geometric control of capillary architecture via cell-matrix mechanical interactions. Biomaterials. 2014 Mar;35(10):3273–80.
6. Wu Y, Al-Ameen MA, Ghosh G. Integrated effects of matrix mechanics and vascular endothelial growth factor (VEGF) on capillary sprouting. Ann Biomed Eng. 2014;42(5):1024–36.
7. Dickinson LE, Rand DR, Tsao J, Eberle W, Gerecht S. Endothelial cell responses to micropillar substrates of varying dimensions and stiffness. J Biomed Mater Res A. 2012 Jun;100(6):1457–66.
8. van Oers RFM, Rens EG, LaValley DJ, Reinhart-King CA, Merks RMH. Mechanical cell-matrix feedback explains pairwise and collective endothelial cell behavior in vitro. PLoS Comput Biol. 2014;10(8):e1003774.
9. Levental KR, Yu H, Kass L, Lakins JN, Egeblad M, Erler JT, Fong SFT,

Csiszar K, Giaccia A, Weninger W, Yamauchi M, Gasser DL, Weaver VM. Matrix crosslinking forces tumor progression by enhancing integrin signaling. Cell. 2009;139:891–906.

10. Ferrara N, Davis-Smyth T. The biology of vascular endothelial growth factor. Endocr Rev. 1997;18(1):4–25.
11. D'Ardenne AJ, McGee JO. Fibronectin in disease. J Pathol. 1984;142:235–51.
12. Bae YK, Kim A, Kim MK, Choi JE, Kang SH, Lee SJ. Fibronectin expression in carcinoma cells correlates with tumor aggressiveness and poor clinical outcome in patients with invasive breast cancer. Hum Pathol. 2013;44(10):2028–37.
13. Fernandez-Garcia B, Eiró N, Marín L, González-Reyes S, González LO, Lamelas ML, Vizoso FJ. Expression and prognostic significance of fibronectin and matrix metalloproteases in breast cancer metastasis. Histopathology. 2014;64(4):512–22.
14. Huynh J, Nishimura N, Rana K, Peloquin JM, Califano JP, Montague CR, King MR, Schaffer CB, Reinhart-King CA. Age-related intimal stiffening enhances endothelial permeability and leukocyte transmigration. Sci Transl Med. 2011;3(112):112ra122.
15. Bordeleau F, Mason BN, Lollis EM, Mazzola MC, Zanotelli MR, Somasegar S, Califano JP, Montague CR, LaValley DJ, Huynh J, Negrón Abril YL, Bonassar LJ, Butcher JT, Weiss RS, Reinhart-King CA. Matrix stiffening promotes a tumor vasculature phenotype. Proc Natl Acad Sci. 2016;114(3):492–7.
16. Lu P, Weaver VM, Werb Z. The extracellular matrix: A dynamic niche in

cancer progression. J Cell Biol. 2012;196(4):395–406.

17. Voyta JC, Via DP, Butterfield CE, Zetter BR. Identification and isolation of endothelial cells based on their increased uptake of acetylated-low density lipoprotein. J Cell Biol. 1984;99(6):2034–40.

APPENDIX B

PROTOCOL FOR MMTV-PYMT MOUSE TUMOR EXTRACTION AND ENDOTHELIAL CELL ISOLATION

B.1 Extracting Tumors from MMTV-PyMT Mice

Materials:

Dissecting tools (scissors, forceps, pins, etc.)

Styrofoam box lid

Absorbent underpad (VWR #56616-031)

100% ethanol

50 mL conical tube of medium, chilled

Ice

1. Euthanize the mouse following proper IACUC protocols.
2. In the hood, clean the Styrofoam lid with ethanol. Place the absorbent pad on top of the Styrofoam lid.
3. Place the mouse on top of the absorbent pad. Position the mouse on its back and place pins at its feet and tail.
4. Cut and peel back the layer of skin until the tumors are visible. Pin the skin flap open for easy access to the tumors.

5. Surgically dissect out the tumors. Place the tumors into the conical tube containing medium. Keep on ice.
6. Clean up the hood and properly dispose of the mouse. Transfer the tumors back to the lab for processing.

B.2 Isolation of Tumor Endothelial Cells

Note: This protocol was adapted from the Miltenyi Biotec protocol. See https://www.miltenyibiotec.com/US-en/applications/All-application-protocol/isolation-of-tumor-cells-from-mouse-tumor-tissue-samples.html

Note: The volumes used in this protocol are for LS columns (up to $2x10^9$ total cells). For smaller samples, MS columns may be used instead (up to $2x10^8$ total cells).

Materials:

Sterile 100 mm petri dish

Sterile PBS

No. 10 scalpel blade

Scalpel handles

Tumor dissociation kit, mouse (Miltenyi Biotec #130-096-730)

MACS SmartStrainers (70, 100 µm – Miltenyi Biotec #130-098-462 and 130-098-463)

MACS pre-separation filters (30 µm – Miltenyi Biotec #130-041-407)

BD Pharm Lyse™ (BD #555899), diluted in MilliQ water

PEB buffer

- 2 mM EDTA
- 0.5% BSA
- Degassed PBS
- Sterile filtered and chilled at 4^{o}C

Dead cell removal kit (Miltenyi Biotec #130-090-101)

CD45 microbeads, mouse (Miltenyi Biotec #130-052-301)

CD326/EpCAM microbeads, mouse (Miltenyi Biotec #130-105-958)

CD31 microbeads, mouse (Miltenyi Biotec #130-097-418)

MS/LS columns (Miltenyi Biotec #130-042-201 and 130-042-401)

MACS® separators

- QuadroMACS separator (Miltenyi Biotec #130-090-976)
- MiniMACS separator (Miltenyi Biotec #130-042-102)

MACS multistand (Miltenyi Biotec #130-042-303)

Tumor endothelial medium

- 10% Nu-Serum IV (Corning #47743-634)
- 3 ng/mL bFGF (Millipore #GF003)
- 50 ng/mL VEGF (R&D Systems #293-VE-010)
- 100 mg/L porcine heparin (VWR #AAAA16198-MD)
- 10% FBS
- 1% Penstrep
- Low-glucose DMEM (Thermo Fisher Scientific #11885-084)

15 mL and 50 mL conical tubes

1.7 mL Eppendorf tubes

gentleMACS™ C tube (Miltenyi Biotec #130-093-237)

gentleMACS™ dissociator (Miltenyi Biotec #130-093-235)

Tube rotator, placed in incubator

Note: Tumor endothelial medium formulation adapted from Dudley et al. Calcification of Multipotent Prostate Tumor Endothelium. Cancer Cell (2008).

1. Aspirate most of media out of the 50 mL conical tube containing the tumor tissue. Rinse the tumors and the tube with PBS. Move the tissue into a sterile petri dish. Quickly rinse with PBS. Aspirate off any excess PBS.
2. Attach the scalpel blades to the handles. Mince the tumors well aiming for 2-4 mm pieces.
3. Add 2.35 mL DMEM, 100 µL of Enzyme D, 50 µL of Enzyme R, and 12.5 µL of Enzyme A (from tumor dissociation kit) to the C tube. Transfer the minced tumor pieces to the C tube.
4. Tightly close the C tube and place it on the dissociator. Run the program m_impTumor_02. Detach tube and incubate 40 min at 37^{o}C on tube rotator. Run the program m_impTumor_03 twice.
5. Place the 100 µm strainer into a new 50 mL conical tube. Wet the filter with PBS. Pour the digested tumor tissue into the strainer. Rinse the filter 3x with PBS.

    Note: If the strainer becomes blocked, stir the mixture with a pipet tip.

6. Centrifuge at 300xg for 10 min. Aspirate the supernatant.
7. Prepare 20 mL of 1x PharmLyse B solution.

    2 mL of 10x PharmaLyse B

    18 mL sterile MilliQ water
8. Resuspend the cell pellet in 1x PharmLyse B solution. Incubate for 10 min at room temperature on the rocker.
9. Centrifuge at 300xg for 10 min. Aspirate the supernatant.
10. Resuspend the cell pellet in 7 mL of MACS buffer.
11. Place a 70 µm strainer into a fresh 15 mL conical tube. Wet the filter with MACS buffer. Pour the cell solution into the strainer. Rinse the filter 3x with MACS buffer.
12. Centrifuge at 300xg for 5 min. Aspirate the supernatant.
13. Incubate the cells with the microbeads.
    a. Resuspend the cells in 90 µL of MACS buffer (up to 10^7 cells)
    b. Add 10 µL of microbeads. Mix well.
    c. Incubate at 4^{o}C for 30 min on the rocker.

    Note: Vary the microbead dilution factor based on the number of cells.
14. Add 1 mL of PEB buffer to the tube. Centrifuge at 300xg for 5 min. Aspirate the supernatant.
15. Prepare the MACS equipment: place the MACS multistand and QuadroMACS separator into the hood. Place a sterile LS column into separator. Keep the plunger aside.

    Note: For MS column use the MiniMACS separator.

16. Resuspend the cells in 500 μL of buffer (up to 10^8 cells).
17. Rinse the column with 3 mL of MACS buffer. Place a 30 μm pre-separation filter on top and wet with buffer.

    Note: Rinse with 500 μL buffer for MS column.
18. Place a 1.7 mL Eppendorf tube or 1.5 mL conical tube in a rack underneath the bottom of the column.
19. Pipet the cell suspension into the filter. Collect unlabeled cells at the bottom. Wait until all of the liquid has flowed through the column before proceeding to the next step.
20. Wash filter/column 3x with 3 mL buffer each. Use first wash to rinse out 15 mL tube that the cells were in previously.

    Note: For MS column wash 3x with 500 μL buffer each.
21. Remove the LS column from the separator and place into a new 15 mL conical tube.
22. Add 5 mL MACS buffer to the top of the column and immediately press the plunger into the column to elute the bound cells.

    Note: For MS column plunge with 1 mL buffer.

    Note: To further increase the cell purity, the cell effluent can be passed over a second column (repeat steps 17-22).
23. If performing another round of separation, repeat steps 13-22.
24. Spin cells at 300xg for 5 min. Aspirate the supernatant.
25. Resuspend the desired cells in tumor endothelial media and plate into tissue culture flasks or well plates.

Note: Flasks or well plates can be coated with 100 μg/mL collagen or fibronectin to further promote cell attachment.

Strategies I have tried:

- CD45 depletion followed by CD31 isolation on the CD45- fraction
- CD45 depletion, then CD326 depletion on the CD45- fraction, followed by CD31 isolation on the CD326-/CD45- fraction
- CD45/CD326 depletion (incubate with microbeads simultaneously), followed by CD31 isolation on the CD326-/CD45- fraction
- Dead cell removal kit, then CD45 depletion on the live cell fraction, followed by CD31 isolation on the live cell/CD45- fraction

Note: No single strategy proved superior to the others. Strategies with multiple steps prior to CD31 isolation resulted in decreased cell number, which sometimes caused subsequent cell death due to insufficient cell number. Strategies with fewer steps often contained contaminating cells, most which appear to be fibroblasts.

APPENDIX C

PROTOCOL FOR GENOTYPING MMTV-PYMT MICE

C.1 Day 1: Tail Snips and Tissue Digestion

Ear Punches and Tail Snips

Note: This procedure is suggested for 12-15 day old mice.

Materials:

Animal ear punch (VWR #10806-286)

No. 10 scalpel blade

70% ethanol/water

1.7 mL Eppendorf tubes, with rack

Paper towels

1. Sterilize the hood with disinfectant. Place the cage with mice into the hood and wipe down the outside of the cage with disinfectant.
2. Obtain a clean cage and add fresh food pellets.
3. Sterilize the ear punch tool with 70% ethanol/water. Prepare a paper towel soaked in ethanol to wipe down the ear punch between mice.
4. Sterilize the scalpel blade with ethanol.

5. Label one 1.7 mL Eppendorf tube per mouse and place into the rack.
6. Separate the male and female pups based on their anogenital distance.

    Note: I would place females onto top of new cage and hold males in my non-dominant hand in their cardboard housing piece until all of the pups were sorted. Then I placed the male pups back into their original cage.
7. One at a time, tail snip and ear punch each mouse.
    a. Scruff the mouse with your non-dominant hand. Make sure its ears are accessible, and if not, free them with your finger.
    b. Hold the ear punch tool in your dominant hand. Place the edge of the mouse's ear between the open ends of the ear punch. Press the ear punch ends firmly together to create a hole in the ear.
    c. Keep a record of each mouse's sex, ear pattern, and Eppendorf tube number.
    d. Using your non-dominant hand, hold mouse by its tail at the corner edge of the new cage with the mouse dangling inside of the cage. If needed, adjust your hand position to the middle of the tail so that the very tip of the tail is accessible.
    e. Hold the scalpel in your dominant hand. Cut off the last 1-2 mm tail tissue and then immediately drop the mouse into the cage.
    f. Collect the tail sample into the Eppendorf tube. Cap tube and place in rack.
    g. Repeat for each mouse. Re-sterilize the ear punch tool and scalpel in between each mouse with ethanol.

8. Once all of the pups have been ear punched and tail snipped, clean up the area. Discard the scalpel and dirty cage.
9. Transfer the tail samples back to the lab for further processing.

Digestion of Tail Tissue

Note: It is best if digestion is done immediately after tail snips are collected, but if necessary, the tail samples can be stored at -20^{o}C for 1 day.

Materials:

Tail digestion buffer

10 mM Tris-Cl pH 8.0

10 mM EDTA pH 8.0

50 mM NaCl

0.5% SDS

MilliQ water

10 mg/mL proteinase K solution:

100 mg proteinase K (Millipore #70663-4)

50 mM Tris-Cl pH 8.0

10 mM $CaCl_2$

MilliQ water

Water bath

1. Prepare a 20:1 working solution of tail buffer and proteinase K solution. Add 250 µL per Eppendorf tube containing the tail samples.

   Note: Make sure the tail is at the bottom of the tube in the buffer. If not, invert the tube.

2. Place Eppendorf tubes into the tube rack. Incubate the tubes in a 50ºC water bath for 4 h to overnight.

   Note: Digestion is completed when the tails have collapsed into a pile of hair and bone at the bottom of the tube.

C.2 Day 2: DNA Extraction, PCR, and Gel Electrophoresis

DNA Extraction

Materials:

1.7 mL Eppendorf tubes (3 per tail)

5 M NaCl/water

100% ethanol

70% ethanol/water

Sterile MilliQ water

Flame-closed glass capillary tubes

Ice

Microcentrifuge

Note: Open ended capillary tubes (e.g. Thomas Scientific #44A509) may be closed on one end by quickly passing over a Bunsen burner flame.

1. Add 125 µL of 5M NaCl per tube of digested tail tissue.
2. Shake the tubes vigorously until the solution turns white.
3. Place the tubes on ice for 10 min.
4. Spin down the tubes at 5,000 RPM for 5 min.
5. While the tubes are spinning, prepare three new 1.7 mL Eppendorf tubes per tail in the microcentrifuge rack in the following manner.

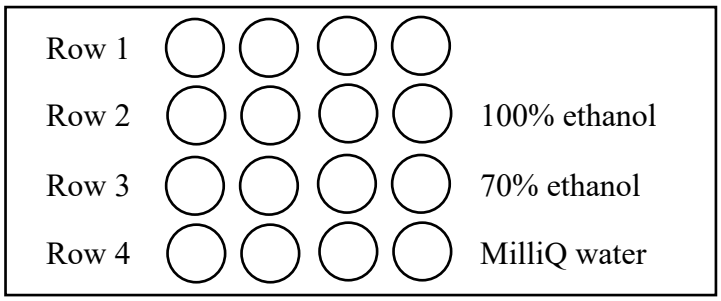

   Note: Space the tubes 2-3 columns apart so that they do not contaminate one another.

   a. Add 600 µL of 100% ethanol to tubes in Row 2.
   b. Add 600 µL of 70% ethanol to tubes in Row 3.
   c. Add 200 µL MilliQ water to tubes in Row 4.
6. When the tubes are done spinning, place them into Row 1 of the rack.
7. One tube at a time, precipitate the DNA.
   a. Transfer 300 µL of supernatant into the tube containing 100% ethanol (Row 2). Check for a white stringy DNA precipitate.
   b. Spool the DNA onto the fire-closed end of the capillary tube.

Note: It is best to hold the capillary tube between your index finger and thumb and first twist near the top of the solution to collect the DNA, then let it fall to the bottom of the tube and continue twisting ~15x. Notice the "bubbles" that appear on the capillary tube.

8. Wash the capillary tube with the DNA by inverting into the tube containing 70% ethanol (Row 3). Swirl the capillary tube ~5x without touching the bottom of the tube.
9. Invert the capillary tube (DNA side up) and place it next to the tube in Row 4. Let it dry for at least 5 min.
10. Repeat steps 7-9 for all tail samples.
11. One at a time, invert the capillary tube (DNA side down) and place into the tubes containing 200 μL dH_2O (Row 4). Break off the glass top of the capillary tube until it fits into the Eppendorf tube. Close the lid. Repeat for all of the samples.
12. Vortex the tubes to mix. Store at -20^{o}C.

PCR

Note: For information on the forward and reverse primers, see https://www2.jax.org/protocolsdb/f?p=116:5:0::NO:5:P5_MASTER_PROTOCOL_ID,P5_JRS_CODE:27997,002374

Materials:

PCR tubes (Thermo Fisher Scientific #AB1182)

PCR tips

DNase-free 1.7 mL Eppendorf tubes

Sterile MilliQ water

10x PCR buffer (Thermo Fisher Scientific #N8080129)

10 mM dNTPs (New England Biolabs #N0447S)

Forward and reverse primers

Taq polymerase (Clontech #RR02AG)

Ice

Microcentrifuge

PCR machine

1. Label PCR tubes with mouse IDs. Remember to include both a positive and negative control and a blank (buffer only) sample.
2. Thaw the PRC reagents on ice.
3. Create the PCR master mix: Determine the number of reactions desired. In a 1.7 mL Eppendorf tube, add each of the PCR reagents one at a time in the order they appear. **Do not add Taq yet.**

    Note: Return the stock solutions back to the ice bucket after adding each to the Eppendorf tube. After adding all of the reagents, store the Eppendorf tube on ice.

	Number of Reactions					
	5	**10**	**15**	**20**	**25**	**30**
Water (µL)	102.25	204.50	306.75	409.00	509.25	613.50
10x PCR buffer (µL)	12.50	25.00	37.50	50.00	62.50	75.00
10 mM dNTPs (µL)	2.50	5.00	7.50	10.00	12.50	15.00
Primer 1 (µL)	2.50	5.00	7.50	10.00	12.50	15.00
Primer 2 (µL)	2.50	5.00	7.50	10.00	12.50	15.00
Taq polymerase (µL)	1.00	2.00	3.00	4.00	5.00	6.00

(Assumes the primers are at a concentration of 25 pmol/µl.)

4. Add 0.5 µL of DNA solution per PCR tube. Store the remaining DNA at -20ºC.

   Note: It is easiest to add as a drop to the tube on the inner side closest to you.

5. Add Taq to the Eppendorf tube. Mix well.
6. Add 24.5 µL of the PCR master mix per PCR tube. Add 25 uL to the blank tube.

   Note: Try to add the mix on top of the DNA drop on the side of the tube and force it down to the bottom of the tube.

7. Place the cap strip on top of the tubes, making sure they are labeled correctly. Quickly spin down the tubes to force all of the liquid to the bottom.
8. Run the PCR program (~2 h):

Temperature (°C)	Time (min)	
94	3	
94	0.5	Repeat 35x
64	1	
72	1	
72	2	
10	infinity	

Note: reaction volume = 25 μL

Agarose Gel Electrophoresis

Note: It is best to prepare the gel(s) immediately after beginning the PCR program. Gel(s) require a minimum of 1 h to polymerize but can be left at room temperature for up to 4 h. If left longer, store at 4°C in 1x TAE buffer.

Materials:

Agarose (Thermo Fisher Scientific #BP1356-100)

1x TAE buffer

20 mL of 50x TAE buffer (Thermo Fisher Scientific #B49)

980 mL MilliQ water

Ethidium bromide (Sigma-Aldrich #E1510)

1 kB DNA ladder (Thermo Fisher Scientific #10787018)

6x loading dye (Thermo Fisher Scientific #R0611)

Erlenmeyer flask

Microwave

Gel electrophoresis equipment

UV trans-illuminator

1. For each gel, add 0.24 g agarose to 30 mL 1x TAE buffer in Erlenmeyer flask. Swirl gently to mix.
2. Microwave the solution 2x for 30 sec each. Cover the top of flask loosely with bottle cap, making sure it is not air tight. Swirl to mix in between heating cycles. Remove flask from the microwave and allow to cool before handling.

   Note: Cooling can be accelerated by running the outside of the flask under cold water.
3. Prepare the gel electrophoresis apparatus by locking the casting tray into the holder. Place the comb at one end.
4. Once the Erlenmeyer flask is cool enough to touch, add 2.5 μL of ethidium bromide. Swirl to mix. Immediately pour the solution into the casting tray, trying not to create bubbles.

   Note: Small bubbles may be popped with a pipette tip.
5. Polymerize gel 1 h at room temperature.
6. Once PCR is completed and the gel has polymerized, remove the comb. Remove the gel from the casting try and place into the gel electrophoresis chamber with the wells oriented towards the black electrode.

7. Add 1x TAE buffer until the gel is covered. Rinse the wells out with buffer in the chamber.
8. Retrieve samples from the PCR machine.
9. One at a time, mix 5 µL of each sample with 1 µL of 6x loading dye. Load 5 µL into each well. Repeat for all samples.
10. Load 2-3 µL of the DNA ladder into an empty well.
11. Put the lid on the gel electrophoresis chamber. Run the gel at 100V for 10-20 min until the samples have traveled at least half way down the gel.
12. Remove the gel from the chamber and view it on the UV trans-illuminator.

    Note: If the desired bands are still indistinguishable from the leading edge, place the gel back into the chamber and run it for a longer time.